

An investigation into the structure and specificity of a G-Quadruplex
RNA-aptamer

by

Kristina Dorothée Gorkotte-Szameit

a dissertation submitted to the University of Hamburg
Department of Chemistry
Faculty of Mathematics, Informatics and Natural Sciences

in partial fulfillment of the requirements for the degree of

doctor rerum naturalium

Hamburg, Germany

2016

Evaluators:

1. Prof. Dr. Ulrich Hahn
2. Prof. Dr. Zoya Ignatova

Date of disputation: 22.04.2016

This work was carried out from March 2012 to February 2016 in the working group of Prof. Dr. Ulrich Hahn at the Institute of Biochemistry and Molecular Biology, Department of Chemistry, Faculty of Mathematics, Informatics and Natural Sciences, University of Hamburg, Germany.

„No great wisdom can be reached without sacrifice.”

- C.S. Lewis, The Magician's Nephew

List of publications

- 1) Kruspe, Mittelberger, Szameit, Hahn. Aptamers as Drug Delivery Vehicles, *ChemMedChem*, 2014, 9 (9), 1988-2011.
doi: 10.1002/cmdc.201402163
- 2) He, Szameit, Zhao, Hahn, Théato. Postpolymerization Modification Using Less Cytotoxic Activated Ester Polymers for the Synthesis of Biological Active Polymers, *Biomacromolecules*, 2014, 15 (8), 3197-3205.
doi: 10.1021/bm500902t

Table of contents

List of publications.....	I
Table of contents.....	I
Abbreviations	IV
Zusammenfassung.....	VI
Abstract	VII
1. Introduction.....	1
1.1. G-Quadruplexes.....	1
1.1.1. Structural properties	1
1.1.2. Structure analysis of G-Quadruplexes.....	5
1.1.3. Biological relevance.....	7
1.1.3.1. G-Quadruplex binding proteins.....	9
1.2. Aptamers	10
1.2.1. Generation and applications	10
1.2.1.1. Aptamers as therapeutics.....	12
1.2.1.2. Targeted delivery of nucleoside analogs.....	13
1.2.1.3. Endocytic fate of targets and ligands	15
1.2.2. AIR-3, an hIL-6R specific RNA aptamer.....	18
1.2.2.1. The Interleukin-6 receptor system	19
1.2.2.2. Therapeutic targeting of hIL-6 and hIL-6R.....	20
1.2.3. G-Quadruplex forming aptamers	22
2. Aim and motivation	23
3. Materials.....	24
3.1. Chemicals.....	24
3.2. Kits and materials	25
3.3. Buffers, solutions and media.....	25
3.4. Nucleotides.....	28
3.4.1. Nucleoside triphosphates.....	28
3.4.2. Oligonucleotides.....	28
3.5. Size standards for proteins and nucleic acids	29
3.6. Proteins	29
3.6.1. Enzymes.....	29
3.6.2. Antibodies.....	29
3.6.3. Other proteins	30
3.7. Cell lines.....	30
3.8. Software	30
4. Methods.....	31
4.1. Nucleic acid preparation, analysis and modification	31
4.1.1. <i>in vitro</i> T7-transcription.....	31
4.1.2. <i>in vitro</i> T7-transcription using modified nucleotides	32
4.1.3. Polyacrylamide Gel Electrophoresis (PAGE).....	32
4.1.4. Detection of nucleic acids	34
4.1.5. Purification of nucleic acids by diffusion elution after PAGE	34
4.1.6. Radio labeling of nucleic acids 5'-end using ³² P-phosphate.....	34
4.1.7. Stability assessment of RNA molecules.....	36
4.2. Protein-biochemical methods	36
4.2.1. Sodium Dodecyl Sulfate Polyacrylamide Gel Electrophoresis (SDS-PAGE)	36
4.2.2. Detection of proteins by Coomassie staining.....	37
4.3. Methods for nucleic acid-protein interaction studies.....	37
4.3.1. Filter retention analysis (FRA) for RNA-protein interaction	37
4.3.2. Microscale Thermophoresis (MST) for analysis of RNA-protein interaction	37

TABLE OF CONTENTS

4.3.3.	Aptamer mediated pull-down of target proteins.....	38
4.4.	Methods for structural analysis of RNA	38
4.4.1.	In-line probing (ILP)	38
4.4.2.	RNase T1 protection assay	39
4.4.3.	RNA sequencing ladders.....	39
4.4.4.	Analysis of ILP- and RNase T1 protection-data	39
4.4.5.	Circular Dichroism (CD) Spectroscopy for GQ identification and $K_{1/2}^+$ determination..	40
4.4.6.	Electrophoretic mobility shift assay (EMSA) for assessment of GQ oligomerization....	40
4.4.7.	Sample preparation for native mass spectrometry of AIR-3A	40
4.5.	Cell biological methods	41
4.5.1.	Cultivation of eukaryotic cell lines	41
4.5.2.	Cryopreservation of eukaryotic cells.....	42
4.5.3.	Flow Cytometry analysis.....	43
4.5.4.	Fluorescence microscopic analysis.....	43
4.5.5.	Immunostaining of cell surface proteins.....	44
4.5.6.	Cellular compartment staining.....	44
4.5.7.	Cellular binding studies of fluorescently labeled aptamers	45
4.5.8.	Indirect binding studies of unlabeled aptamers.....	45
4.5.9.	Cell cycle synchronization by double T-block or single T-block	45
4.5.10.	Aptamer mediated drug delivery of nucleoside analogs	46
4.5.11.	Proliferation assays for toxicity studies.....	46
4.5.12.	Cell cycle analysis	47
5.	Results.....	48
5.1.	Structural investigations.....	48
5.1.1.	Influence of cations to AIR-3A folding.....	48
5.1.1.1.	Native mass spectrometry of AIR-3A	52
5.1.2.	AIR-3A assembly and stoichiometry of the aptamer:protein complex.....	53
5.1.3.	Structure probing analyses.....	55
5.1.3.1.	Protection from RNase T1 cleavage	56
5.1.3.2.	Flexibility of nucleotides in the GQ motif.....	57
5.2.	Tolerance of AIR-3 and AIR-3A to nucleotide modifications in target binding	60
5.2.1.	Intrinsic modification of AIR-3 with nucleoside analogs	60
5.2.1.1.	Binding studies of gemcitabine modified AIR-3	62
5.2.1.2.	Stability of gemcitabine modified AIR-3.....	63
5.2.1.3.	Cytotoxic properties of gemcitabine modified AIR-3	64
5.2.2.	AIR-3 variants containing deoxy pyrimidines	69
5.3.	Target specificity	71
5.3.1.	Analysis of AIR-3A non-target affinity	71
5.3.2.	AIR-3A-aided protein isolation from cell extracts	73
5.4.	Influence of AIR-3A presence on endocytic behavior	76
5.4.1.	Subcellular localization of endocytosed hIL-6R and AIR-3A.....	76
5.4.2.	Analysis of AIR-3A influence on hIL-6R presentation and endocytosis over time	79
6.	Discussion	81
6.1.	Structural investigation of AIR-3 and AIR-3A	82
6.1.1.	Cationic influence and dimerization of AIR-3A.....	82
6.1.2.	Structure probing for revelation of tetrad composition at nucleotide resolution.....	86
6.2.	Derivatization of AIR-3 and AIR-3A.....	90
6.3.	Analyses on AIR-3A target specificity	92
6.4.	Endocytic fate	94
7.	Future prospects.....	96
8.	References	99
9.	Acknowledgments	111
10.	Appendices	112

TABLE OF CONTENTS

10.1.	GHS hazard statements	112
10.2.	GHS precautionary statements	113
10.3.	Hazardous compounds according to GHS	114
10.4.	CMR substances	115
10.5.	List of proteins identified by LC-MS analysis (5.3.2)	115
10.6.	Eidesstattliche Versicherung	124

Abbreviations

2'-F-Py	2'-fluoro modified pyrimidines	hIL-6R	human Interleukin-6 receptor (also: sIL-6R soluble form of hIL-6R)
AB	antibody		
APC	allophycocyanin, fluorescent phycobiliprotein ($\lambda_{\text{ex}} = 652 \text{ nm}$, $\lambda_{\text{em}} = 657.5$)	Hyper-IL-6	fusion protein of hIL-6R and hIL-6
APS	ammonium persulfate	ILP	in-line probing
ATP	adenosine triphosphate	K⁺	potassium cation
Ba²⁺	barium cation	Li⁺	lithium cation
bp	base pairs	LP x	long pass filter (λ greater than x nm transmitted, less than reflected)
BSA	bovine serum albumin	LSM/cLSM	laser scanning microscopy/confocal LSM
cpm	counts per minute	LT	LysoTracker [®] , lysosomal staining dye
ddH₂O	dideionized water	M	mole per liter
DEPC	diethylpyrocarbonate	min	minute
DLS	dynamic light scattering	mRNA	messenger RNA
DNA	deoxyribonucleic acid	MS	mass spectrometry
DTT	dithiothreitol	MST	microscale thermophoresis
EDTA	ethylenediaminetetraacetic acid	mTrf	murine Transferrin
EMSA	electrophoretic mobility shift assay	NaOAc	sodium acetate
EtBr	ethidiumbromide	NFT x	dichroic beam splitter (λ than x nm transmitted, less than reflected)
EtOH	ethanol	NH₄⁺	ammonium cation
FBS	fetal bovine serum	nm	nanometer
FRET	Förster resonance energy transfer	nt	nucleotide
G	guanine	NTP	nucleoside-5'-triphosphate
GMP	guanosine monophosphate (guanylic acid)	PAGE	polyacrylamide gel electrophoresis
GQ	G-quadruplex	PCR	polymerase chain reaction
h	hour	PEG	polyethylene glycol
H-bond	hydrogen bond	ph	pinhole
HFT	main dichroic beam splitter (reflects x nm wavelengths, transmits all other)	PI	propidium iodide

ABBREVIATIONS

PNK	T4-Polynucleotide kinase	RASSF1	gene encoding Ras association domain-containing protein 1
hIL-6	human Interleukin-6	TEM	transmission electron microscopy
RME	receptor mediated endocytosis	TfR	transferrin receptor (model system for clathrin mediated endocytosis)
RNA	ribonucleic acid	TMAA	trimethylammonium acetate
RT	reverse transcription, also: real time	tRNA	transfer RNA
s	second	U	unit
SOMAmer	Slow Off-rate Modified Aptamer	UV	ultraviolet
Sr²⁺	strontium cation	v/v	volume-volume percentage
TAE	Tris-Acetate-EDTA	w/v	weight-volume percentage
TEMED	N,N,N',N'-tetramethylethylenediamine		
Ras	(<i>Rat sarcoma</i>) GTP-binding protein		

Zusammenfassung

G-Quadruplexe sind in den vergangenen Jahrzehnten mehr und mehr in den Fokus der Nukleinsäure-Forschung gerückt. Dabei entwickelte sich das Verständnis von ihrer Entdeckung als außergewöhnliche Sekundärstruktur motive bis heute hin zu komplexen Modulatoren verschiedener Ebenen der Genregulation. Ein tieferes Verständnis ihrer Funktion und Kontrolle könnte einen wichtigen Beitrag zur Aufklärung regulatoriver Mechanismen leisten und helfen, Dysregulationen besser zu verstehen und neue Behandlungsmöglichkeiten zu eröffnen.

Aptamere sind monomolekulare DNA- oder RNA-Moleküle oder auch Peptide mit individueller dreidimensionaler Faltung und daraus resultierender Spezifität für die selektive Bindung an ein Zielmolekül. Sie besitzen also Antikörpern ähnliche Charakteristika und haben sich zu einer neuen Klasse therapeutisch relevanter Biomoleküle entwickelt. So verbinden sie die Vorteile einer selektiven, starken Bindung an das Zielmolekül, einfacher, kostengünstiger Synthese bei gleichbleibender Qualität, hoher Stabilität und geringer Immunogenität.

Ziel der vorliegenden Arbeit war die Charakterisierung des Aptamers AIR-3 bzw. des 19 nt langen Bindemotivs AIR-3A bezüglich seiner Struktur und Spezifität. AIR-3 wurde zur Bindung an den humanen Interleukin-6-Rezeptor (hIL-6R) selektiert, dessen Fehlregulation mit der Prävalenz und Persistenz verschiedener Krankheiten assoziiert ist, und bereits für *in vitro* Wirkstofftransporte eingesetzt. Strukturell ist über AIR-3A aus vorangegangenen Studien jedoch nur bekannt, dass es einen parallelen G-Quadruplex ausbildet und dass fast alle enthaltenen Nukleotide Bedeutung für die Interaktion mit hIL-6R haben. Auch wurden Hinweise gefunden, dass die Interaktion über Domäne D1 des hIL-6R erfolgt.

Im Rahmen dieser Doktorarbeit wurden deshalb die Struktur von AIR-3A sowie seine Bindspezifität und -stöchiometrie mittels verschiedener Verfahren genauer untersucht. Zudem wurde die Auswirkung der Anwesenheit des Aptamers auf die zelluläre Rezeptorpräsentation sowie der Einfluss von Nukleotid-Modifikationen auf die funktionelle Aptamerintegrität überprüft. Anhand dessen konnte festgestellt werden, dass AIR-3(A) ein größeres Spektrum an Faltungen und Zielmolekülen besitzt als bisher angenommen wurde, und eine große Toleranz bezüglich verschiedener Modifikationen aufweist. Außerdem deuten die Ergebnisse auf einen regulativen Einfluss AIR-3As auf die Endozytose von hIL-6R hin. Dies könnte ein Hinweis darauf sein, dass hIL-6R direkt oder indirekt durch zellulär vorkommende Quadruplexe beeinflusst wird. Vor dem Hintergrund aktueller Fortschritte in der Aufklärung G-Quadruplex-kontrollierter Mechanismen könnten diese Erkenntnisse helfen, das Verständnis für hIL-6R assoziierte Dysfunktionen zu mehren.

Abstract

G-quadruplexes have more and more moved into focus of research in nucleic acids, thereby evolving in scientific significance from exceptional secondary structure motifs to complex modulators of gene regulation. A deeper understanding of their function and control may serve as an important milestone to elucidate regulatory mechanisms and help understand dysregulation. This might offer new opportunities for treatment options in the future.

Aptamers are monomolecular DNAs, RNAs or peptides with defined three dimensional folding, resulting in selective target specificity and affinity. In these characteristics, they resemble antibodies and they developed into a new class of therapeutically relevant biomolecules. They combine several advantages such as selectivity and high affinity to their target, simple and cheap synthesis with low batch to batch variability as well as high stability and low immunogenicity.

The aim of the present thesis was to further characterize the aptamer AIR-3 and its minimal binding motif AIR-3A (19 nt) with respect to its structure and specificity. Originally, AIR-3 was selected for binding to human Interleukin-6 receptor (hIL-6R), a key player in inflammatory diseases and cancer, and has recently been exploited for *in vitro* drug delivery studies. Concerning its structure, former studies gave only little insight. As such, it is known to date that AIR-3A forms an all-parallel G-quadruplex and that almost all nucleotides in the binding motif are essential to maintain affinity towards hIL-6R. Also, experimental data indicated that interaction with the target occurs via hIL-6R-domain D1.

By means of different methods, the structure, binding specificity and stoichiometry of AIR-3A were scrutinized in this study. Also, the influence of aptamer presence to cellular levels of membrane bound hIL-6R as well as tolerance of Air-3A integrity for nucleotide modifications were analyzed. In conclusion, these findings suggested a broader spectrum of folding species and targets for AIR-3A than assumed so far. Also, remarkable tolerance towards different pyrimidine modifications was found. Furthermore, the results hinted at a regulatory influence of AIR-3A on endocytosis and trafficking of hIL-6R. This could be an indication for hIL-6R regulation being (directly or indirectly) associated with cellular occurring G-quadruplexes. Against the background of recent advances in the elucidation of G-quadruplex mediated modulations these findings may help to increase understanding of hIL-6R associated dysfunctions.

1. Introduction

1.1. G-Quadruplexes

DNA and RNA can adopt different secondary structures that arise from intra- or intermolecular hydrogen bonding. Most common are helical structures as for example the B-form double helix known from DNA duplexes.¹ Helices can also occur in RNA and in hybrids of DNA and RNA and also in unimolecular oligonucleotides undergoing intramolecular folding. There, other secondary structures as stem-loops, internal loops or bulges can be formed as well.²⁻⁴ Secondary structures are stabilized by stacking interactions.⁵

Another group of higher ordered structures is represented by G-quadruplexes (GQs) found in DNA or RNA rich in guanines. The guanines are arranged as repetitive sequence motifs (G-tracts). The term quadruplex refers to the tetramolecular characteristic of these nucleic acids. Thus, deduced from duplexes and triplexes, a quadruplex (or tetraplex) is composed of four strands. These can either be four separate strands,⁶ a dimer of two strands⁷ or a single strand that forms a GQ by intramolecular folding (unimolecular GQ).⁸⁻¹⁰

While duplex formation results in helical conformations, regardless of the base sequence, by complementary Watson-Crick base pairing, formation and stability of higher order structures is depending on their sequences and more difficult to predict.^{11,12} To form such alternative structures, alternative base pairing is a prerequisite.

1.1.1. Structural properties

Discovery of guanine self-association dates back to 1910 when Ivar Bang discovered that guanylic acid (GMP) formed gels in aqueous solutions.^{13,14} Decades later, in 1962, Gellert *et al.* published X-ray diffraction data for GMP, proposing the tetrameric structure known nowadays as G-quartet or G-tetrad.¹⁵ In G-tetrads, Hoogsteen hydrogen bonding occurs between Gs, which are arranged in a cyclic planar fashion (Figure 1).

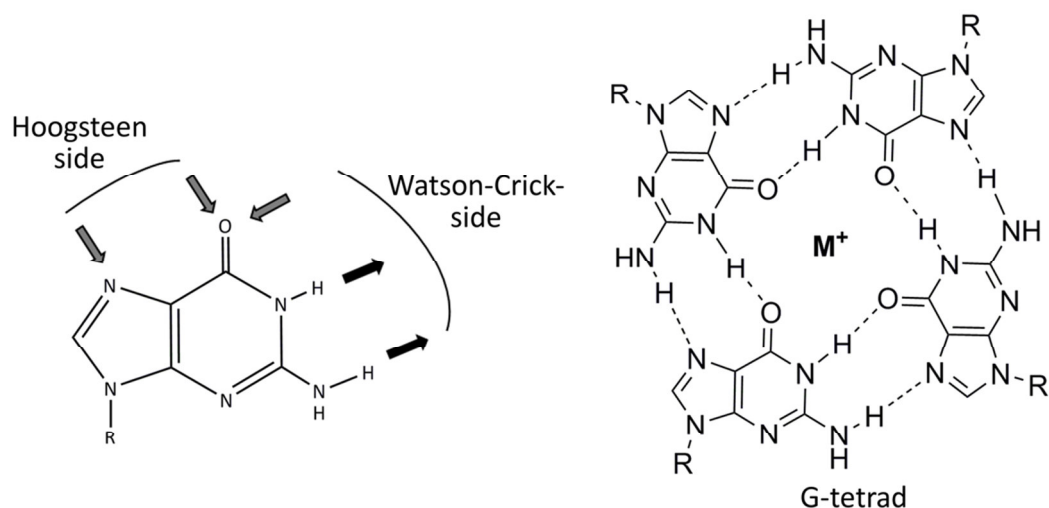


Figure 1: Schematic representation of a G-quartet [modified from ¹⁶]. The planar structure consists of four guanine residues, that interact via Hoogsteen hydrogen bonds (N1-N6 and N2-N7) and is stabilized by complexation of a central cation (M^+).

By stacking, several G-tetrads can form a complex, the G-quadruplex (Figure 3A). To compensate for the negative charge arising from the oxygen atoms, the coordination of monovalent cations (M^+ in Figure 1) is highly favored. Especially potassium and sodium cations have an influence on GQ formation and are often interchangeable, while lithium (Li^+) usually inhibits GQ folding.¹⁰ Due to their radii, Na^+ can be complexed within the plane of a quartet or between two planes, while K^+ is found exclusively in the latter position.^{6, 17} Depending on charge and radius, also other cations are in principle able to intercalate and exchange for K^+ or Na^+ such as ammonium (NH_4^+), barium (Ba^{2+}) and strontium (Sr^{2+}).¹⁸ Cation interaction promotes the GQs stability, which is displayed by their high melting temperatures - relative to nucleotide composition and chain length - and elevated resistance towards nucleases.^{19, 20} GQ stabilizing character was shown to decrease in the order $K^+ > Rb^+ > Na^+ > Li^+ > Cs^+$ for monovalent and $Sr^{2+} > Ba^{2+} > Ca^{2+} > Mg^{2+}$ for divalent cations.^{21, 22} Also, stabilization by trivalent cations Tb^{3+} and Eu^{3+} was reported.^{23, 24} Apart from these inner ions, cations can naturally interact with the phosphate backbone (outer ions) via electrostatic interactions.

Next to cation contribution, stability is further enhanced by stacking interactions between the G-tetrads. Undergoing G-quartet association, guanines experience a change in electron density distribution. This phenomenon is based on the molecular orbital theory and known as resonance-assisted hydrogen bonding (RAHB),²⁵ an interplay of delocalized π -electrons and hydrogen bond (H-bond) formation. However, the RAHB model was recently challenged by the “charge separation” theory,²⁶ which proposes that the GQ stability arises from synergetic effects of H-bond formation and donor-acceptor orbital interactions in the system of σ -electrons rather than π -electrons. Yet, the

redistribution of guanine electron density is consistent with both models. Furthermore, the formation of G-quartets is energetically favored towards free guanines.²⁷

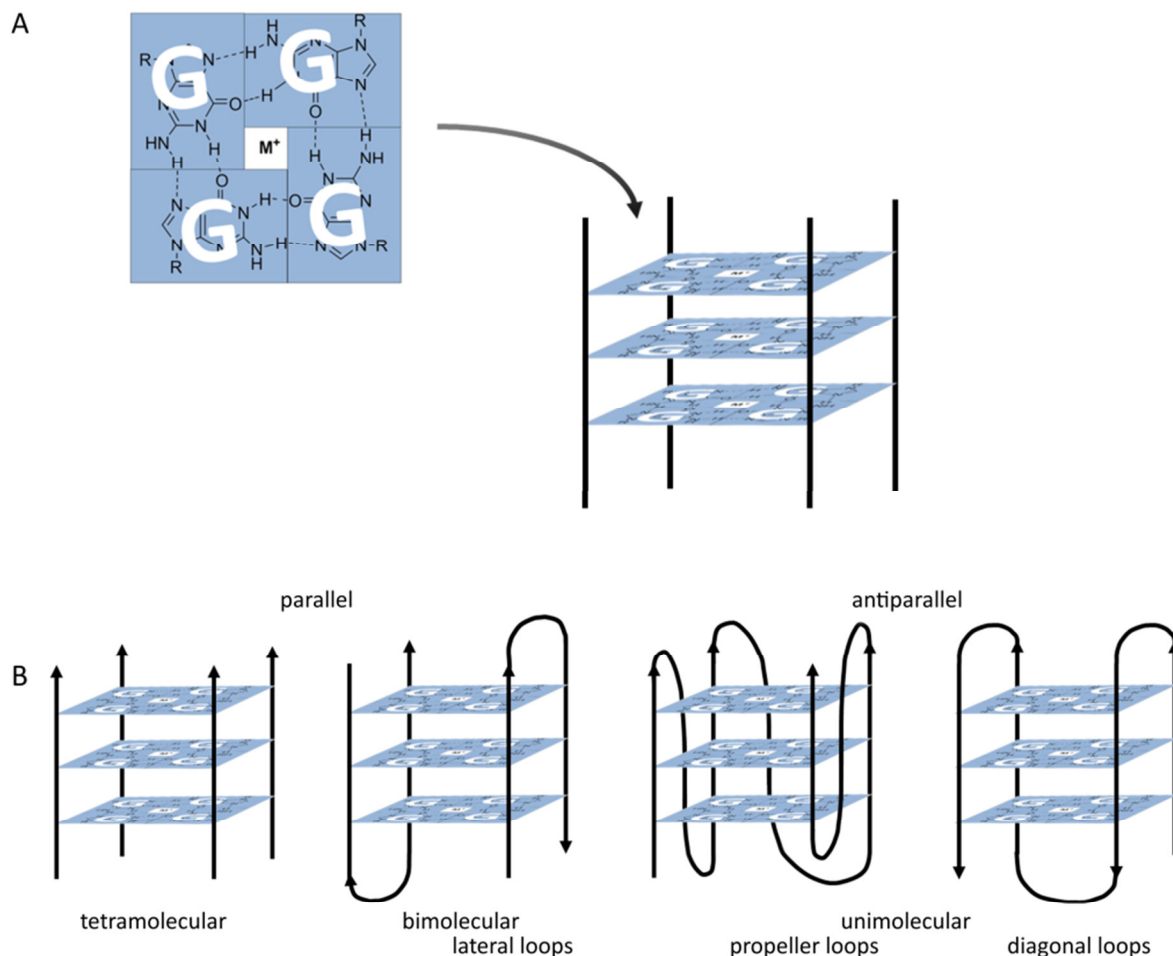


Figure 2: Topologies of G-quadruplexes [modified from Rhodes²⁸]. **A)** Planar G-quartets stack upon each other to form quadruplexes consisting of two or more tiers, according to the G-tracts present in the strand(s). They are stabilized by coordination of cations (M^+) within or between two tetrads. **B)** A selection of possible GQ topologies. GQs can be tetra-, bi- or unimolecular and according to the direction in which the strands run, topologies can be either parallel (same direction) or antiparallel (different directions).

Structurally, GQs can differ in G-tract length, loop or bulge size, strand orientation and topology. The strand(s) forming the GQ can adopt different orientations: parallel (all strands have the same direction) or antiparallel (at least one strand runs in the opposite direction). Further classification is achieved by the location of linking loops (lateral, diagonal or propeller type, Figure 2B).²⁹

In general, longer G-tracts and shorter loops in between result in increased stability.^{10, 30} Folding topologies depend on the molecularity, cation identity, number of G-quartets, nucleotide sequence and glycosidic conformation.³¹ Especially for unimolecular quadruplexes, topologies are diverse (Figure 2B).

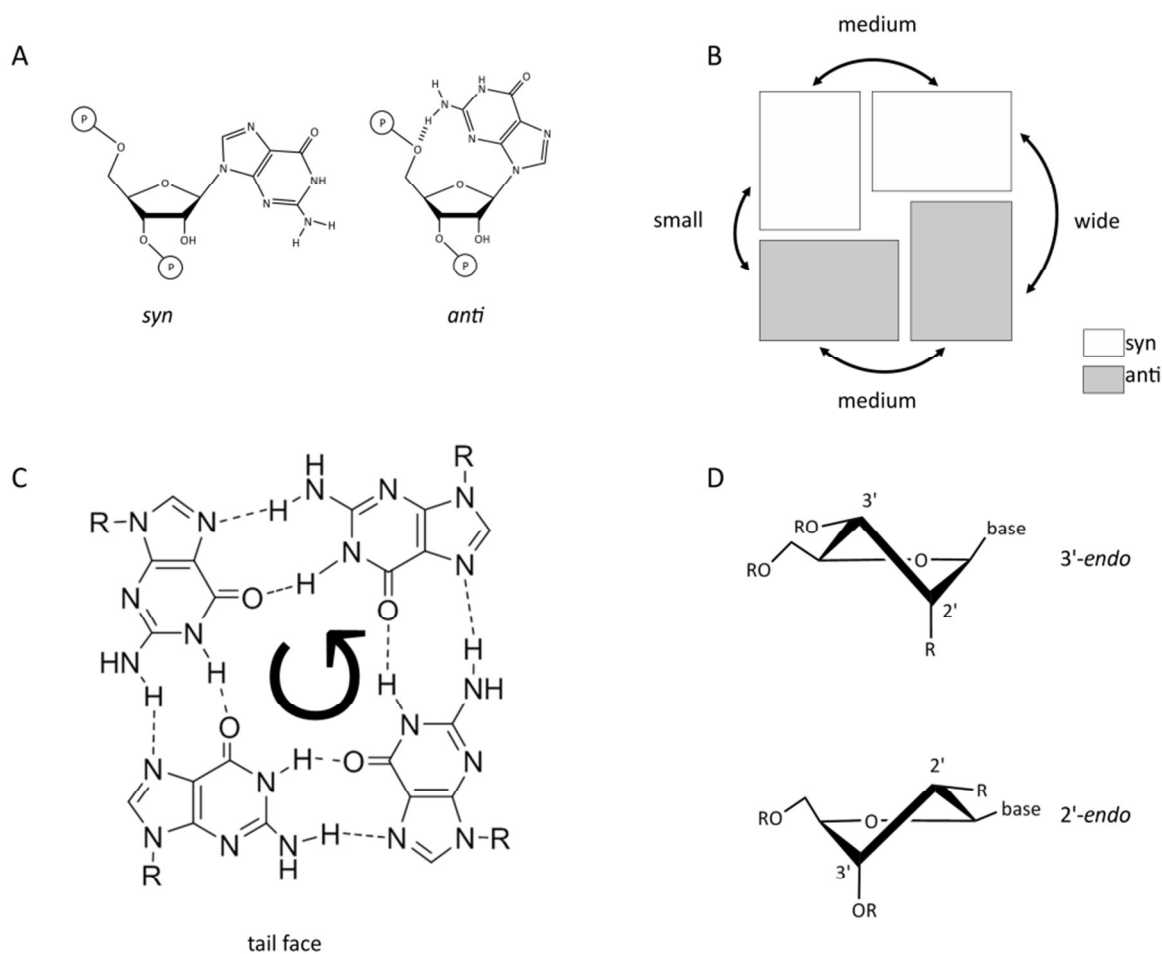


Figure 3: Stereochemical aspects in G-quadruplexes [modified from Tran¹⁶]. **A)** The glycosidic bond between guanine base and sugar moiety adopts either *syn*- or *anti*-conformation (encircled P representing phosphate) with the structural consequence of **(B)** causing different groove sizes (small, medium or wide) between neighboring Gs in the plane. **(C)** The G-tetrad possesses two diastereotopic faces defined by rotation direction of the NH to C=O hydrogen bond: clockwise (*head*) or counter clockwise (*tail*). **(D)** In the G-quartet, favored sugar conformations are either C2'- or C3'-endo.

The glycosidic bond linking guanosines and sugar units in the GQ can adopt either *syn*- or *anti*-conformation (Figure 3A). Also, the sugar can be present in different conformations of which C2'- or C3'-endo are most favorable (Figure 3D). In this respect, RNA is constrained towards DNA by the presence of its 2' hydroxyl group which causes C3'-endo puckering and allows only *anti*-conformation. This also results in RNA G-quadruplexes exclusively adopting parallel folding topology. The 2' hydroxyl also represents a thermodynamic advantage by broadening the scope of intramolecular interaction and stability. The glycosidic conformation also influences the size of grooves defined by neighboring Gs, which can be small, medium or wide (Figure 3B).³²

Moreover, the chiral sugar units attached to all nucleobases transmit and amplify their chirality resulting in a chiral G-quartet with two diastereotopic faces. This means, considering the face of one G-quartet, the direction of N-H to C=O hydrogen bonding can either have a clockwise (head) or counter clockwise (tail) rotation (Figure 3C).^{10, 22}

Over time, related structural phenomena were discovered, for example the occurrence of A₄-, U₄-, T₄- and mixed tetrads, which contribute to quadruplex stabilization.³³⁻³⁶ Also, interlocking or stacking of different GQs were observed.^{37, 38}

1.1.2. Structure analysis of G-Quadruplexes

Under *in vitro* conditions, different structural analyses can be applied to prove the presence of GQs in DNA or RNA. This can be achieved at different orders of resolution depending on the methods used.

On a global level, formation of the quadruplex as well as stoichiometric properties can be analyzed by UV-detected thermal melting or Circular Dichroism (CD) spectroscopy in solution.³⁹⁻⁴¹ Both methods are suitable to detect transitions between duplex and quadruplex formation. CD spectroscopy gives further information on conformational properties such as strand orientation or stacking interactions.

CD spectroscopy exploits the ability of chiral, optically active molecules to differentially absorb circularly polarized light. The difference in absorption of left-hand and right-hand circular polarized light at different wavelength (ellipticity) can be plotted as a function of the wavelength. This results in characteristic bands that allow for structural assignment. In the case of GQs, parallel and antiparallel folding topologies can be discriminated by characteristic bands (Figure 4). Parallel GQs display a minimum absorbance at 240 nm and a maximum at 260 nm, antiparallel topology is indicated by a minimum at 260 nm and a maximum at 295 nm. GQ formation in dependence of different parameters (e.g. temperature or salt concentration) can be monitored and evaluated from the difference in amplitude (e.g. decreasing signal for denatured oligonucleotide (heat), increasing signal at renaturing).

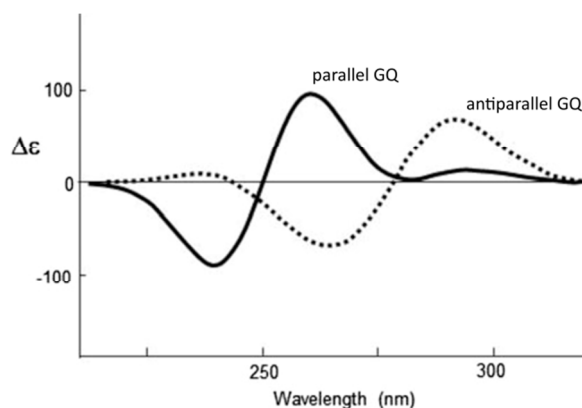


Figure 4: Superimposed calculated CD-spectra of G-Quadruplex forming nucleic acids [modified from Randazzo⁴²]. Exemplary spectra depicting characteristic CD signals. Parallel GQs (solid line) display a minimum at 240 nm and a maximum at 260 nm. Antiparallel folding (dashed line) is characterized by a minimum at 260 nm and a maximum at 295 nm. Amplitude intensity correlates with folding and stacking of the tetrads. Unfolding leads to a decrease in CD signal (curve approaches the baseline).

Structure information at nucleotide resolution can be obtained using secondary structure analyses such as reverse transcriptase stalling, polymerase-stop assay, chemical or enzymatic probing or in-line cleavage susceptibility.⁴³⁻⁴⁷ In general, traditional structure probing analyses that are applied to DNA or RNA are suitable for GQ forming oligonucleotides as well. Briefly, these methods are all based on the generation of oligonucleotide fragments that differ in abundance depending on presence or absence of GQ formation. Quantification of fragment portions under both conditions reveals nucleotides that are influenced by or involved in GQ formation. Fragment analysis can then be conducted by electrophoresis with a sensitive detection method at hand (fluorescence or radioactivity).

Even atomic resolution can be accomplished using methods like NMR or X-ray crystallography.^{43, 48-51} The structural details that these methods provide are impressive. However, high resolution techniques may not be applicable for all GQs as they often demand special sample requirements, such as relatively high concentrations, monodispersity, homogeneity in conformation or laborious preparation (e.g. crystallization) to yield utilizable results.

For interaction studies of G-quadruplexes with cations, ligands or target molecules, a wide array of methods like Filter Retention Assay, Electrophoretic Mobility Shift Assay (EMSA), Flow Cytometry and Microscale Thermophoresis is available. Also Mass Spectrometry (MS) can be employed to study GQs and their interaction partners, while so called native MS additionally provides the possibility to keep the bio-molecules in a near native state allowing for stoichiometry investigations of macromolecular complexes.⁵² The salts that are present in common buffers can interfere with the ionization process of the bio-macromolecule (e.g. a protein) in mass spectrometric analysis. Therefore, in native MS, volatile buffers (such as aqueous ammonium acetate at 5 mM to 1 M) are used that desolvate during

ionization and render bare ions of the investigated molecule. While these are less charged than under standard MS conditions and the folded molecule displays a compact surface, preservation of macromolecular complexes was shown.⁵³⁻⁵⁵

There exist further methods for structural analysis of GQs, which were excellently reviewed for example by Jaumot *et al.* and Murat *et al.*^{56, 57}

Despite the range of possibilities to analyze the structure of a GQ experimentally, bioinformatic modeling approaches add valuable information (e.g. assess thermodynamic interaction probabilities) and are routinely applied in combination. Especially when considering possible therapeutic approaches, it is important to know the structural parameters defining the G-quadruplex and possible interaction sites.³⁸

1.1.3. Biological relevance

Since their discovery, the recognition of G-quadruplexes has evolved from structural curiosities to potential nucleic acid based regulators of multiple biological processes. Advances in sequencing methods and bioinformatics have been to the benefit of this matter. All over genomes and transcriptomes of different species, computational analyses have identified numerous regions that contain potential GQs.⁵⁸ This includes mammals, non-mammals, bacteria and human viruses.⁵⁹⁻⁶¹ Moreover, these sites are not randomly distributed, but co-localize with functional regions such as promoters or telomeres in the genome (Figure 5). There, DNA GQs were found to exhibit regulatory functions, like controlling transcription (Figure 5A) and replication (Figure 5B) due to binding to certain proteins.⁶² Quadruplexes are further present on the RNA level, for example in the 5'-UTR of mRNAs, where they can repress⁶³⁻⁶⁶ or augment⁶⁷ translation (Figure 5D), in 3'-UTRs, where they exhibit regulation by alternative polyadenylation, transcript shortening and miRNA interference,⁶⁸ or in the transcripts of telomeric DNA (TERRA), which contribute to telomere maintenance (Figure 5C).^{69, 70} The site specificity of predicted GQs is also conserved among different species.⁷¹ Recently, a first evidence for GQ occurrence in mitochondria was reported.⁷² While GQs are characterized *in vitro* by their high stability (see 1.1.1), *in vivo* they are often of transient appearance. This is sensible with regard to their suggested function as switches to control biological pathways.²¹

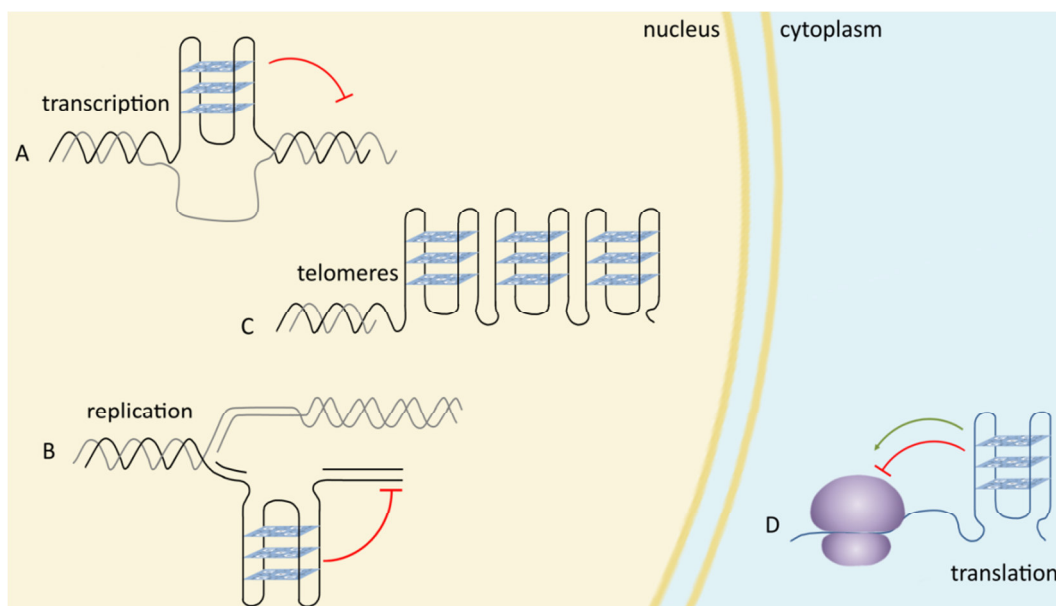


Figure 5: Possible cellular localization of G-quadruplexes [modified from Rhodes²⁸]. Predicted GQ sites in the genome and transcriptome are non-randomly distributed. Their abundance is enriched in regulative regions as promoters and telomeres. GQ formation in the nucleus is supposed to occur in the context of transcription (A) and replication (C) when DNA transiently is unwound, as well as in the G-rich telomeric overhangs that are single stranded (B). Further, involvement is predicted for GQs in mRNA exhibiting translational control in the cytoplasm (D). Red T-bars represent repressive, green arrows progressive influence on cellular processes.

Although GQs likely form *in vitro* under physiological conditions, monitoring of their formation *in vivo* is not as straightforward, despite the abundance of predicted GQ sites. This is because different intracellular parameters can influence GQ-structure and –formation and cause divergence from *in vitro* approaches. As such, state of chromatin condensation or molecular crowding effects need to be taken into account.^{28, 73, 74}

The first proof for the existence of G-quadruplexes *in vivo* was presented for ciliates by Schaffitzel *et al.* in 2001.⁷⁵ Generation of antibodies that specifically bind to parallel stranded GQs allowed for visualization of telomeres by immunostaining in *Stylonychia lemnae*. Similar approaches were then also realized in mammalian cells for example with the antibodies BG4⁷⁶ or 1H6.⁷⁷ Yet, these techniques display the drawback that the antibodies are cell-impermeable and can only be applied on fixed and permeabilized cells.⁷⁶ Thereby detection is limited to GQs in cellular surroundings of limited morphological integrity.⁷⁸ In 2015, Laguerre *et al.* presented an advanced approach.⁷⁸ To detect GQs in live mammalian cells, they used a fluorescent ligand (*N*-TASQ) that exhibits fluorescence only when interacting with RNA GQs. The ligand itself mimics a G-tetrad with guanine residues conjugated to a naphthalene template. Fluorescence is quenched by intramolecular photoinduced electron transfer unless RNA GQs are present. Upon interaction, fluorescence is switched on and enhanced by the intrinsic fluorescence of the GQ.

Application of small molecules that bind GQs also contributed to their identification and isolation.⁷⁹ As an example, pyridostatin was shown to label cellular GQs causing DNA damage. Immuno-detection of damaged sites and chromatin immuno-precipitation followed by deep sequencing revealed genomic GQ sites.⁸⁰ Against this background, small molecules may also be suitable for GQ targeting in therapeutic approaches.

The regulatory potential, discovered for GQs in telomeres^{54, 55} and promotor regions of oncogenes^{51, 81-84} suggests, that they promote cell growth and immortality. Next to potential diagnostic approaches,⁸⁵ this renders them interesting targets for therapeutic applications, especially in the treatment of cancer⁸⁶⁻⁸⁹ as GQ formation can selectively interfere with telomere maintenance in tumor cells.^{90, 91} In the majority of tumor cells, the telomerase enzyme is active, maintaining telomere length and adding to longevity of the cells.⁹² Telomerase levels correlate with state of metastasis and cancer progression.^{93, 94} By means of small molecules, that can stabilize GQs at telomeric ends, inhibition of telomerase was achieved.⁹⁵ Enzymatic inhibition results then in telomere-length reduction, senescence and apoptosis of tumor cells. In a similar approach, small molecule ligands were shown to silence transcription of *MYC* by GQ stabilization in the promotor region of this proto-oncogene.^{96, 97}

1.1.3.1. G-Quadruplex binding proteins

With respect to the regulative potential found for GQs, not only DNA and RNA regions were identified, but also various proteins, that selectively bind GQs (GQ binding proteins) causing stabilization or destabilization.⁹⁸ Groups of targeting proteins were found localized at GQs in the telomere region,⁹⁹⁻¹⁰¹ promotor regions¹⁰²⁻¹⁰⁵ and RNA GQs.^{106, 107} Also, helicases specific for GQ unwinding were identified.¹⁰⁸⁻¹¹⁰ If the recognition proteins become mutated or dysfunctional this may lead to deregulation of GQ interactions which are linked to disorders in aging and disease. Their affinity towards GQs might therefore represent a regulative element. As such, repression of translation was reported for fragile X mental retardation protein (FMRP) upon binding to a GQ in its own mRNA.¹¹¹ FMRP absence, resulting from methylation of a trinucleotide (CGG) repeat in the *FMR1* gene, is associated with inheritable mental retardation.^{112, 113} Mutations in or deficiency of GQ helicases WRN (Werner syndrome ATP-dependent helicase) and BLM (Bloom syndrome protein) are connected to the Werner syndrome (marked by premature aging) and Bloom syndrome (marked by increased cancer incidence, immune and developmental disorders).^{114, 115} Both were reported to be associated with altered transcription of genes possessing predicted GQs.¹¹⁶ Several proteins with GQ binding characteristics were identified and isolated for example by chromatin immunoprecipitation and pull-down assays. General features that are responsible for GQ specificity and common in all binding proteins have not been revealed yet. One characteristic connected with GQ affinity in some proteins is the presence of the stabilizing Arg-Gly-Gly (RGG) repeats as found in FMRP,¹¹⁷ nucleolin (a

multifunctional heterogeneous nuclear ribonucleoprotein (hnRNP) belonging to the family of RNA binding proteins)¹¹⁸ or engineered proteins.¹¹⁹

Next to these examples occurring *in vivo*, G-quadruplexes have also been found in RNAs and DNAs selected *in vitro*. These oligonucleotides called aptamers are dealt with in the following chapter.

1.2. Aptamers

Aptamers are short monomolecular oligonucleotides that display affinity towards a certain target molecule. The target, which can be a protein,¹²⁰ small molecules,¹²¹ metal ions¹²² or even whole cells,¹²³ is recognized with high specificity and effectively bound.

Since 1990, when aptamers were first mentioned,^{124, 125} they have gained more and more importance as versatile tools applied in molecular biology,¹²⁶ nanotechnology,¹²⁷ and medicinal sciences.¹²⁸

In their general properties, aptamers resemble antibodies, but several advantages exist. First, aptamers are less sensitive to heat damage and can refold after denaturation, which results in an overall longer shelf-life and undemanding storage requirements. Also, they can be synthesized cost-efficiently at high yields and low batch-to-batch variation. Another important advantage is that they display little to no immunogenicity and toxicity.^{129, 130}

1.2.1. Generation and applications

Aptamers are generated by an iterative selection process termed Systematic Evolution of Ligands by Exponential enrichment (SELEX)¹²⁵ from a library of monomolecular oligonucleotides diverse in sequences (10^{11} - 10^{14}) with constant terminal primer regions and a randomized central region (20-50 nt). A SELEX can be conducted with DNA or RNA. The unselected pool of oligonucleotides is exposed to the target of interest to allow for binding (Figure 6-1). The binding fraction is then separated from non-binders (Figure 6-2) and eluted from the target molecule (Figure 6-3). Subsequently, binders are amplified (Figure 6-4) by PCR in the case of DNA or RT-PCR for RNA. Finally, to regain a starting pool for the next round of selection, strand separation (DNA) or *in vitro* transcription (RNA) are performed (Figure 6-5). After completion of 5 to 15 SELEX cycles, the pool is investigated for enrichment in binders and aptamers are elucidated by sequence analysis.

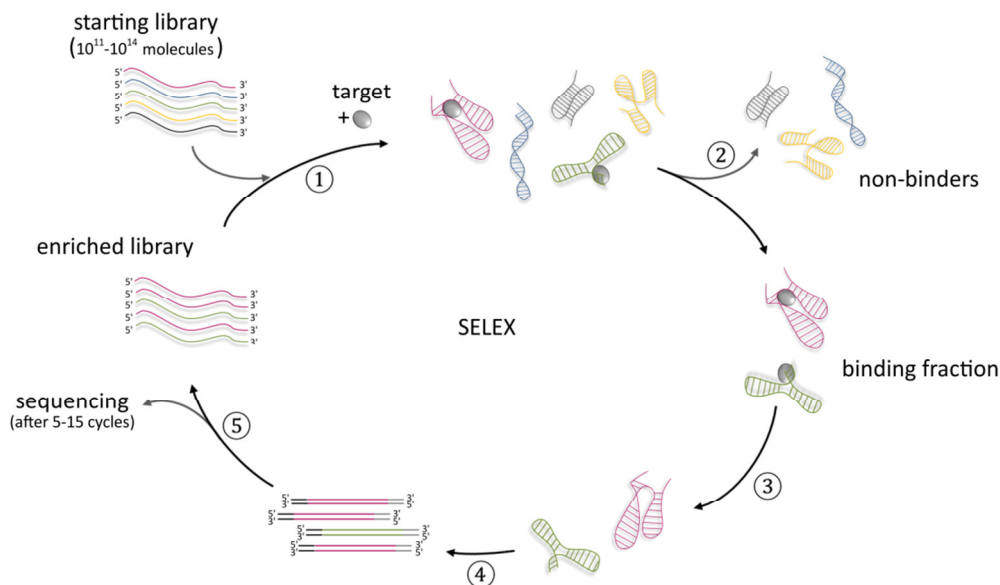


Figure 6: Aptamer generation using SELEX [modified from Kruspe¹³¹]. Schematic depiction of the iterative process used to select aptamers from a diverse starting library of oligonucleotides (DNA or RNA). The library is exposed to the target of interest for binding (1). The non-binding fraction is then separated from oligonucleotides bound to the target (2). Binders are eluted (3) and amplified (4) by PCR (DNA) or RT-PCR (RNA). Generation of the new starting pool is accomplished by single strand synthesis and ready for the next selection round to begin (steps 1-5). Aptamers in the final pool are identified by sequence analysis.

The general experimental setup is adapted to the requirements of the target, selection conditions and planned application. Traditionally, SELEX is performed with the target (e.g. recombinant protein) immobilized on a column or magnetic beads to facilitate separation of the different fractions. Often, a counter-selection step is included to rule out unspecific interactions with the matrix or other components present in the process. Over time, methods were refined to ensure native target conformation and to take into account environmental influences. For example, the targeting of cell-surface molecules can be realized by subjecting the pool to whole cells using cell-SELEX.¹³² This bears on the other hand the risk of concomitant selection of binders for other (unknown) targets.

Depending on the future application, chemical modifications can be introduced to fine-tune aptamer properties. This can either be realized during the selection or post-selectively. A post-selective modification may however result in a decrease or loss of affinity. Prevalent modifications include integration of fluorine- (2'-F) or methoxy-residues (2'-OMe) to enhance stability of the nuclease sensitive oligonucleotides. The stability issue is also tackled by use of enantiomers of naturally occurring RNA called spiegelmers (L-RNA) or locked nucleic acids (LNA) that contain 2'-O-, 4'-C-bridges.¹³¹

In some cases, adaptive chemical conjugation is needed. In that case, reactive groups as thiol- or amino-linkers or linkers offering the possibility to conduct 1,3 dipolar cycloadditions ("click chemistry") can be integrated.¹³³

In therapeutical approaches cholesterol or polyethylene glycol (PEG) are often conjugated with the aptamer to reduce renal clearance.^{128, 134}

1.2.1.1. Aptamers as therapeutics

The aims of selecting aptamers are often directed towards diagnostics or therapy. As almost any target is suitable for aptamer selection, a broad range of possible applications exists. Equipped with a detectable moiety like a fluorescent or radioactive label, aptamer-aided detection of target molecules can be realized for *in vivo* diagnostic imaging or in rapid diagnostic tests, recognizing trace amounts of pathogens or biomarkers *in vitro*.^{135, 136} In the field of therapeutics, either inhibition of molecular interactions that are connected with dysregulation and disease, or targeted drug delivery is aimed at.

Aptamers can induce loss of function in their target upon binding. This may be the case when the binding site is located close to an enzymatic catalytic region or a recognition site for a natural ligand.¹³⁷ They therefore represent useful alternatives to antibodies or small molecules.

Targeted delivery implies that the drug is specifically or preferentially delivered to the site its action is needed and off-target effects are reduced compared to other means of administration. Aptamers are polyanionic and generally unable to pass the cell membrane. Aptamer targets are therefore often found in the extracellular environment. For example, aptamers for coagulatory proteins like thrombin or cofactors involved in the clotting process were selected to operate as coagulants.¹³⁸ Also, molecules on the cell surface, e.g. a biomarker upregulated in a certain malignant cell type or a receptor involved in a dysregulated signaling pathway, are suitable.

To date, only one aptamer has made its way to clinical implementation: Pegaptanib (Macugen, Pfizer). This short, modified RNA aptamer targets vascular endothelial growth factor (VEGF) and was approved by the FDA in 2004 to treat age-related macular degeneration.¹³⁹ Yet there are numerous aptamers that were used in therapeutic approaches with promising results and some that already progressed towards clinical phase studies.^{140, 141} Important candidate targets and their respective aptamers in the focus of cancer research are Prostate Specific Membrane Antigen (PSMA),^{142, 143} Protein Tyrosine Kinase (PTK7),^{131, 144} Epidermal Growth Factor Receptor (EGFR),^{145, 146} Nucleolin,^{147, 148} Transferrin Receptor (TfR),^{149, 150} Mucin 1^{151, 152} or Epithelial Cell Adhesion Molecule (EpCAM).¹⁵³ Importance has also gained aptamer mediated tackling of HIV-1 gp120^{154, 155}

For delivery using aptamers, different effectors can be used as a cargo, as for example various therapeutics including small interfering RNAs (siRNAs), chemotherapeutics, photosensitizers, nanoparticles or proteins. In a first step, the compound needs to be attached to the aptamer. In some cases, non-covalent conjugation is possible, as in case of intercalating drugs (e.g. doxorubicin)

or some siRNAs that can be linked by hybridization. Covalent linkage is often realized by chemical conjugation using a thiol- or amino-modified aptamer to react with carboxylic acid or maleimide residues in the cargo or a linker molecule. Some effectors such as nucleoside analogs can also be introduced during aptamer synthesis which spares later conjugation steps. The method of conjugation should also consider the cellular whereabouts of the delivered compound. In the need to ensure controlled release, it may be necessary to introduce bonds that can be cleaved at intracellular conditions e.g. redox-active disulfides or linkers susceptible to enzymatic degradation.¹³¹

1.2.1.2. Targeted delivery of nucleoside analogs

Nucleoside analogs are a class of therapeutics with competitive potential towards naturally occurring nucleic acids as they possess structural similarities. Thus, they often inhibit enzymes that are involved in modification and processing of nucleic acids and their building blocks (e.g. polymerases, helicases, viral integrases or reverse transcriptases). They are therefore used in the treatment of viral infections as caused by hepatitis- or herpes-viruses or human immunodeficiency virus (HIV).

Also, cytotoxic properties of nucleoside analogs are known. These are exploited as chemotherapeutics for the treatment of cancer, tackling the increased proliferative activity in malignant cells especially on the level of DNA synthesis. As such, for example antimetabolites 5-fluorouracil (5-FU) and 2',2'-difluorocytidine (gemcitabine) represent compounds successfully deployed in the treatment of different types of cancer (Figure 7). While 5-FU is preferentially used in treating colorectal tumors and breast cancer, gemcitabine is applied in pancreatic cancer therapy.^{156, 157} Also, combinatory treatment was investigated for pancreatic cancer treatment.¹⁵⁸

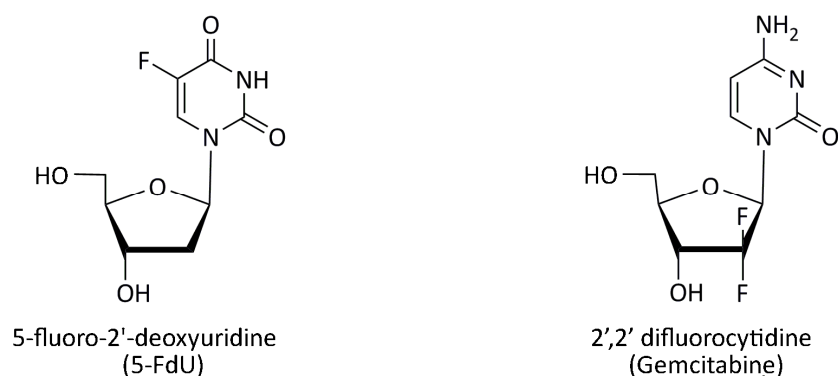


Figure 7: Cytostatic drugs 5-FdU and gemcitabine. 5-FdU and gemcitabine are nucleoside analogs that are applied as chemotherapeutics due to their cytostatic influence on proliferating cells. 5-FdU is characterized by the fluorine derivatization at N5 position. Gemcitabine in turn is fluorine-modified at the 2' position of the deoxyribose.

To minimize adverse side effects, 5-FU and gemcitabine are administered as prodrugs that are activated by enzymatic conversion to therapeutically active drugs inside specific cells.¹⁵⁹

5-FU displays toxicity on different levels. Its triphosphate metabolites 5-F-UTP and 5-F-dUTP can be incorporated in DNA and RNA, causing DNA strand breaks and hampered RNA maturation.^{160, 161} Upon conversion to the monophosphate 5-F-dUMP, it inhibits thymidylate synthase, the key enzyme of thymidine biosynthesis.^{162, 163} Therefore, the derived deoxy-nucleoside 5-FdU is applied as well.

In the case of gemcitabine, active metabolites are the respective mono-, di- and triphosphates dFdCMP, dFdCDP and dFdCTP that interfere with different cell cycle stages. The triphosphate dFdCTP competes with natural dCTP for integration into DNA and, if inserted, causes strand breaks.¹⁶⁴ A unique feature in that case is that subsequently at least one additional natural nucleotide is attached, masking gemcitabine and rendering DNA repair by base excision impossible. In consequence, DNA polymerases are unable to proceed. This feature is referred to as “masked chain termination”.¹⁶⁵ Indirectly, DNA synthesis is also inhibited by dFdCDP which acts as an inhibitor of ribonucleotide reductase (RR).¹⁶⁵ This results in blockage of *de novo* DNA synthesis and enhances gemcitabine activity: as levels of intracellular dNTPs are depleted, dFdCTP incorporation increases as well as formation of active metabolites dFdCMP and dFdCDP due to the missing feedback inhibition of deoxycytidine kinase (dCK) caused by lack of dCTP.¹⁶⁶ Another site of action is the cytidine deaminase (CDD), an enzyme that is responsible for generation of uridine and deoxyuridine by deamination of (deoxy-)cytidine.¹⁶⁷ CDD is directly inhibited by dFdCTP, which results in its decelerated elimination and prolonged intracellular presence and activity.^{166, 167} To some extent, dFdCTP incorporation into RNA occurs as well.¹⁶⁸

Both therapeutics influence the cell cycle by causing S-phase arrest and apoptosis.^{158, 163, 169}

Cellular uptake of nucleoside analogs is usually realized by equilibrative (hENT) and concentrative (hCNT) nucleoside transporters. Gemcitabine and 5-FU/5-FdU are substrates of hENT1, while activated (phosphorylated) metabolites cannot be transported. The influence of hENT1 expression on drug sensitivity and resistance is discussed controversially in the literature.^{170, 171} But though it may have some influence, the contribution of dysregulation of other factors such as apoptosis regulating genes,¹⁷² dCK and RR is probable.^{173, 174} It was shown that pretreatment with 5-FU led to increased sensitivity to subsequent gemcitabine treatment *in vitro* and in a xenograft model.¹⁷⁵

For aptamer mediated delivery, nucleoside analogs possess inherent suitability as they represent nucleic acid building blocks themselves. The aptamer serves as a prodrug and the uptake is not controlled by the presence of nucleoside transporters but on the target. In theory, the aim of specific targeting and decreased off-target effects would be improved towards the systemic administration of the nucleoside analog alone. In 2012, the first aptamer-aided delivery of nucleoside analogs was presented for gemcitabine. EGFR aptamer m07 was annealed to a poly-gemcitabine-oligonucleotide, which was internalized by targeted cells and displayed specific toxicity.¹⁴⁵ In an even more

straightforward manner, delivery of 5-FdU was realized in 2014 by incorporation in hIL-6 receptor specific RNA aptamer AIR-3 (see 1.2.2). The triphosphate 5-FdUTP was used as a substrate during *in vitro* transcription replacing normal UTP. The resulting aptamer prodrug comprised 30 units of 5-FdU per molecule and was shown to induce specific cytotoxic effects on target cells.¹⁶³

Although for clinical application the issue of limited serum stability of aptamers would need to be solved, they represent an elegant way of aptamer mediated delivery.

To deliver the cargo, whatever it may be, cellular uptake is essential. Suitable targets were found to naturally undergo endocytosis and shuttle the aptamer-conjugate bound to it into the cell.

1.2.1.3. Endocytic fate of targets and ligands

Many endocytic pathways exist of which especially clathrin mediated endocytosis is highly abundant and well characterized. Mechanisms independent of clathrin include caveolae mediated endocytosis, macropinocytosis, and phagocytosis.¹³¹

These different pathways can be discriminated by their dependencies on certain cellular proteins or lipids, such as kinases, small G-proteins, actin, or dynamin.¹⁷⁶ Thus, the uptake mechanism can be identified by inhibiting regulating units that are essential for a given pathway.¹⁷⁷ Co-localization with markers that are exclusively or mainly internalized by a certain pathway (e.g. transferrin and its receptor for clathrin mediated endocytosis) enables concomitant investigation of the uptake of a molecule of interest.¹⁷⁸ However, mammalian cells contain multiple pathways, and most endocytic cargos enter the cell by more than one of them.¹⁷⁶

For cell surface proteins, usually active internalization by receptor mediated endocytosis (RME, Figure 8) occurs. For various aptamer targeted proteins including PSMA,¹⁷⁹ EGFR,^{180, 181} and transferrin receptor (TfR),¹⁸² this process is clathrin-dependent.

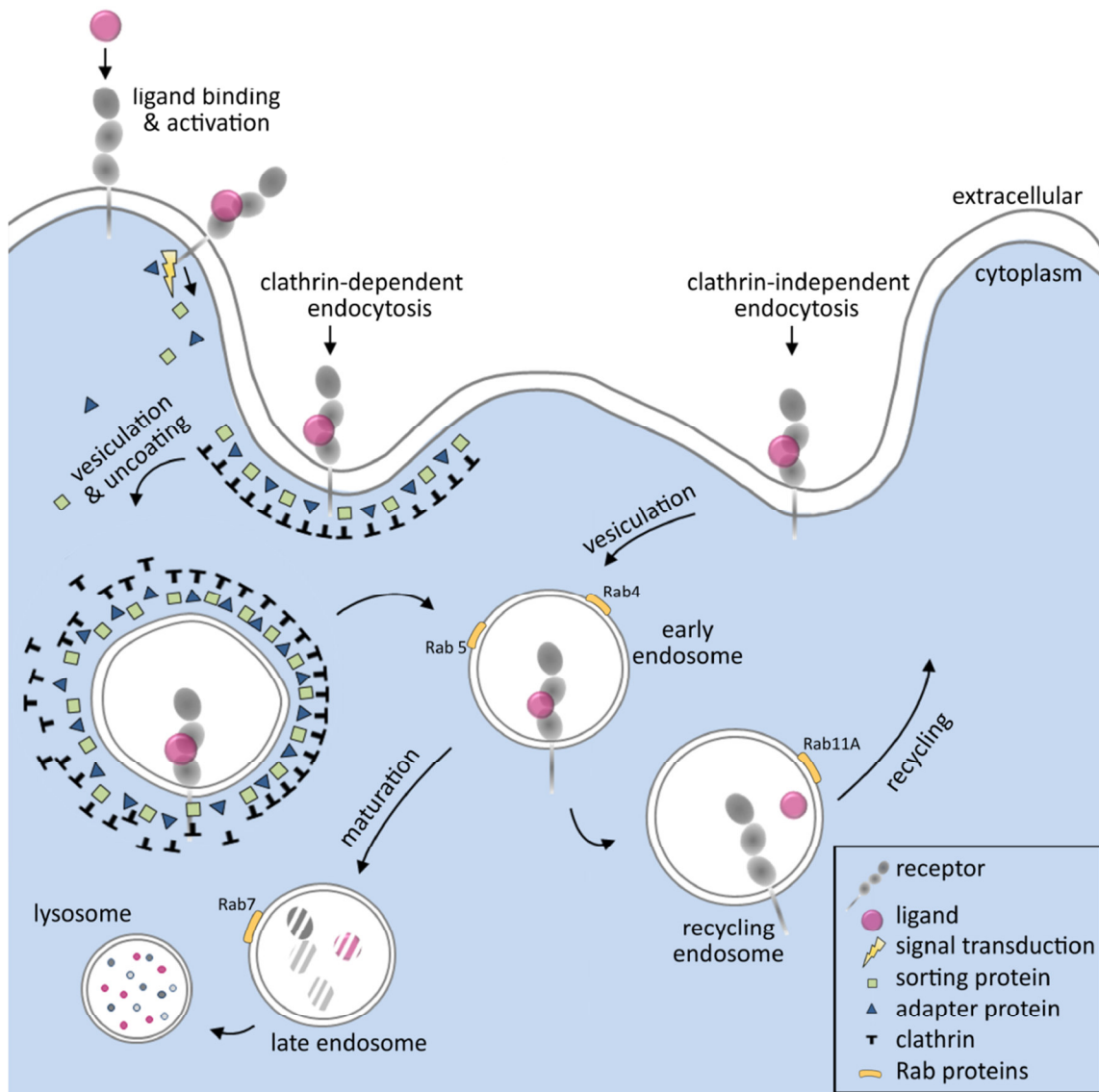


Figure 8: Receptor mediated endocytosis (RME, modified from Traub¹⁸³ and Sorkin¹⁸⁴). Schematic illustration of RME by clathrin-dependent and -independent pathways. Cell surface receptors are activated upon interaction with their ligands. They interact with adapter- and sorting proteins that recruit them to clathrin-coated pits. Dynamin-driven invagination and budding yields the endocytic vesicle. After uncoating, endocytic vesicles from clathrin-dependent and -independent endocytosis fuse to early endosomes. These mature to late endosomes and lysosomes where degradation occurs. An alternative way leads from the early endosome to recycling vesicles resulting in the return of the receptor to the cell surface. Trafficking is controlled by different proteins of the Rab family.

Figure 8 illustrates the RME process: after ligand binding and activation of signaling, receptors are recruited to clathrin-coated pits by interaction with sorting- and adapter proteins, which in turn interact with clathrin. Budding is supported by several accessory proteins and driven by the GTPase dynamin. The clathrin-coated vesicle is uncoated and the internalized receptors with their ligands proceed to the mild acidic early endosome (pH 5.9–6.0). Different Rab proteins (small GTPases of the Ras superfamily) residing in particular types of endosomes control endosomal trafficking by recruitment of effector proteins.¹⁸⁴

Endosomes that contain Rab5 can recycle back to the cell surface with the aid of Rab4 and Rab11A ($t_{1/2} \sim 2.5$ min). Otherwise, endosomes mature to late endosomes (pH 6.0) by acquisition of Rab7 and removal of recycling accessory. Late endosomes fuse with lysosomes (pH 4.5–5.0) for enzymatic or chemical degradation. In the case of clathrin-independent uptake, mechanisms are not yet as well elucidated. The uptake is then dependent on other sets of proteins and structural components. Yet, the pathways unite in fusion of their primary endocytic vesicles with early endosomes.^{131, 184}

Undergoing RME, the cargo delivered to the cell faces the challenge of endosomal escape into the cytosol. Against the background of increasing acidification, the use of acid-labile linkages (hydrazones, imines, and acetals) is sensible to promote the efficacy of drug release by segregation from the aptamer–target complex in the early endosome.¹³¹ Some compounds realize their escape by becoming membrane permeable in slightly acidic environment. This is the case for example for chlorin e6 or doxorubicin, which become uncharged at protonation. To prevent exclusion or degradation of the cargo, in some cases addition of so called “endosomal escape agents” is necessary.¹³¹ These additives lead to disruption of the vesicle and facilitate escape into the cytoplasm. Examples are proton sponges,^{185, 186} membrane-active proteins,¹⁸⁷ peptides,¹⁸⁸ and photochemical internalization compounds.¹⁸⁹ Especially for membrane impermeable therapeutics as siRNAs this has been applied.

Figure 9 summarizes the idea of aptamer-aided targeted cargo delivery. Aptamers conjugated to effector molecules (e.g. drugs, fluorescent dyes or gold nanoparticles) enter the cell bound to their target molecule by receptor mediated endocytosis. Inside the cell, the cargo is released to the cytosol undergoing endosomal escape while the aptamer is degraded.

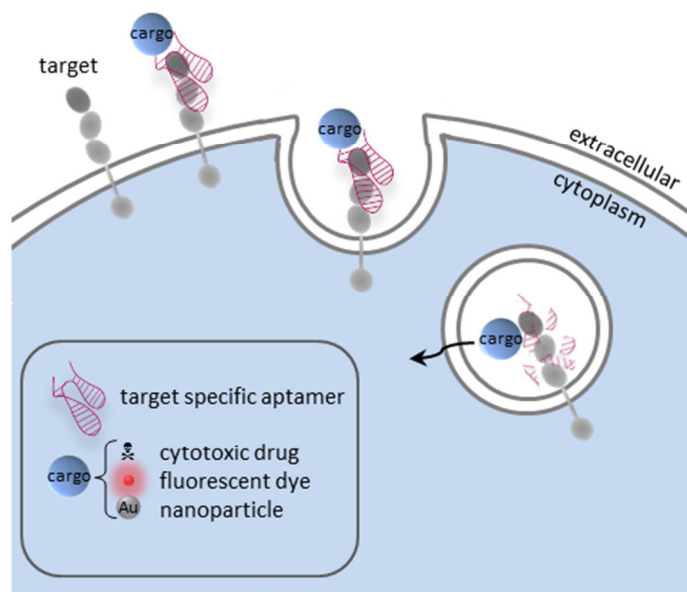


Figure 9: Scheme for endocytic uptake of aptamers for detection and cargo delivery. Aptamers targeting cell surface molecules can be conveyed into the cell by endocytosis. The aptamer's recognition properties provide the delivery to target cells only. The payload conjugated can for example be a drug, a nanoparticle or a fluorescent dye for intracellular detection. To ensure drug release, endosomal escape of the coupled effector needs to be provided.

1.2.2. AIR-3, an hIL-6R specific RNA aptamer

A GQ forming RNA aptamer, selected in 2009 by Cindy Meyer, is the 106 nt aptamer AIR-3^{190, 191} (Figure 10). AIR-3 displays specificity towards human Interleukin-6 receptor (hIL-6R) with a K_d of 20 nM and could be truncated to the binding motif which consists of only 19 nt (5'-GGGGAGGCUGUGGUGAGGG-3').¹⁹⁰ This truncation represents the GQ region of AIR-3 (nt 32 - 51) and was termed AIR-3A. Investigation of AIR-3A revealed high affinity towards recombinant hIL-6R ($K_d = 60$ nM) and cellular presented target protein ($K_d = 8.5$ nM on BaF-3_hIL-6R cells).¹⁹¹

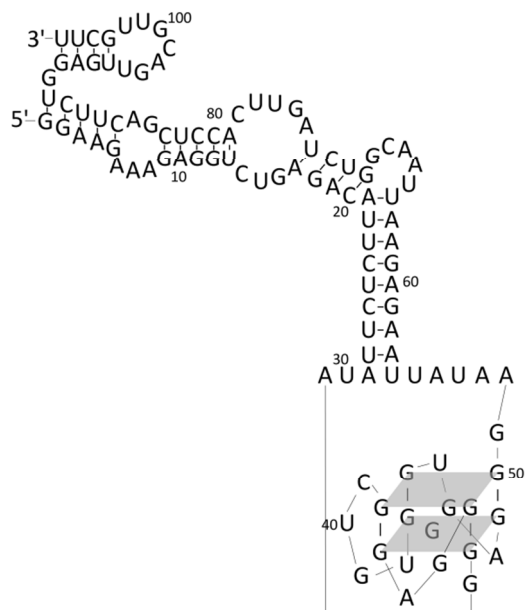


Figure 10: Secondary structure of AIR-3.¹⁹⁰ The 106 nt RNA aptamer AIR-3 with specificity towards human Interleukin-6 receptor forms a GQ as confirmed by thermal melting and CD spectroscopy. Truncation to the 19 nt binding motif in the quadruplex region (nt 32 to 51) represents the variant AIR-3A. Illustration of the hypothesized GQ within the secondary structure of AIR-3 according to Mfold¹⁹² prediction, forcing nt 32 - 50 to be single-stranded.

1.2.2.1. The Interleukin-6 receptor system

Human Interleukin-6 (hIL-6) is a cytokine of the four- α -helix bundle family consisting of 184 amino acids (AA). Cytokines in general are glycoproteins that function as messengers to regulate cell proliferation and differentiation in their environment. They are secreted by different cell types, as for example immune cells, endothelial cells or fibroblasts, and are involved in mediation of inflammatory and immune responses.

Upon interaction with its target receptor hIL-6R, hIL-6 can exert pro- and anti-inflammatory effects that are mainly directed in a paracrine fashion towards hepatocytes, which respond with production of acute phase proteins. Also proliferation and differentiation of B- and T-cells is controlled by hIL-6.^{193, 194}

Mature hIL-6R is a glycosylated 80 kDa membrane protein composed of several domains: a cytoplasmic domain (82 AA), a short transmembrane domain (28 AA) and an extracellular region, also called α -chain (339 AA), consisting of three domains D1-D3 (Figure 11). D2 (Figure 11, green) and D3 (Figure 11, orange) are fibronectin type III-like and mediate interaction with hIL-6. Homology with cytokine-binding domains from other receptors was found. For N-terminal domain D1 (Figure 11, blue), contribution to receptor stability and folding was suggested.¹⁹⁵

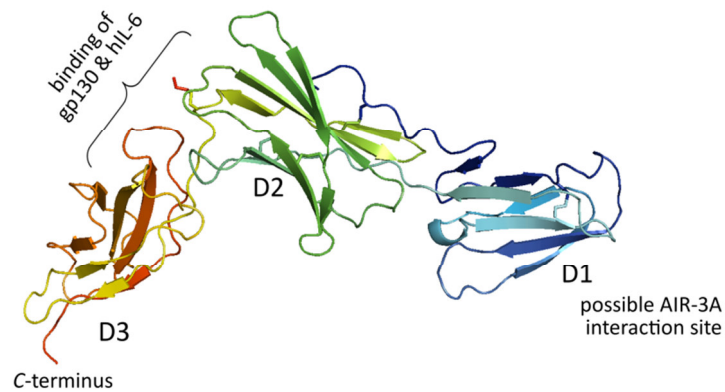


Figure 11: Extracellular domains D1-D3 of hIL-6R (α -chain, PDB: 1N26).¹⁹⁶ Structure of extracellular domains found in hIL-6R α . Binding of hIL-6 and gp130 is mediated by loops located between D2 (green) and D3 (orange). D1 (blue) was suggested for aptamer interaction¹⁹⁷ as well as stabilizing domain.¹⁹⁵

Signal transduction induced by hIL-6 binding requires, next to hIL-6R α , also presence of glycoprotein 130 (gp130), a ubiquitously presented cell surface protein, which functions as co-receptor for other cytokines as well.¹⁹⁸ Assembly of two gp130 molecules with hIL-6R and hIL-6 activates JAK/STAT or MAPK-signaling.¹⁹⁹ Next to this *cis*-signaling, also *trans*-signaling is possible. In that case, a soluble variant (sIL-6R) of hIL-6R α , emerging from shedding (proteolytic cleavage of hIL-6R α) or alternative splicing, interacts with gp130. In this manner, hIL-6 can initiate signaling independently from hIL-6R presence in various cell types.^{200, 201} In 1997, the Rose-John group presented a fusion cytokine of sIL-6R and hIL-6 called Hyper-IL-6 (~68 kDa, 520 AA including a 29 AA peptide linker). It was shown to induce hIL-6 dependent signaling in gp130-positive cells at concentrations 100- to 1000-fold lower compared to combination of the primary proteins.²⁰²

1.2.2.2. Therapeutic targeting of hIL-6 and hIL-6R

Usually, hIL-6 has beneficial functions in inflammation, hematopoiesis and regeneration. If dysregulated, it can however negatively influence pathology and progression of diseases. As such it has a role in rheumatoid arthritis, multiple sclerosis, Crohn's disease and multiple myeloma.²⁰³⁻²⁰⁵

Often, pathologic influence is caused by elevated levels of hIL-6 and sIL-6R. Therapeutic approaches therefore aim at blockage of the protein interactions between these two as well as their interplay with membrane bound hIL-6R and gp130.¹⁹⁴ Inhibition of hIL-6 – hIL-6R interaction was so far successfully realized by application of antibodies Tocilizumab (binding hIL-6R and sIL-6R, approved in 2008) and Siltuximab (hIL-6 specific, approved in 2014) for treatment of inflammatory diseases and Castleman's disease respectively.^{206, 207}

In 2014, also hIL-6 specific aptamers entered the stage in inhibiting interaction with the receptor. The SOMAmers (chemically modified DNA aptamers) SL1025, SL1026, SL1032 and SL1033 were presented

to effectively bind hIL-6, interfere with receptor binding and signal transduction and display high stability in serum.²⁰⁸ In 2015, *in vivo* studies in Cynomolgus Monkeys even showed successful treatment of collagen-induced arthritis with IL-6 aptamer SL1026.

The initial idea for AIR-3 selection was to generate an aptamer with inhibitory potential. Yet, neither AIR-3 nor AIR-3A could compete with hIL-6 or gp130 for interaction with hIL-6R, nor was IL-6 mediated signal transduction influenced by the presence of the aptamer.¹⁹¹

In a follow-up SELEX, selecting for inhibitory potential was tried using hIL-6R domain D3 as a target. Aptamer RAID3 emerged, which could not displace hIL-6 or gp130. Yet, post-selective 2'-F modification was performed with retained affinity for hIL-6R and increased serum stability compared to AIR-3 and AIR-3A.²⁰⁹

In connection with investigation of GQs targeting HIV-1 integrase, sequence identity of a selected hIL-6R DNA aptamer (AID-1) and HIV-1 inhibitor T30923 were discovered. Thus, HIV-1 and hIL-6R were both targeted by AID-1. Against this background, also AIR-3A was investigated for affinity towards HIV-1 and found to inhibit HIV infection at concentrations of 1 μ M. Although no common structural or sequence related features were identified between HIV-1 integrase and hIL-6R, this hinted at a broadened target specificity of AIR-3A and a commonality between the proteins that is not yet understood.²¹⁰

Research on AIR-3A and possible applications went on. For the target cell line BaF-3_hIL-6R, uptake of fluorescently labeled AIR-3A by endocytosis of the targeted receptor was demonstrated and lysosomal fate suggested.^{197, 211}

This cell line was in further approaches used to investigate potential of AIR-3(A) as a vehicle for drug delivery. First attempts, dealing with delivery of siRNAs, had proven ineffective, probably due to failure of endosomal escape and drug release after endocytosis.²¹¹ On basis of these findings, aptamer mediated drug delivery for this system was optimized by Sven Kruspe in 2014. Targeted delivery of photosensitizer chlorin e6 and nucleoside analog 5-fluoro-2'-deoxyuridine were presented and proved AIR-3 and its truncation suitable for application in drug delivery.^{163, 197, 212} In a first attempt to identify the binding site of AIR-3A in hIL-6R, UV cross-linking and mass spectrometry analyses were conducted. The results indicated that domain D1 was involved in interaction with the aptamer.¹⁹⁷ Yet, further proof to this hint is needed. AIR-3A might then have influence on endocytic behavior and intracellular trafficking of hIL-6R, as domain D1 plays a key role in transport through the secretory pathway.¹⁹⁵

1.2.3. G-Quadruplex forming aptamers

Not only AIR-3A, but also other famous aptamers were found to form GQs. This includes for example nucleolin-specific DNA aptamer AS1411,²¹³ thrombin binding aptamer,⁹ HIV-1 aptamer T30177,²¹⁴ aptamers for prion proteins,²¹⁵⁻²¹⁷ Severe Acute Respiratory Syndrome Corona-Virus (SARS-CoV) aptamers²¹⁸ and fluorophore binding aptamer spinach.²¹⁹ In these cases, GQ formation was only discovered during post-selective characterization. It can be assumed that aptamer selections for targets that display general affinity to G-quadruplexes have high probability for GQ forming aptamers to emerge. Recently, selection strategies were presented to increase the GQ yield in the final pool.²²⁰ The idea of combining the benefits of specific targeting by aptamers and intrinsic regulatory potential of GQs is striking. However, the number of identified GQ-binding proteins constantly increases while common features of their binding property remain unclear and categorization is rather conducted according to the type of GQ bound than on the level of protein characteristics.⁹⁸ It was found that some of the proteins targeted by GQ-aptamers possessed a general affinity for GQs. Also, due to their GQ character, some aptamers were prone to bind other proteins next to their target.²²¹

This reflects the inherent ambiguity of including non-specific binding potential to an aptamer for which specific binding is desired. Yet, with the advancing research on GQ-binding proteins and analyses of binding-sites and interaction properties between proteins and GQs, this conflict may be resolved in the future.

2. Aim and motivation

Aptamers binding to cell surface proteins have evolved to sophisticated tools for targeted drug delivery or the inhibition of dysregulated molecular interactions of the target molecule. They thus represent a novel class of therapeutics.

Aptamer AIR-3 was selected in the group of Prof. Dr. U. Hahn for binding to human Interleukin-6 receptor (hIL-6R).^{190, 191} The cytokine hIL-6 and its receptor hIL-6R are involved in the genesis and progression of several inflammatory and autoimmune diseases, as well as in the development of cancer.²⁰³⁻²⁰⁵ Aptamer AIR-3 and its 19 nt truncation AIR-3A bind to hIL-6R presenting cells and are internalized by endocytosis. They also proved effective in drug deliveries using photosensitizer chlorin e6 and nucleoside analog 5-fluoro-2'-deoxyuridine.^{163, 212} The binding motif AIR-3A was shown to form a G-quadruplex (GQ).¹⁹¹

GQs have gained importance during the past years due to the discovery of their abundance throughout the genomes of different species and their regulatory functions discovered for a variety of biological processes.^{44, 63, 83, 107, 222-225}

The aim of the present thesis now was to structurally resolve the folding and tetrad formation of this quadruplex as well as its cation dependency. Also, target interaction and stoichiometry were investigated focusing on the interaction surface on the RNA side. In former works, the aptamer binding site on the protein was identified to be located in hIL-6R domain D1.¹⁹⁷

As D1 had been suggested to play a key role in hIL-6R transport,¹⁹⁵ also the influence of AIR-3A binding on hIL-6R internalization was analyzed as well as its subcellular distribution after endocytosis. In addition, derivatization of AIR-3(A) by nucleotide modifications was conducted. This served as a complement to earlier studies^{163, 226} and aimed at (1st) stabilizing the aptamer towards nuclease degradation by integration of 2'-F- or deoxy-pyrimidines, (2nd) assessing the tolerance towards modifications which retained target affinity and (3rd) evaluating the cytotoxic property of nucleoside analog gemcitabine as a building block of AIR-3 for another drug delivery approach.

3. Materials

3.1. Chemicals

If not stated otherwise, all standard chemicals and materials used in this work were purchased from the companies Merck (Darmstadt), Sigma-Aldrich (Munich), Carl Roth (Karlsruhe) and AppliChem (Darmstadt).

Table 1: Chemicals.

18-crown-6, Crown ether	Merck KGaA, Darmstadt
Acrylamid/Bisacrylamid 19:1 (40%, w/v)	SERVA, Heidelberg
Ammonium persulfate (APS)	AppliChem, Darmstadt
Barium chloride dihydrate	Merck KGaA, Darmstadt
Deoxythymidine	Sigma-Aldrich, Munich
Dichlordimethylsilane	Merck KGaA, Darmstadt
Dimethylsulfoxide (DMSO)	Fluka, Neu-Ulm
Dithiothreitol (DTT)	Thermo Scientific, Schwerte
Ethidium bromide	AppliChem, Darmstadt
Glycogen	Thermo Scientific, Schwerte
Propidium iodide	Sigma-Aldrich, Munich
Resazurin	Biozol, Eching
TEMED	Carl Roth, Karlsruhe
Tris Base	AppliChem, Darmstadt
Tris-HCl	Carl Roth, Karlsruhe
Urea	AppliChem, Darmstadt

3.2. Kits and materials

Table 2: Kits and materials.

BcMag Streptavidin magnetic beads	Bioclone Inc, San Diego, USA
BioSpin® p6-columns	Bio-Rad, Munich
cOmplete™ protease inhibitor	Roche, Mannheim
Cover-glass (24 x 50 mm x 0.13 - 0.17 mm thick)	Brand GmbH+Co KG, Wertheim
Cyto Tox-Glo™ Cytotoxicity Assay, Cat# 9290	Promega GmbH, Mannheim
LysoTracker® Green	Thermo Scientific, Schwerte
Nitrocellulose membrane (0.45 µm)	Carl Roth, Karlsruhe

3.3. Buffers, solutions and media

Table 3: Buffers and solutions for molecular biology techniques.

Name	Composition
Elution buffer	0.3 M Sodium acetate, pH 5.2
FastAP™ buffer (10x)	100 mM Tris-HCl (pH 8.0 at 37°C), 50 mM MgCl ₂ , 1 M KCl, 0.2% Triton X-100 and 1 mg/mL BSA.
FRA equilibration solution (RNA)	20% Methanol, 40 mM 6-aminohexanoic acid
MST buffer (1x)	1x PBS, 0.05% Tween, 1 mg/mL BSA
Orange DNA loading dye (6x)	10 mM Tris-HCl (pH 7.6), 0.15% Orange G, 0.03% Xylene cyanol FF, 60% Glycerol, 60 mM EDTA
PBS (10x)	1.37 M NaCl, 27 mM KCl, 65 mM Na ₂ HPO ₄ , 15 mM KH ₂ PO ₄ (pH 7.5)
Phosphate buffer (10x)	500 mM Na ₂ HPO ₄ , 500 mM NaH ₂ PO ₄ , 1.5 M NaCl (pH 7.4)
PNK-buffer A (10x)	500 mM Tris-HCl (pH 7.6), 100 mM MgCl ₂ , 50 mM DTT, 1 mM Spermidine, 1 mM EDTA
Selection buffer (10x)	10x PBS, 30 mM MgCl ₂
Transcription buffer (3 x)	120 mM Tris-HCl pH 8.1, 15 mM DTT, 6 mM Spermidine, 0.03%(v/v) Triton X-100, 4.5% (w/v) PEG 6000

Table 4: Buffers and solutions for electrophoresis.

Name	Composition
Coomassie destaining solution	45% (v/v) Ethanol, 10% (v/v) Acetic acid
Coomassie staining solution	0,25% (w/v) Coomassie Brilliant Blue G-250, 45% (v/v) Ethanol, 10% (v/v) Acetic acid
Ethidium bromide staining solution	4 µg/mL Ethidium bromide in 1 x TAE
Orange DNA loading dye (6x)	10 mM Tris-HCl (pH 7.6), 0.15% (w/v) Orange G, 0.03% (w/v) Xylene cyanol FF, 60% (v/v) Glycerol, 60 mM EDTA
RNA-loading buffer (2x, denaturing)	95% (v/v) Formamide, 0.025% (w/v) SDS, 0.025% (w/v) Bromophenol blue, 0.025% (w/v) Xylene cyanol FF, 0.025% (w/v) Ethidium bromide, 0.5 mM EDTA
RNA-loading buffer (2x, native)	40% (v/v) Glycerol, 2 x TBE, 0.5% (w/v) Orange G, 0.02% (w/v) Xylene cyanol FF, (K ⁺ in desired concentrations if needed)
SDS-loading buffer (3x, non-reducing)	188 mM Tris-HCl (pH 6.8), 6% (w/v) SDS, 60% (v/v) Glycerol, 0.003% (w/v) Bromophenol blue
SDS-running buffer (1x)	125 mM Tris (pH 8.4), 0.96 M Glycine, 0.5% (w/v) SDS
Separating gel buffer (4x)	1.5 M Tris-HCl (pH 8.8), 0.4% (w/v) SDS
Stacking gel buffer (4x)	0.5 M Tris-HCl (pH 6.8), 0.4% (w/v) SDS
TAE (50x)	2 M Tris-base, 250 mM sodium acetate, 50 mM EDTA (pH 7.8)
TBE (10x)	1 M Tris-base, 1 M boric acid, 20 mM EDTA (pH 7.8)

Table 5: Buffers for RNA fragmentation.

Name	Composition
Alkaline buffer for partial hydrolysis	100 mM Sodium carbonate, 2 mM EDTA (pH 9.5)
Denaturing T1-fragmentation buffer (1x)	7 M Urea, 20 mM sodium citrate (pH 5)
ILP-buffer (2x)	50 mM Tris-HCl (pH 8.3), 10 mM MgCl ₂
Native T1-fragmentation buffer (1x)	10 mM Tris-HCl (pH 7.5), 0.5 mM EDTA

Table 6: Cell culture media and solutions.

Name	Supplier / Composition
Dulbecco's Modified Eagle Medium (DMEM) + L-Glutamin	PAA Laboratories (Marburg)
Fetal bovine serum (FBS)	PAA Laboratories (Marburg)
Freeze medium	90% medium, 10% DMSO
Penicillin/Streptomycin	PAA Laboratories (Marburg)
Roswell Park Memorial Institute Medium 1640 (RPMI-1640) + L-Glutamin	PAN Biotech (Aidenbach)

Table 7: Buffers and solutions for cell-biology techniques.

Name	Composition
Dialysis buffer	20 mM Tris-HCl (pH 7.5), 100 mM KCl, 20% (v/v) glycerol, 0.5 mM DTT, 0.2 mM Na-EDTA
Lysis buffer A	10 mM Tris-HCl (pH 7.5), 10 mM KCl, 1.5 mM MgCl ₂ , 0.5 mM DTT
Lysis buffer B	300 mM Tris-HCl (pH 7.5), 1.4 M KCl, 3 mM MgCl ₂
PI staining solution	0.1% (w/v) Triton X-100, 10 µg/mL propidium iodide, 100 µg/mL RNase A in PBS

3.4. Nucleotides

3.4.1. Nucleoside triphosphates

Table 8: Nucleotides.

ATP, CTP, GTP, UTP; dATP, dCTP, dGTP, dTTP	(Carl Roth, Karlsruhe)
2'-FUTP, 2'-FCTP	(TriLink BioTechnologies, Offenbach)
2',2'-Difluorocytidine-5'-triphosphate, 5-FdUTP	(Jena Bioscience, Jena)
[γ - ³² P]-ATP (3,000 Ci/mmol)	(Hartmann Analytic, Braunschweig)

3.4.2. Oligonucleotides

All synthetic oligonucleotides were purchased desalted from IBA Life Sciences (Göttingen) or Sigma-Aldrich (Munich).

Table 9: Oligonucleotides.

Oligonucleotide	Sequence (5'→3' direction)
AIR-3 (<i>binding motif in italics</i>)	GGAAGAAAGAGGUCUGAGACAUUCUCUUAUAGGGGAGGCUGUGGUGAGG GAAU AUUAAGAGAAUUAACGGUCUAGUUCACCUCGACUUCUGGAGUUGACGUU GCUU
AIR-3A	GGGGAGGCUGUGGUGAGGG
AIR-3A_G17U	GGGGAGGCUGUGGUGAUGG
AIR-3A_Alexa Flour®647	Alexa Flour®647-C ₆ H ₁₂ -GGGGAGGCUGUGGUGAGGG
AIR-3A_G17U_Atto 647N	Atto 647N-C ₆ H ₁₂ -GGGGAGGCUGUGGUGAUGG
AIR-3A_3'-biotin	GGGGAGGCUGUGGUGAGGG-C ₆ H ₁₂ -biotin
AIR-3A_G17U_3'-biotin	GGGGAGGCUGUGGUGAUGG-C ₆ H ₁₂ -biotin
AIR-3_DNA_Alexa Flour®647	Alexa Flour®647-C ₆ H ₁₂ - GGAAGAAAGAGGTCTGAGACATTCTCTTATAGGGGAGGCTGTGGTGAGG GAAT ATTAAGAGAATTAACGGTCTAGTTCACCTCGACTTCTGGAGTTGACGTT GCTT
Pool-RNA	GGAAGAAAGAGGUCUGAGACAUUCU-N60- CUUCUGGAGUUGACGUUGCUU Unselected library (N60 = randomized region)
TBA ²²⁷	dGGTTGGTGTGGTTGG

3.5. Size standards for proteins and nucleic acids

Table 10: Size standards.

O'GeneRuler™ DNA Ultra Low Range Ladder	Thermo Scientific, Schwerte
miRNA Marker	New England BioLabs, Frankfurt am Main
PageRuler™ Unstained Protein Ladder	Thermo Scientific, Schwerte

3.6. Proteins

3.6.1. Enzymes

Table 11: Enzymes.

FirePol® DNA-Polymerase	Solis Biodyne, Tartu, Estland
FastAP™ Alkaline phosphatase	Thermo Scientific, Schwerte
RNase A	Thermo Scientific, Schwerte
RNase T1	Thermo Scientific, Schwerte
T4-Polynucleotide kinase (PNK)	Thermo Scientific, Schwerte
T7-RNA-Polymerase (wild type)	Thermo Scientific, Schwerte
T7-RNA-Polymerase variant Y639F	in house production, Thorsten Mix
Trypsin/EDTA	PAA Laboratories, Marburg

3.6.2. Antibodies

Table 12: Antibodies used for cytometric and microscopic analysis.

Antibody	Host	Supplier
anti-hIL-6R (human)	Mouse, monoclonal	R&D Systems, Wiesbaden
anti-mouse-IgG_APC	Goat, polyclonal	BD Biosciences, Heidelberg
anti-mouse-IgG_FITC	Goat, polyclonal	Sigma-Aldrich, Munich
anti-tetra-His mouse IgG ₁	Mouse, monoclonal	Qiagen, Hilden

3.6.3. Other proteins

Table 13: Further proteins.

BSA	Carl Roth, Karlsruhe
hIL-6	Peprotech, Hamburg
Hyper-IL-6	Conaris Research Institute AG, Kiel
murine Transferrin_Alexa Flour®488	DIANOVA GmbH, Hamburg
shIL-6R	Conaris Research Institute AG, Kiel
Thrombin	CellSystems GmbH, Troisdorf

3.7. Cell lines

Cell lines BaF3/gp130/IL6R/TNF α and BaF3/gp130 were kindly provided from the Rose-John lab (University of Kiel, Germany).

Cell lines KMS-12-BM, RPMI-8226, U-266, PC3 and LNCaP were kindly provided from the lab of PD Dr. F. A. Ayuk (University Medical Center, Hamburg-Eppendorf, Germany).

Cell lines HEK 293 and HeLa were present in the working group of Prof. Dr. U. Hahn.

3.8. Software

Table 14: Software.

Image Lab™ 5.1	Bio-Rad, Munich
CellQuest™ Pro	BD Biosciences, Heidelberg
Quantity One® 4.6.6	Bio-Rad, Munich
GIMP 2.8.14	Spencer Kimball, Peter Mattis
Origin 8.5	OriginLab, Northampton, USA

4. Methods

4.1. Nucleic acid preparation, analysis and modification

Nucleic acid concentrations were quantified photometrically via absorption at 260 nm using a NanoDrop® ND-1000 spectrophotometer. Mass concentrations were calculated by application of the following extinction coefficients:

$$\epsilon_{\text{ssRNA}} = 25 \text{ L} \cdot \text{g}^{-1} \cdot \text{cm}^{-1}, 1 \text{ OD}_{260} \text{ equates to } 40 \text{ ng}/\mu\text{L ssRNA}$$

$$\epsilon_{\text{ssDNA}} = 27 \text{ L} \cdot \text{g}^{-1} \cdot \text{cm}^{-1}, 1 \text{ OD}_{260} \text{ equates to } 33 \text{ ng}/\mu\text{L ssDNA}$$

$$\epsilon_{\text{dsDNA}} = 20 \text{ L} \cdot \text{g}^{-1} \cdot \text{cm}^{-1}, 1 \text{ OD}_{260} \text{ equates to } 50 \text{ ng}/\mu\text{L dsDNA}$$

Ratio of absorptions at 260 and 280 nm was taken as a measure for purity of the sample ($A_{260/280 \text{ nm}} \approx 2.0$).

Experiments including RNA were performed in ddH₂O treated with 1% DEPC.

4.1.1. *in vitro* T7-transcription

RNA synthesis was realized enzymatically using a DNA dependent RNA-polymerase from bacteriophage T7. PCR products or hybridization products of commercially available oligonucleotides including the T7-promotor sequence were used as a template.

Table 15: Composition of *in vitro* T7-transcription reaction.

component	Volume [μL]	Final concentration
DNA template	10	$\sim 0.5 \mu\text{M}$
Transcription buffer (3x)	33	1x
MgCl ₂ [100 mM]	20	20 mM
NTP mix (ATP, CTP, GTP, UTP [25 mM] each)	5	1.25 mM
T7-RNA-Polymerase (wild type)	2.5	> 1 U/mL
DEPC treated ddH ₂ O	ad 100 μL	

Reactions were conducted at 37 °C for 2 to 8 hours. RNAs were gel-electrophoretically analyzed and purified by preparative denaturing PAGE (4.1.3, 4.1.5).

4.1.2. *in vitro* T7-transcription using modified nucleotides

In order to yield RNAs incorporating 2'-F-Py or nucleoside analogs (Gemcitabine or 5-FdU), components from Table 15 were used and exchanged for their respective analogs if needed. Also, T7-RNA-Polymerase variant Y639F was used for synthesis instead of the wildtype enzyme.

Table 16: Composition of *in vitro* T7-transcription reaction using modified nucleotides.

component	Gemcitabine	Gemcitabine+2'FU	5-FdU	Gemcitabine+5-FdU	2'FC+2'FU	final concentration
DNA template	15 μ L	15 μ L	15 μ L	15 μ L	15 μ L	~0.75 μ M
Transcription buffer (3 x)	33 μ L	33 μ L	33 μ L	33 μ L	33 μ L	1 x
MgCl ₂ [100 mM]	20 μ L	20 μ L	20 μ L	20 μ L	20 μ L	20 mM
ATP, GTP [25 mM] each	8 μ L	8 μ L	8 μ L	8 μ L	8 μ L	2 mM
CTP [25 mM]	-	-	8 μ L	-	-	2 mM
2'-FUTP [25 mM]		5 μ L			5 μ L	1 mM
2'-FCTP [25 mM]					5 μ L	1 mM
5-FdUTP [10 mM]			5 μ L	5 μ L		0.5 mM
2',2'-Difluorocytidine-5'-triphosphate [10 mM]	5 μ L	5 μ L		5 μ L		0.5 mM
T7-RNA-Polymerase Y639F	5 μ L	5 μ L	5 μ L	5 μ L	5 μ L	> 1 U/mL
Pyrophosphatase	1 μ L	1 μ L	1 μ L	1 μ L	1 μ L	1 U/mL
DEPC treated ddH ₂ O	ad 100 μ L					

Reactions were conducted at 37 °C for 2 to 8 hours. RNAs were gel-electrophoretically analyzed and purified by preparative denaturing PAGE (4.1.3, 4.1.5).

4.1.3. Polyacrylamide Gel Electrophoresis (PAGE)

Nucleic acids were analyzed and purified using PAGE. For single stranded DNA or RNA, Urea was used as a denaturing agent and ratios of polyacrylamide (PAA) used were adjusted according to the

METHODS

experimental requirements as listed in Table 17 and Table 18. Radical polymerization of acrylamide was initiated by addition of ammonium persulfate (APS) using catalyst tetramethylethylenediamine (TEMED) in aqueous solution.

Table 17: Composition of denaturing PAA-Gels according to their application.

component	analytic	preparative	sequencing gel
TAE buffer	1x	1x	1x
Acryamide/Bisacrylamide 19:1 (w/v)	< 20 nt: 15-20% > 20 nt: 10%	< 20 nt: 15-20% > 20 nt: 10%	< 100 nt: 15% > 100: 12.5%
Urea	8 M	8 M	8 M
TEMED (v/v)	0.1%	0.1%	0.1%
APS (w/v)	0.7%	0.7%	0.7%
Size of gel	130 x 80 x 0.75 mm	245 x 180 x 1.5 mm	210 x 500 x 0.4 mm
Limiting electrophoresis parameter	10 W	10 W	50 W

For analysis under native conditions, gels were prepared omitting urea. For analysis of RNA-protein interactions, an acrylamide/bisacrylamide ratio of 37.5:1 (w/v) was used in native PAGE.

Table 18: Composition of native PAA-Gels for dimerization assays of GQ forming nucleic acids.

component	final concentration
TBE buffer	1x
Acryamide/Bisacrylamide 37.5:1 (w/v)	15%
TEMED (v/v)	0.1%
APS (w/v)	0.7%
KCl	10 mM
Size of gel	130 x 80 x 0.75 mm
Limiting electrophoresis parameter	6.5 V/cm

4.1.4. Detection of nucleic acids

Nucleic acids were detected after electrophoresis from the gel depending on their labeling. Non-labeled samples were subjected to ethidium bromide stain and UV-detection (~325 nm) using Molecular Imager VersaDoc™ (Bio-Rad, Munich). Alternatively, detection of unstained nucleic acids via UV-shadowing was realized exploiting the intrinsic nucleobase absorption against a fluorescent background excited with a UV hand lamp at 254 nm.

Oligonucleotides fluorescently labeled with Alexa Flour®647 or Atto 647N were analyzed by LED-excitation (635 nm) and detection with VersaDoc™ imager (695BP55) or, when in solution, by photometric detection with NanoDrop® ND-1000 (PeqLab GmbH, Erlangen).

When radio labeled, detection of nucleic acids was realized by autoradiography. The matrix (gel or nitrocellulose membrane) carrying radio labeled RNA or DNA was exposed to a phosphor screen which was then read out using phosphor imager PMI FX™ (Bio-Rad, Munich) and analyzed using the corresponding software.

4.1.5. Purification of nucleic acids by diffusion elution after PAGE

After preparative denaturing PAGE (see 4.1.3), bands of interest were detected (see 4.1.4) and excised from the gel. The gel fragment was transferred to a reaction tube, soaked in elution buffer (0.3 M sodium acetate, pH 5.2) and eluted by shaking at 50 °C for 2 h. The supernatant was then transferred to another tube and the purified nucleic acids were isolated by alcohol precipitation.

1 vol of eluate was mixed with 2.5 vol of chilled Ethanol (or 1 vol of chilled isopropanol) and 1 µL of Glycogen (from a saturated solution) and incubated at -20 °C for at least 2 h. Subsequently, centrifugation for 30 min at 4 °C and 16.000 x *g* yielded the precipitate. The supernatant was discarded and the pellet washed with 100 µL of 70% chilled Ethanol by centrifugation for further 10 min. The pellet was then air dried and resolved in ddH₂O.

4.1.6. Radio labeling of nucleic acids 5'-end using ³²P-phosphate

Radioactive labeling of nucleic acids was realized by enzymatic transfer of ³²P-phosphate from [γ-³²P]-ATP to the 5'-end of nucleic acids by Polynucleotide kinase (PNK). As this reaction requires the presence of dephosphorylated 5'-termini, RNAs from T7-transcription (4.1.1 and 4.1.2) were enzymatically dephosphorylated prior to labeling (Table 19).

Table 19: Composition of dephosphorylation reaction of 5'-termini.

component	amount	final concentration
ssRNA or ssDNA	20-200 pmol	2-20 μ M
FastAP™ buffer (10 x)	1 μ L	1 x
FastAP™ Alkaline phosphatase	1 μ L	0.1 U/ μ L
DEPC treated ddH ₂ O	ad 10 μ L	

The mixture was allowed to react for 2 h at 37 °C followed by enzyme inactivation at 75 °C for 15 min.

Commercially available oligonucleotides from solid phase synthesis did not need to undergo this step but were directly used in the labeling reaction.

Dephosphorylated oligonucleotides were enzymatically labeled with PNK from bacteriophage T4 using [γ -³²P]-ATP as a substrate (Table 20).

Table 20: Composition of radio labeling reaction of 5'-termini.

component	amount	final concentration
ssRNA or ssDNA	10-20 pmol	1-2 μ M
PNK-buffer A (10 x)	1 μ L	1 x
PNK enzyme	1 μ L	0.1 U/ μ L
[γ - ³² P]-ATP	2 μ L	1.3 μ M
DEPC treated ddH ₂ O	ad 10 μ L	

The reaction was completed after 45 min incubation at 37 °C. Subsequently, labeled nucleic acids were regained by precipitation with 70 μ L of ethanol (-20 °C, overnight) and centrifugation. Purification was performed by PAGE and diffusion elution (4.1.5).

4.1.7. Stability assessment of RNA molecules

Stability of ^{32}P 5'-end labeled RNA under cell culture conditions was assessed by incubation in DMEM supplemented with 10% FBS at 37 °C. At defined time points, aliquots were taken and immediately frozen in liquid nitrogen. Until electrophoretically analyzed, samples were stored at -20 °C. PAGE separation and analysis by autoradiography revealed remnant amounts of full length RNA. Fragment band intensities were normalized to total counts per lane.

4.2. Protein-biochemical methods

4.2.1. Sodium Dodecyl Sulfate Polyacrylamide Gel Electrophoresis (SDS-PAGE)

Discontinuous, denaturing SDS-PAGE was applied to analyze proteins. Compositions of focusing stacking gel and separating gel are given in Table 21 and Table 22.

Table 21: Composition of stacking gel.

component	final concentration
stacking gel buffer (4 x)	1x
acrylamide/bisacrylamide 37.5:1 (w/v)	4%
TEMED (v/v)	0.1%
APS (w/v)	0.7%

Table 22: Composition of separating gel.

component	Final concentration
Separating gel buffer (4x)	1x
Acryamide/Bisacrylamide 37.5:1 (w/v)	8-15%
TEMED (v/v)	0.1%
APS (w/v)	0.7%

Samples were mixed with SDS-loading buffer (3x) and heated to 95 °C for 2 min.

SDS induced denaturation and negative charge transfer resulting in equal mass-to-charge ratios of all proteins. In consequence, electrophoretic mobility was correlated with the molecular weight.

Electrophoresis was performed in SDS-running buffer (1 x) at 160 V for approximately 1 h.

4.2.2. Detection of proteins by Coomassie staining

Proteins separated by SDS-PAGE were detected by staining with Coomassie Brilliant Blue G-250. Gels were soaked in Coomassie staining solution and incubated under orbital shaking for 3 to 12 h.

Subsequent incubation in Coomassie destaining solution for 1 to 3 h removed background staining and spared detectable stained protein bands.

4.3. Methods for nucleic acid-protein interaction studies

4.3.1. Filter retention analysis (FRA) for RNA-protein interaction

Filter retention assay (FRA) was used to investigate binding of RNAs to recombinant protein. RNAs were radio labeled and purified (4.1.6 and 4.1.5). Constant amounts of labeled RNA (< 1 nM) were incubated with dilution series (0 – 500 nM or up to 2 μ M) of protein in selection buffer (1x). Complex formation was allowed to take place by incubation for 30 min at room temperature. Subsequently, samples were filtrated through a pre-equilibrated (for RNA: 20% Methanol, 40 mM 6-aminohexanoic acid, for DNA: KOH) nitrocellulose membrane (0.45 μ M, Carl Roth) in a vacuum manifold (Minifold® I Dot-Blot-System, Schleicher & Schuell) and washed twice with selection buffer. The membrane was dried and exposed to a phosphor imaging screen (Bio-Rad, 170-7841), read out with Molecular Imager FX and quantified using Image Lab™ 5.1 software (Bio-Rad). From the amount of labeled RNA on the filter related to total amount applied, dissociation constant K_d and maximum binding (B_{max}) values were calculated using Origin 8.5 software (OriginLab Corporation) according to the equation: $RNA_{bound} = (B_{max} \times C_{protein}) / (K_d + C_{protein})$.

4.3.2. Microscale Thermophoresis (MST) for analysis of RNA-protein interaction

MST experiments for stoichiometric investigation of AIR-3A and hIL-6R were performed on a Monolith NT.115 system (NanoTemper Technologies, Munich, Germany) using 10% LED- and 40% IR-laser power. Laser on- and off-times were set at 30 s and 5 s, respectively. A twofold dilution series for unlabeled recombinant target protein sIL-6R (Conaris Research Institute AG, Kiel, Germany) was prepared and equal volumes of AlexaFluor®647 labeled AIR-3A (400 nM) were added resulting in protein concentrations ranging from 10 to 250 nM with a constant AIR-3A concentration of 200 nM in MST buffer (1x PBS supplemented with 0.05% Tween and 1 mg/mL BSA). Samples were incubated at room temperature for 15 min followed by centrifugation at full speed for 15 min to exclude

aggregates. Samples were filled in standard treated capillaries (NanoTemper Technologies) for measurement. Saturation concentration was indicated by the kink in the saturation curve.

4.3.3. Aptamer mediated pull-down of target proteins

Pull-down experiments for protein isolation from cell lysates were performed based on the methods presented by von Hacht *et al.* and Shangguan *et al.*^{107, 228} Briefly, cells were harvested, washed with 1 x PBS and suspended in 1 vol lysis buffer A. After 15 min incubation on ice, cells were centrifuged and pellets suspended in 2 vol lysis buffer A and 1 vol lysis buffer B in presence of cComplete™ protease inhibitor. Protein extracts were obtained by sonification and removal of insoluble cell debris (centrifugation at 10.000 x *g* and 4 °C for 20 min). Overnight extracts were dialyzed against dialysis buffer at 4 °C. For pull-down of proteins, biotinylated RNAs were used as bait, immobilized on streptavidin coated magnetic beads. BcMag Streptavidin magnetic beads (Bioclone, further referred to as “beads”) were washed following the standard protocol prior to the experiment; 100 µL of beads were used per sample. For assessment of unspecific binding, protein extracts (1 mL) were first incubated with beads in presence of 200 pmol biotin only for 30 min at 4 °C. After magnetic separation, supernatants were transferred to fresh tubes containing variant AIR-3A_G17U_3'-biotin (200 pmol) and tRNA (20 µg) and incubated for 30 min at 4 °C. Then, the mixture was added to beads and incubated for further 15 min at 4 °C. This step was conducted to rule out unspecific RNA-protein interaction. Again, magnetic separation yielded the supernatant, which was then transferred to a new tube containing aptamer AIR-3A_3'-biotin. After 30 min at 4 °C, subjection to beads, further 15 min at 4 °C and magnetic separation, all beads were washed four times with 1 mL selection buffer, suspended in 30 µL of SDS-loading buffer (3x) and heated to 95 °C for 20 min to elute bound proteins from the beads. Electrophoretic separation by SDS-PAGE and coomassie staining were performed as described above (4.2.1 and 4.2.2). For analysis by liquid chromatography–mass spectrometry (LC-MS) bands were excised from the coomassie-stained gel and delivered to the *Core Facility Mass Spectrometric Proteomics of the UKE*, N27, Martinstraße 52, 20246 Hamburg. Analysis was conducted by Sönke Harder and Marcel Kwiatkowski from the group of Prof. Dr. Hartmut Schlüter using an Orbitrap Fusion™ Tribrid™ Mass Spectrometer (Thermo Scientific, Schwerte) on the in gel tryptically digested samples (in house protocol).

4.4. Methods for structural analysis of RNA

4.4.1. In-line probing (ILP)

For in-line probing (ILP), 5'-end ³²P-labeled RNA (< 1 nM) in 5 µL of nuclease free water was heated to 95 °C for 1 min and allowed to refold by cooling to room temperature for 5 min. Then, one volume of 2 x ILP-buffer (50 mM Tris-HCl, pH 8.3, 10 mM MgCl₂ and either 200 mM LiCl, 200 mM KCl or 200 mM

KCl and additional 200 nM hIL-6R) was added. Incubation was carried out at room temperature for 36 h. Samples were mixed with an equal volume of RNA-loading buffer (2x, denaturing) and applied on a 12.5 or 15% denaturing sequencing gel (8 M urea). Gels were run at 50 W for 3 to 6 h., frozen and exposed to a phosphor imaging screen and analyzed by autoradiography.

4.4.2. RNase T1 protection assay

For RNase T1 protection assays, samples were prepared with 5'-end ^{32}P -labeled RNA (1 pmol) in native T1-fragmentation buffer (1x), heated to 95 °C for 1 min and cooled to room temperature for 10 min. To a final volume of 10 μL , KCl, LiCl, BaCl₂, NH₄Cl or hIL-6R were added at desired concentrations or 10 mM 18-crown-6 as a “no K⁺” control. Cleavage under native folding conditions was initiated by addition of RNase T1 to a final concentration of 0.005 U/ μL and further incubation for 1 h. Samples were mixed with an equal volume of RNA-loading buffer (2x, denaturing) and applied on a 12.5 or 15% denaturing sequencing gel (8 M urea). Gels were run at 50 W for 3 to 6 h, frozen and exposed to a phosphor imaging screen and analyzed by autoradiography.

4.4.3. RNA sequencing ladders

To assign occurring bands to the nt position, several ladders were generated from ~1 pmol radio-labeled RNA each. A ladder allowing nt resolution was obtained by incubating labeled RNA in 5 μL alkaline buffer for partial hydrolysis at 95 °C for 2 min and quenching by addition of 5 μL Tris buffer (100 mM, pH 7.5). For a denaturing RNase T1 ladder identifying all G positions, RNA was incubated in denaturing T1-fragmentation buffer (1x) at 60 °C for 2 min. 0.5 U/ μL RNase T1 (dilution freshly prepared) were added and the mixture was incubated at 50 °C for 3 min. An RNase A ladder (marking C and U positions) was produced from RNA in 10 μL Tris buffer (100 mM, pH 7.5) by addition of 10 pg/ μL RNase A (dilution freshly prepared). After 2 min incubation at room temperature, reaction was stopped by addition of RNA-loading buffer (2x, denaturing). Ladders were heated to 95 °C for 2 min prior to loading on a 12.5 or 15% denaturing sequencing gel (8 M Urea). Gels were run at 50 W for 3 to 6 h, frozen and exposed to a phosphor imaging screen and analyzed by autoradiography.

4.4.4. Analysis of ILP- and RNase T1 protection-data

For analysis of data obtained from autoradiographic readout of the exposed phosphor screens, bands from sequencing gels were quantified with rectangular boxes around and signals were normalized to total counts per lane. For ILP data, signal intensities for each nt position in the K⁺ or hIL-6R lane were divided by the intensity of the respective position in the Li⁺ lane and plotted against nt position considering the twofold threshold as significant ILP reactivity. T1 protection was evaluated by relating G position intensities to full length intensity (G19 = 1).

4.4.5. Circular Dichroism (CD) Spectroscopy for GQ identification and $K^{+}_{1/2}$ determination

RNAs were prepared at 5 μ M in 10 mM Tris-HCl (pH 7.5) with or without salts added at different concentrations ranging from 100 nM to 100 mM (KCl, LiCl, BaCl₂, NH₄OAc, trimethylammonium acetate (TMAA)), heated to 80 °C for 3 min and allowed to cool on ice for renaturation until measured. CD spectra were recorded using a Jasco J-815 CD spectrometer with a cuvette path length of 0.1 cm. Spectra were acquired at 25 °C every 1 nm from 220 to 320 nm. For each spectrum, ten scans were averaged. Data were buffer subtracted and normalized to provide molar ellipticity values $[\theta]$. Based on the Beer-Lambert law, molar ellipticity $[\theta]$ was calculated from measured ellipticity values θ , path length and RNA concentration (0.000005 mol/cm³).

$$[\theta] = \theta / (0.000005 \text{ mol/cm}^3 \cdot 0.1 \text{ cm}).$$

Titration with cations were conducted in a similar approach as described by Mullen *et al.*²²⁹ To assess the K^{+} concentration at which GQ formation can take place, ellipticity data at wavelength of maximum signal change were plotted as a function of K^{+} and fit with OriginPro 8.5G (OriginLab Corporation software) according to the two state Hill equation:

$$\varepsilon = \varepsilon_F + (\varepsilon_U - \varepsilon_F) / ([K^{+}] / [K^{+}_{1/2}])$$

with ε_U being the normalized ellipticity corresponding to unfolded and ε_F to fully folded GQ, $[K^{+}]$ is potassium concentration and $[K^{+}_{1/2}]$ potassium concentration needed to obtain half the RNA in a folded state.

4.4.6. Electrophoretic mobility shift assay (EMSA) for assessment of GQ oligomerization

For investigation of potassium dependent oligomerization, native gel electrophoresis was conducted as described by Piekna-Przybylska *et al.*²³⁰ 15% polyacrylamide gels were prepared (Table 18) with 10 mM KCl added to gels and running buffer. 5'-end ³²P-labeled RNA (1 pmol) was added to 4 μ M unlabeled RNA in a final volume of 25 μ L. Samples were heated to 95 °C for 3 min, incubated on ice for 1 min and allowed to cool to room temperature. Incubation proceeded at room temperature for 20 h in 10 mM Tris-HCl (pH 7.5), 1 mM EDTA and 100 mM of either KCl or LiCl. For PAGE analysis, one volume of RNA-loading buffer (2x, native) was added to each sample. After electrophoresis for 3 to 6 h at 4 °C and 6.5 V/cm, gels were frozen and exposed to a phosphor imaging screen (Bio-Rad, 170-7841) until analyzed by a Personal Molecular Imager FX™ (Bio-Rad) with Quantity One 4.6.6 and Image Lab 5.1 software (Bio-Rad).

4.4.7. Sample preparation for native mass spectrometry of AIR-3A

RNA was subjected to a desalting procedure prior to native MS analysis in order to remove salt (mainly Na⁺) bound to the RNA by exchange for trimethylammonium (TMA) as a counter ion.

Desalting was adapted according to a formerly presented protocol by Shah *et al.*⁵⁵ Trimethylammonium acetate (TMAA) was applied instead of ammonium acetate as described by Marchand *et al.*⁵²

5.5 nmol AIR-3A in 100 μL of 8 M urea were heated to 65 $^{\circ}\text{C}$ for 5 min. Glycogen was added (20 $\mu\text{g}/\mu\text{L}$ final concentration) as well as 200 μL of 1 M TMAA. The mixture was heated for 1 min at 65 $^{\circ}\text{C}$ and allowed to cool to room temperature. Incubation at room temperature was continued for 1 h. RNA was precipitated by addition of 1000 μL of ethanol and incubation at -20 $^{\circ}\text{C}$ overnight, followed by centrifugation at 16.000 $\times g$ and 4 $^{\circ}\text{C}$ for 75 min. The pellet was air dried for 45 min, dissolved in 200 μL of TMAA, mixed on a vortex for 10 s and heated to 65 $^{\circ}\text{C}$ for 5 min. Another ethanol precipitation was conducted (addition of 600 μL ice cold ethanol, incubation at -80 $^{\circ}\text{C}$ for 5 h and centrifugation for 1 h) and the precipitate was dried at 65 $^{\circ}\text{C}$ for 5 min. Finally, the pellet was resuspended in 10 μL DEPC-treated water and the concentration was determined (4.1). Concentrations of 1 to 100 μM were delivered in 0.5 M TMAA and potassium acetate was added prior to analysis at 200 μM . Sample analysis by native MS was conducted by Boris Krichel at the mass spectrometry facility at *Heinrich Pette Institute* in the group of Dr. Charlotte Uetrecht (Heinrich Pette Institute, Leibniz Institute for Experimental Virology, Martinistrasse 52, 20251 Hamburg, Germany).

4.5. Cell biological methods

4.5.1. Cultivation of eukaryotic cell lines

All eukaryotic cell lines were cultured at 37 $^{\circ}\text{C}$ and 5% CO_2 in presence of 10% FBS, penicillin (60 mg/L) and streptomycin (100 mg/L) if not stated otherwise. Cell cultures were handled under sterile conditions at all times using Herasafe™ KS 2 safety cabinet and sterilized consumables.

- BaF3/gp130/IL6R/TNF α (murine pre-B-cell line, stably transfected to present human proteins gp130, hIL-6R and TNF α on their surface. Cytokine dependent suspension cells. Doubling time: 12 h): subcultivation in DMEM supplemented with hIL-6 (10 ng/mL). Dilution up to 1:100 by renewal or addition of fresh medium every 2 to 3 days maintaining density at $1 \cdot 10^4$ to $1 \cdot 10^6$ cells/mL. These cells are further referred to as BaF3_hIL-6R or target cells.
- BaF3/gp130 (murine pre-B-cell line, stably transfected to present human protein gp130 on their surface. Cytokine dependent suspension cells, hIL-6R negative. Doubling time: 12 h): subcultivation in DMEM supplemented with Hyper-IL-6 (10 ng/mL). Dilution up to 1:100 by renewal or addition of fresh medium every 2 to 3 days maintaining density at $1 \cdot 10^4$ to $1 \cdot 10^6$ cells/mL. These cells are further referred to as BaF3_gp130 or non-target cells.

- KMS-12-BM (human multiple myeloma, suspension cells, hIL-6R positive. Doubling time: 60 h): subcultivation in RPMI-1640 with 20% FBS. Dilution up to 1:2 by renewal or addition of fresh medium every 2 to 3 days maintaining density at $5 \cdot 10^5$ to $1 \cdot 10^6$ cells/mL.
- RPMI-8226 (human multiple myeloma, suspension cells, hIL-6R positive. Doubling time: 60 h): subcultivation in RPMI-1640. Dilution up to 1:2 by renewal or addition of fresh medium every 3 days maintaining density at $1 \cdot 10^5$ to $1 \cdot 10^6$ cells/mL.
- U-266 (human multiple myeloma, suspension cells, hIL-6R positive. Doubling time: 55 h): subcultivation in RPMI-1640. Dilution up to 1:2 by renewal or addition of fresh medium every 3 days maintaining density at $1 \cdot 10^5$ to $1 \cdot 10^6$ cells/mL. Cell clusters formed were resuspended by pipetting.
- PC3 (human prostate carcinoma, adherent cells, hIL-6R positive): subcultivation in RPMI-1640. For passaging, confluent cells were detached with Trypsin/EDTA and diluted 1:3 to 1:10 by addition of fresh medium. Medium change every 2 to 3 days.
- LNCaP (human prostate carcinoma, adherent cells, hIL-6R positive. Doubling time: 60 h): subcultivation in RPMI-1640 with 20% FBS. For passaging, confluent cells were detached with Trypsin/EDTA and diluted 1:3 to 1:10 by addition of fresh medium. Medium change every 2 to 3 days.
- HeLa (Human epitheloid cervix carcinoma, adherent cells, hIL-6R positive. Doubling time: 24 h): subcultivation in DMEM. For passaging, confluent cells were detached with Trypsin/EDTA and diluted 1:2 to 1:6 by addition of fresh medium. Medium change every 2 to 3 days.
- HEK 293 (human embryonic kidney, adherent cells, hIL-6R positive. Doubling time: 30 h): subcultivation in DMEM. For passaging, confluent cells were detached with Trypsin/EDTA and diluted 1:6 to 1:10 by addition of fresh medium. Medium change every 2 to 3 days, maintaining density at $6-7 \cdot 10^4$ cells/mL.

4.5.2. Cryopreservation of eukaryotic cells

For cryopreservation, cells were harvested by trypsinization and/or centrifugation at 4 °C and 300 x g for 5 min. Supernatants were discarded and pellets resuspended in cold freeze medium (composed of 90% complete growth medium supplemented with 10% DMSO). Cell densities were $2-5 \cdot 10^6$ cells/mL. 1 mL aliquots were transferred to 2 mL cryo vials which were incubated in a 4 °C

pre-chilled, isopropanol filled cryo-box at -80 °C for one day. For long term storage, these cryo-stocks were kept in liquid nitrogen vapor phase.

For recultivation, frozen cryo-stocks were transferred to 5 mL of fresh, pre-warmed culture medium and centrifuged for 5 min at 4 °C and 300 x *g*. Supernatants were discarded and pellets resuspended in complete growth medium and seeded in a 25 cm² cell culture flask.

4.5.3. Flow Cytometry analysis

By Flow Cytometry, fast analysis of cellular fluorescence and scattering properties of thousands of cells is possible. Flow Cytometry is a laser-based technique. Application of fluorescent labels allows simultaneous detection of different biomarkers and quantification of their prevalence among the tested cell population. The number of different lasers present in the device and labels used on the sample define the number of properties that can be analyzed simultaneously.

Cells in suspension enter the capillary system of the cytometer within a liquid sheath stream. Single cells are focused to pass the laser beam that excites the fluorescence of interest. Fluorescence intensities obtained from several thousand cells are then processed to multidimensional histograms.

In this work, Flow Cytometry was used to analyze cellular binding of antibodies or nucleic acids as well as cell cycle distribution on a FACScalibur™ Flow Cytometer (BD Biosciences). For histogram plots 10000 to 20000 cells were analyzed.

4.5.4. Fluorescence microscopic analysis

Fluorescence microscopy was performed on a confocal laser scanning microscope (cLSM) LSM 510 ConfoCor2 (Zeiss, Jena) with C-Apochromat 40 x objective (numerical aperture 1.2, water immersion). For analysis, cells were pipetted on a cover-glass (24 x 50 mm x 0.13 - 0.17 mm thick, Brand, Wertheim). Cellular compartment staining, cell-surface binding and trafficking of fluorescently labeled antibodies and RNA were visualized (Table 23).

Table 23: Parameters for detection of fluorescent dyes by cLSM.

Fluorescent dye	Labeled molecule	Method	cLSM paramters
Alexa Flour®647	AIR-3A	subcellular aptamer visualization	laser: 633 nm, 10% laser power, HFT 514/633
APC	secondary antibody	subcellular hIL-6R visualization	NFT 545* LP 650 ph = 200-240 µm
Alexa Flour®488	mTrf	subcellular compartment staining, clathrin mediated endocytosis visualization	
FITC	secondary antibody	subcellular hIL-6R visualization	laser: 488 nm, 6% laser power, HFT 488
LysoTracker® Green	-	subcellular visualization of lysosomes (dye stains acidic compartments)	LP 505 ph = 200-250 µm

*For co-localization experiments

4.5.5. Immunostaining of cell surface proteins

Cell surface protein hIL-6R was detected by means of antibodies. Quantification was realized by Flow Cytometry and subcellular distribution was analyzed by laser scanning microscopy. For immunostaining, $5 \cdot 10^5$ cells were harvested by centrifugation or trypsinization (4.5.1), washed twice with 1 x PBS and resuspended in 350 µL 1x PBS. Cells were kept on ice during the following treatment. 1 µL of primary antibody (anti-hIL-6R or anti-tetra-His mouse IgG₁ (isotype control), final concentration approx. 0.3 ng/µL) was added to the cell suspension and incubated for 30 min. Subsequently, cells were washed with 1 x PBS by centrifugation (3 min, 4 °C, 300 x g) and incubated with 1 µL of secondary antibody (anti-mouse-IgG_APC or anti-mouse-IgG_FITC) in 350 µL 1 x PBS. Finally, cells were washed twice, suspended in PBS and analyzed.

4.5.6. Cellular compartment staining

To study subcellular localization of hIL-6R (APC labeled secondary antibody) and aptamer AIR-3A (Alexa Flour®647), reference staining of lysosomes and clathrin-coated vesicles was performed for co-localization in BaF-3_hIL-6R cells. Lysosomes were detected with LysoTracker® Green, a dye that exhibits fluorescence only in acidic environment. LysoTracker® Green (10 nM) was added to cells

simultaneously as primary antibody or fluorescently labeled aptamer and samples treated as described (4.5.5, 4.5.7).

Clathrin mediated endocytosis was analyzed by monitoring cellular uptake of fluorescently labeled mTransferrin (mTrf_Alexa Flour®488) bound to murine transferrin receptor (mTfR). TfR is known to undergo clathrin mediated endocytosis and serves as a standard control.¹⁸² Similar to lysosomal staining, mTrf_Alexa Flour®488 (10 µg/mL) was added to cell suspensions during incubation with primary antibody or fluorescently labeled RNA and samples treated as described for single staining.

For excitation, red (633 or 635 nm) and blue (488 nm) lasers were used and respective fluorescence channels for concomitant analysis of the pair of dyes.

4.5.7. Cellular binding studies of fluorescently labeled aptamers

For analysis of cellular bound RNA $5 \cdot 10^5$ cells were harvested by centrifugation or trypsinization (4.5.1), washed twice with 1x PBS and resuspended in 100 to 350 µL 1x PBS. Fluorescently labeled RNA (1-200 nM) was added to cell suspensions and incubated on ice for 10 min. To study internalization, incubation was conducted at 37 °C. Subsequently, cells were washed twice with 1x PBS (3 min, 4 °C, 300 x g) resuspended in 100 to 350 µL PBS and analyzed by Flow Cytometry or laser scanning microscopy.

4.5.8. Indirect binding studies of unlabeled aptamers

To assess cellular binding of non-labeled aptamer variants of AIR-3 (e.g. AIR-3-Gem), indirect binding was measured. Affinity was thereby represented as ability for displacement of fluorescently labeled AIR-3A.

Cells were kept on ice/at 4 °C at all times to prevent uptake of cellular bound RNA. $5 \cdot 10^5$ BaF-3_hIL-6R cells were harvested by centrifugation (3 min, 4 °C, 300 x g), washed twice with 1x PBS and incubated with a dilution series of AIR-3-Gem (1-200 nM) in PBS for 20 min. Unbound RNA was removed by washing with PBS followed by incubation with AIR-3A_Alexa Flour®647 (50 nM) in PBS for 20 min. Finally, cells were washed, resuspended in 350 µL PBS and analyzed by Flow Cytometry. Dissociation constant (K_d) and maximum mean fluorescence intensity (B_{max}) were determined from fitting mean fluorescence intensity (F) to corresponding concentration of RNA as described by:

$$F = (B_{max} \times C_{RNA}) / (K_d + C_{RNA}).$$

4.5.9. Cell cycle synchronization by double T-block or single T-block

To ensure homogeneous cell cycle distribution in cell populations prior to drug treatment, BaF3_hIL-6R target cells and BaF3_gp130 non-target cells were synchronized.

Double T block was performed in a similar fashion as described by Roch *et al.*²³¹ Exponentially growing cells were treated with 1 mM deoxythymidine added to the culture medium overnight at 37 °C and 5% CO₂. Cells were washed twice with PBS and resuspended in fresh medium for 2 h. Subsequently, the second block was applied for 4 h with 1 mM deoxythymidine. After washing twice with PBS, cells were released in serum depleted DMEM supplemented with 0.2% BSA and the respective cytokine (hIL-6 or Hyper-IL-6 (10 ng/mL each), see 4.5.1) for further 4 h before fixation and analysis (4.5.12). During this time period, drug treatment was performed (4.5.10).

Alternatively, only one block with deoxythymidine was conducted. In this case, after block one (overnight incubation with 1 mM deoxythymidine) cells were washed twice and cultured for 4 h in serum free DMEM supplemented with 0.2% BSA and cytokine. During this incubation, the corresponding drug could be added. Subsequently, cells were washed and released in complete growth medium for 3 h before fixation.

4.5.10. Aptamer mediated drug delivery of nucleoside analogs

Target cells BaF-3_hIL-6R were washed three times with PBS containing 0.5% BSA and seeded at $1 \cdot 10^5$ cells/well in 100 μ L serum free DMEM supplemented with 0.5% BSA, hIL-6 (10 ng/mL) and 250 nM of one AIR-3 variant containing nucleoside modifications (Gemcitabine, 5-FdU or 2'-F-Py; Table 16, Table 24). After incubation for 3 h at 37 °C and 5% CO₂ to ensure uptake, cells were washed to remove remnant RNA from the medium and cultured in complete growth medium at 37 °C and 5% CO₂. Analysis of cell cycle fractions (4.5.12) or relative cell proliferation (4.5.11) was conducted after culturing times of 4 h or 24 h, respectively.

Non-target cells BaF-3_gp130 were treated in the same way and served as a control to assess off-target effects.

4.5.11. Proliferation assays for toxicity studies

Proliferation of differently treated cells, seeded at 100000 cells/well in a 96-well tissue culture plate, was assayed to assess cytotoxic potential of the respective treatment.

Relative proliferation was measured by addition of redox indicator resazurin. To 100 μ L of cell suspension, 10 μ L of resazurin solution (Biozol, Eching) was added and incubated at 37 °C and 5% CO₂ for 3 to 6 h (depending on cell density) until a color change from blue to purple was visible in the untreated reference sample (100% control). Resorufin, the fluorescent dye ($\lambda_{\text{ex}} = 590$ nm, $\lambda_{\text{em}} = 560$ nm) that live cells produced by reduction of internalized resazurin, served as a measure for viable cell fractions.

In addition, toxicity was assessed using the luminescence based Cyto Tox-Glo™ Cytotoxicity Assay (Promega GmbH, Mannheim) according to the manufacturer's instructions. In this assay, dead cells in the sample were quantified. To 100 µL of cell suspension, 50 µL of Cyto Tox-Glo™ Cytotoxicity Assay Reagent was added, mixed by orbital shaking and incubated at room temperature for 15 min before measuring luminescence. Then, cells were lysed by addition of 50 µL of Lysis Reagent and 15 min incubation, and luminescence measured again to determine total cell number.

Read-out of fluorescence and luminescence signals was conducted in a black, opaque multi well plate using a TECAN Infinite Plate Reader. Relative proliferation was calculated by subtraction of background signals (no-cell control) and relation to viable cells in the 100% control.

4.5.12. Cell cycle analysis

Partial cell cycle fractions were analyzed on fixed cells stained with propidium iodide (PI). $5 \cdot 10^4$ $2 \cdot 10^5$ cells were washed with 1 x PBS and resuspended in 100 µL PBS. By addition of 900 µL of ice cold ethanol (70%) and incubation at 4 °C overnight, cells were fixed. Then, cells were centrifuged (5 min, 4 °C, 300 x g) and all ethanol was removed. Pellets were resuspended in 1 mL PBS and incubated for 60 s at room temperature followed by centrifugation (5 min, 4 °C, 300 x g). The supernatant was discarded and the fixed cells were incubated in PI staining solution (0.1% (w/v) Triton X-100, 10 µg/mL propidium iodide, 100 µg/mL RNase A in PBS) for 10 min at 37 °C.

DNA content was measured by Flow Cytometry detection of PI fluorescence (FL2-H, linear mode). By gating, exclusion of cell debris from laser scattering (FSC vs. SSC dot plot) and cell doublets (false G₂/M signals) from area vs. height plots (FL2-W vs. FL2-H dot plot) was ensured. Quantification of cell cycle fractions was performed by definition of marker regions using CellQuest™ Pro software (BD Biosciences, Heidelberg).

5. Results

In former theses the aptamers discussed herein were investigated and characterized by Cindy Meyer, Katja Eydeler, Eileen Magbanua and Sven Kruspe, who contributed to the selection, characterization and investigation of possible applications.

AIR-3 is a 106 nt RNA aptamer that specifically binds to human Interleukin-6 receptor (hIL-6R) with high affinity ($K_d = 20$ nM). Its truncated version AIR-3A consists of only 19 nt (5'-GGGGAGGCUGUGGUGAGGG-3') that comprise the binding motif which forms a parallel G-Quadruplex (GQ).¹⁹⁰ The target receptor hIL-6R and the signaling pathway that is activated upon binding of cytokine hIL-6 mediate inflammatory and immune responses. Dysregulation of hIL-6R and hIL-6 levels and interaction is also associated with progression and pathology of different diseases.²⁰³⁻

205

For AIR-3 and AIR-3A, no influence on interaction of hIL-6R and hIL-6 or the resulting signaling cascade was found. The aptamers proved however suitable for *in vitro* drug delivery approaches.^{163,}

212

The aim of this research study was to further investigate AIR-3 and AIR-3A in terms of structural properties, target specificity and tolerance of nucleotide modifications such as therapeutically relevant nucleoside analogs. Additionally, the influence of AIR-3A presence on endocytic behavior of target cells was examined.

5.1. Structural investigations

In approaches to determine the general structure of AIR-3, the binding motif AIR-3A was shown to form an all parallel G-Quadruplex with dependence on potassium cation (K^+) concentration.²³²

Here, folding of AIR-3A was analyzed by CD spectroscopy to probe the cation affinity and interchangeability. Subsequent native PAGE and Microscale Thermophoresis (MST) gave insight into intermolecular interactions of AIR-3A such as stoichiometry of RNA and protein upon binding. To determine which of the thirteen guanine bases in this 19 nt RNA took part in tetrad formation, footprinting analyzes including RNase T1 protection and in line probing (ILP) were conducted.

5.1.1. Influence of cations to AIR-3A folding

CD spectroscopic analysis of G-Quadruplex (GQ) formation in the presence of different cations was performed (4.4.5). In order to test the cation influences, different cation concentrations were titrated to constant amounts of RNA.

First, titration of different K^+ amounts to constant AIR-3A concentrations was performed (Figure 12). This experiment gave information on the K^+ dependence of GQ formation as well as the possibility to calculate the K^+ affinity (given as $K^+_{1/2}$). From the difference in ellipticity amplitude at maximum signal intensity wavelength (263 nm), the $K^+_{1/2}$ value could be derived by application of a two state Hill equation ($state_{unfolding} \rightarrow state_{folding}$).

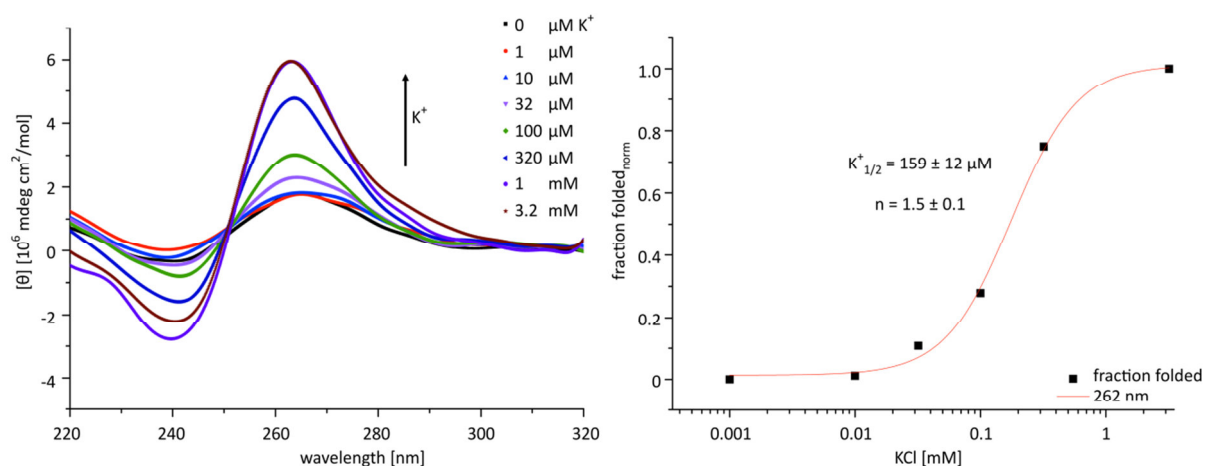


Figure 12: CD spectroscopic analysis of AIR-3A GQ formation in dependence of K^+ . CD spectra (A) and fraction folded plot (B) of 5 μ M AIR-3A in a background of 10 mM Tris-HCl (pH 7.5) in the range of 220 to 230 nm. A) K^+ induced GQ formation on AIR-3A indicates parallel topology by a positive peak at \sim 260 nm and a negative peak at \sim 240 nm. B) Molar ellipticity at $\lambda_{max} = 262$ nm from (A) as a function of K^+ concentration fit to a two-state Hill equation resulting in a $K^+_{1/2}$ value of $159 \pm 12 \mu$ M at $n = 1.5$. Data obtained were averages of ten scans per spectrum from technical duplicates of which the shown plot represents one.

In Figure 12 A, the observed characteristic minima at 240 nm and maxima at 263 nm for each curve indicate the all parallel folding of AIR-3A. Without addition of potassium, the background signal shows only light signals at these wavelengths while a potassium-concentration dependent increase in amplitude to more pronounced bands at $\lambda_{max} = 263$ nm occurs. Normalized ellipticity data at λ_{max} were plotted against $[K^+]$ (Figure 12 B) and a potassium affinity of AIR-3A was calculated with $K^+_{1/2} = 159 \pm 12 \mu$ M, as only one point of inflection was observed indicating one K^+ binding site.

While potassium and sodium are candidates to be most likely coordinated, other monovalent or divalent cations are also able to interact with GQs by either competing for cation binding sites and thereby exchanging with K^+ , or destabilizing GQ integrity.

Therefore, the influence of Li^+ , Ba^{2+} and NH_4^+ on CD spectroscopic behavior of AIR-3A was investigated in a next step (Figure 13-Figure 15). Li^+ is known to interfere with GQ folding in an inhibitory fashion and Ba^{2+} and NH_4^+ can in principle compete for K^+ binding sites due to their similar

ion radii ($\text{Ba}^{2+} < \text{K}^+ < \text{NH}_4^+$).¹⁸ Therefore, Li^+ represents the standard control in face of probing K^+ dependence, while Ba^{2+} and NH_4^+ , in turn, were examined to gain additional information for possible future application in high resolution techniques or native Mass Spectrometry (native MS), respectively.

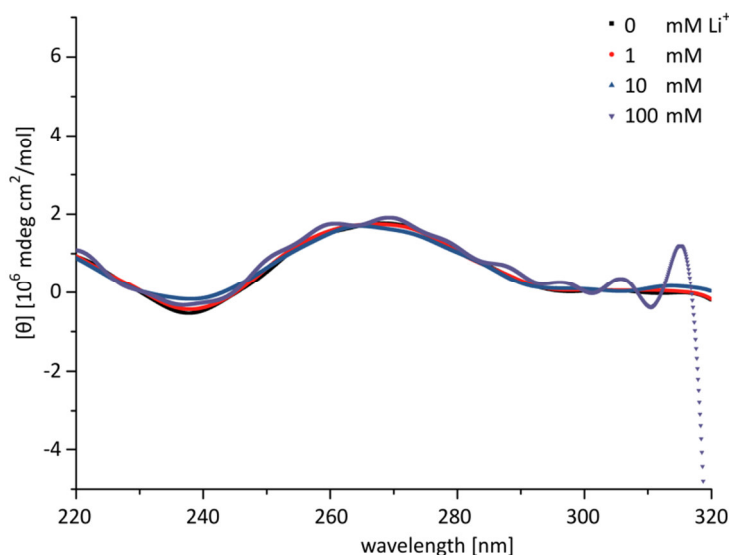


Figure 13: CD spectroscopic analysis of AIR-3A GQ formation in presence of Li^+ . CD spectra of 5 μM AIR-3A 10 mM Tris-HCl (pH 7.5) measured in the range of 220 to 320 nm. Li^+ inhibits GQ formation of AIR-3A as indicated by preservation of background signals independent from Li^+ concentration.

According to the expectations, for AIR-3A in presence of Li^+ concentrations ranging from 0 to 100 mM and absence of K^+ , no difference of the CD intensities was observed (Figure 13). Thus, no GQ was formed, as the characteristic extrema in the curve shape did not appear. This reflects the absence of GQ folding in presence of Li^+ .

Next, Ba^{2+} coordination of AIR-3A was tested. For CD titrations, Ba^{2+} concentrations ranging from 0 to 320 μM were applied in absence of K^+ .

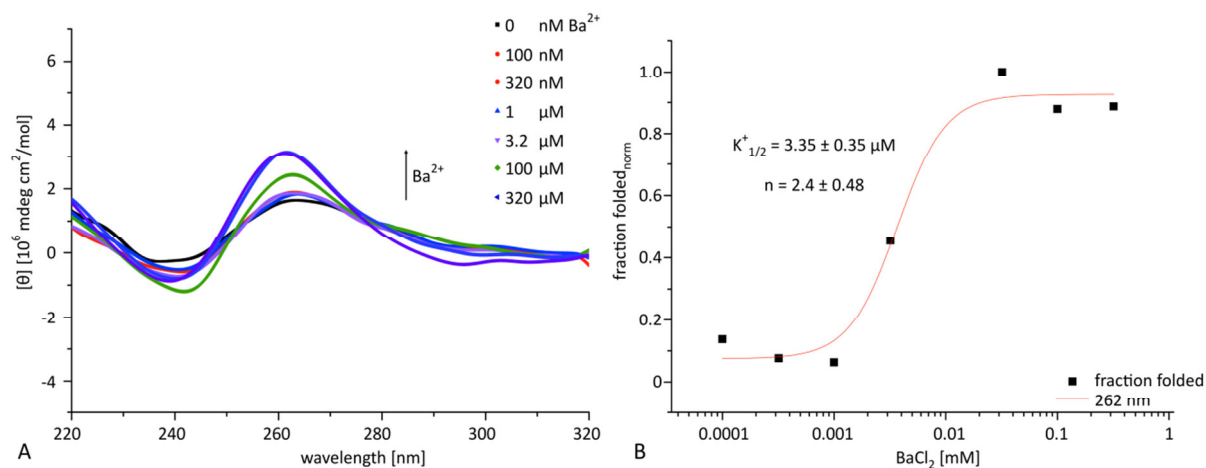


Figure 14: CD spectroscopic analysis of AIR-3A GQ formation in dependence of Ba^{2+} . CD spectra (A) and fraction folded plot (B) of 5 μM AIR-3A measured in a background of 10 mM Tris-HCl (pH 7.5) in the range of 220 to 320 nm. A) Ba^{2+} concentration dependent change of amplitude at ~ 260 nm represents influence on GQ folding. B) Molar ellipticity at $\lambda_{\text{max}} = 262$ nm from (A) as a function of Ba^{2+} concentration fit to a two-state Hill equation yielded a $K_{1/2}^+$ value of $3.35 \pm 0.35 \mu\text{M}$ at $n = 2.4 \pm 0.48$.

In contrast to Li^+ , with Ba^{2+} present in solution, a concentration dependent increase in the amplitude at $\lambda_{\text{max}} = 262$ nm was detected (Figure 14). It could be seen that saturation with Ba^{2+} was reached at lower concentrations (320 μM) compared to K^+ . In conclusion, Ba^{2+} is coordinated with higher affinity, probably due to the twofold positive charge which mediates stronger interaction.

In preparation of native MS analyses, buffer conditions for GQ formation were tested. Most common is the use of ammonium acetate (NH_4OAc), a volatile buffer which was in consequence tested with AIR-3A. In Figure 15A, CD data for AIR-3A in NH_4OAc are shown. As indicated by the similar curves in presence and absence of K^+ , it can be assumed that NH_4^+ exchanges with K^+ . Consequently, this buffer would not be suitable for native MS, but could be substituted with trimethylammonium acetate (TMAA).⁵² As seen in Figure 15B, the obtained signal of AIR-3A in TMAA in CD spectroscopic analysis was back to general background intensity, while addition of K^+ led to a significant increase of the amplitude.

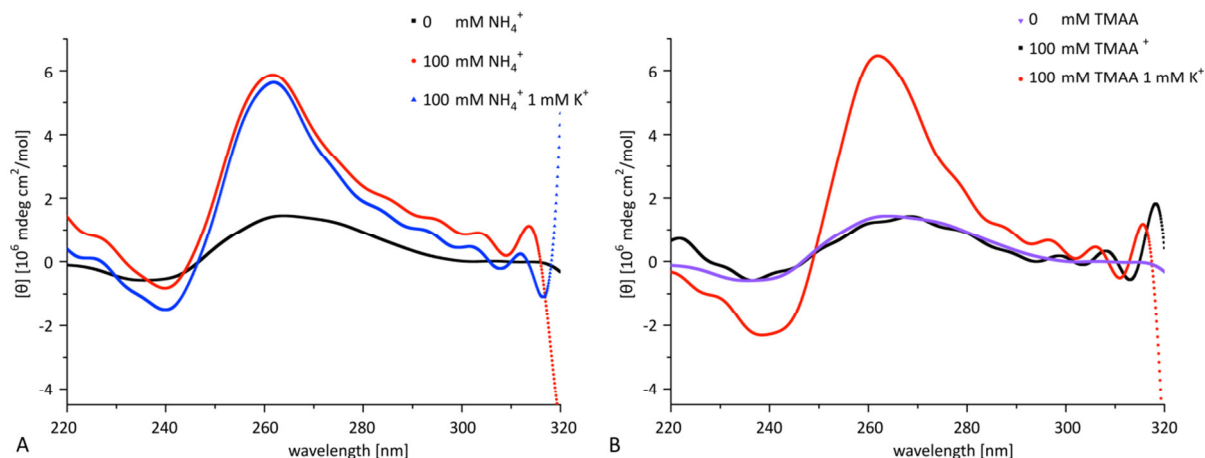


Figure 15: CD spectroscopic analyses of AIR-3A in NH_4OAc and TMAA. A) In presence of ammonium cations, the CD signal intensities, measured from 220 to 230 nm, correspond to a GQ formation (red curve). The signal is hardly influenced by addition of K^+ (blue curve), indicating coordination of NH_4^+ within the GQ. **B)** With TMAA present in solution (purple curve), AIR-3A CD signals superpose with the reference background signal (10 mM Tris-HCl, black curve), while K^+ addition leads to the characteristic bands at 240 nm and 260 nm (red curve).

In summary, dependence of GQ formation on K^+ concentration was found with a $\text{K}^+_{1/2}$ value of 159 μM as well as non-GQ folding of Li^+ . As a proof of principle, it could also be shown that Ba^{2+} is coordinated by AIR-3A, which might offer the possibility of further structural analyses exploiting high resolution techniques such as X-ray crystallography. Finally, buffer conditions for native MS approaches were tested, revealing an unwanted GQ coordination of NH_4^+ cations and suitability of TMAA as alternative buffer system.

On basis of these findings, cation concentrations were adapted in following experiments. And the buffer conditions were applied for evaluation in a pilot experiment using native MS.

5.1.1.1. Native mass spectrometry of AIR-3A

Preliminary data obtained by native MS proved suitability of buffer conditions using TMAA. AIR-3A was desalted and prepared in 500 μM TMAA in presence of 200 μM K^+ .^{52,55} Samples were delivered to the group of Dr. Charlotte Uetrecht at *Heinrich Pette Institute* where native MS was conducted by Boris Krichel. As seen in the recorded spectrum (Figure 16), no single peaks could be discriminated but only clusters were detected. This was probably due to insufficient desalting prior to analysis. Remnant sodium resulted in formation of salt adducts. Therefore, the signals could not be assigned exactly to reveal the number of K^+ cations bound to AIR-3A which would indirectly define the number of tetrads stacked upon each other. The clusters indicated presence of monomeric (Figure 16A and B) and dimeric (Figure 16C) AIR-3A species in solution. AIR-3A has a mass of 6307.89 g/mol and can be differently ionized. Mass to charge ratios detected in the clusters could correspond to monomeric

AIR-3A in complex with one K^+ ($m/z = 1585$ for $[AIR-3A + 1K^+]^{-4}$ or $m/z = 2113$ for $[AIR-3A + 1K^+]^{-3}$) and two AIR-3A for example with 5 K^+ ($m/z = 2565$ for $[(AIR-3A)_2 + 5K^+]^{-5}$), depending on ionization.

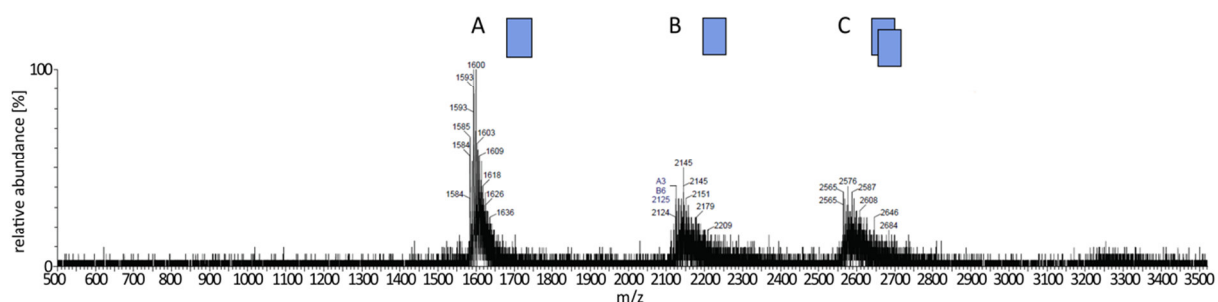


Figure 16: Preliminary data from native MS obtained for AIR-3A in presence of 200 μM K^+ . ESI-MS of 1 μM AIR-3A in 500 mM TMAA and 200 μM K^+ (negative ion mode, low collision). Peak clusters (A, B and C) detected by native MS analysis of AIR-3A resulted from salt adducts. Cluster A and B contained peaks that can be assigned to monomeric AIR-3A in complex with one K^+ . Cluster C represents dimeric species present in solution. Optimization of the desalting procedure would be needed to obtain distinct peaks that give information on the exact number of complexed cations. Samples were prepared in cooperation with Sarah Lemcke and Sven Kruspe. Data collection and analysis by native MS was conducted by Boris Krichel.

Due to the presence of Na^+ other compositions of AIR-3A, K^+ and Na^+ could be interpreted. Therefore, the number of complexed K^+ per AIR-3A was not determinable and optimization of the desalting process would be needed to obtain reliable results. Yet, the presence of dimeric AIR-3A was detected.

5.1.2. AIR-3A assembly and stoichiometry of the aptamer:protein complex

One property of GQ forming oligonucleotides is their ability to oligomerize due to the possibility of intermolecular stacking interactions.⁷

Electrophoretic Mobility Shift Assay (EMSA) is a method commonly applied to detect dimers and oligomers of GQs as it does not affect intermolecular interactions and allows for simple and fast analysis.²²⁹ Native polyacrylamide gel electrophoresis in presence of K^+ and Li^+ was performed to identify higher ordered assemblies of AIR-3A. Therefore, radio labeled AIR-3A with an excess of unlabeled AIR-3A (4 μM) was subjected to long term incubation (20 h) in presence of K^+ or Li^+ to allow complex formation. Figure 17A shows results of native PAGE analysis.

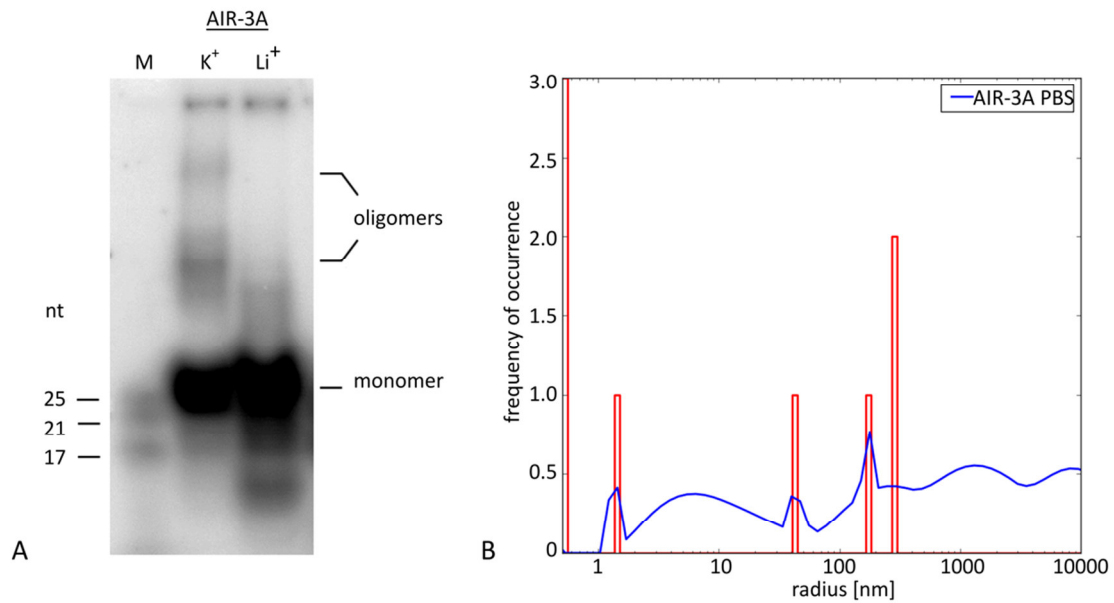


Figure 17: Aggregation of AIR-3A. **A)** Native gel mobility shift analysis (15% polyacrylamide, 1x TBE, 10 mM K⁺) of AIR-3A (4 μ M, 5'-end labeled with ³²P) supports formation of GQ oligomers in presence of K⁺ compared to Li⁺ (100 mM). K⁺ promotes formation of complexes with higher migration behavior. Compared to miRNA Marker (M), monomeric AIR-3A displays higher migration referring to its size (19 nt). This is due to the high G content of the aptamer. **B)** AIR-3A (40 μ M) in 1x PBS was analyzed by DLS. Histogram plot shows severe aggregate formation in solution (measurement conducted by Katharina Berg).

With 100 mM concentration of K⁺, bands of higher migration become visible next to the main band corresponding to the monomer (19 nt). With Li⁺ present, these bands disappear. This is an indication for dimer- and multimerization of AIR-3A. The slight shift above the monomeric band in the Li⁺ lane may be caused by K⁺ present in gel and running buffer (10 mM) causing intermediate complex formation during electrophoresis. For AIR-3A, aggregation at concentrations of 40 μ M was observed as confirmed by dynamic light scattering (DLS) prior to small angle X-ray scattering (see Figure 17B).

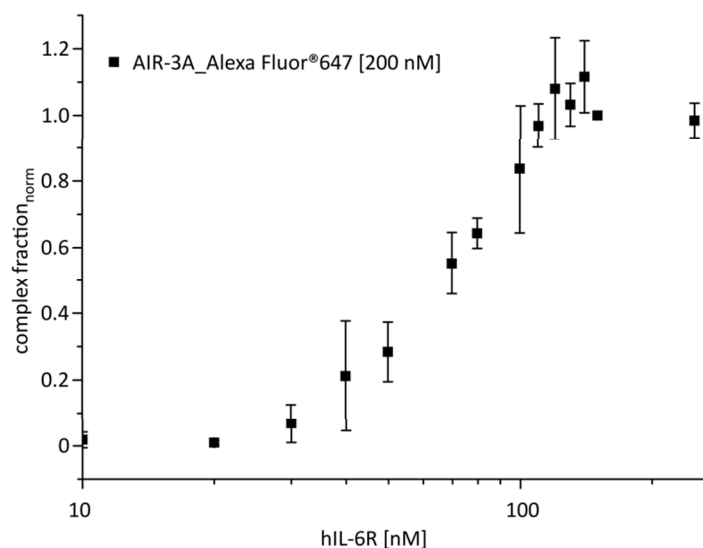


Figure 18: Binding stoichiometry of AIR-3A to human IL-6 receptor. Stoichiometric Microscale Thermophoresis (MST) investigation of fluorescently labeled AIR-3A binding to hIL-6R indicating a ratio of 2:1 of RNA:protein. Plotted data represent mean values from three experiments.

For clarification of stoichiometry of the aptamer:protein-complex, Microscale Thermophoresis (MST, 4.3.2) was performed. To a dilution series of hIL-6R, constant amounts of fluorescently labeled AIR-3A (200 nM) were added to identify the ratio of RNA and protein at saturation concentrations. The displayed curve reached saturation at about 100 nM hIL-6R (Figure 17B). This indicates a stoichiometry of 2:1 and hints at AIR-3A binding to hIL-6R as a dimer, whereas it is also possible that the aptamer targets two different sites of hIL-6R with very similar affinities. In summary, AIR-3A is supposed to form higher ordered assemblies such as dimers and possibly multimers and is likely to also be dimeric in its binding species.

5.1.3. Structure probing analyses

Another aspect that remained unclear during former investigations is the actual structure of the GQ formed by AIR-3A. Bioinformatic calculation of thermodynamic probability of GQ formation, realized by tools such as QGRS mapper,²³³ propose several possible GQs, and mutation analyses led to the choice of one hypothetical structure (Figure 10).²¹¹ While its topology was proven to be all parallel as seen from CD spectroscopic analyses, the identity of the tetrad guanines is still unknown. For modeling approaches of aptamer structure and binding interaction, this information would be valuable. To tackle this matter, structure probing analyses were performed on AIR-3A as well as on the original 106 nt aptamer AIR-3 applying RNase T1 protection assays and in-line probing (ILP), both reflecting protection from cleavage and flexibility of nt within the GQ.

5.1.3.1. Protection from RNase T1 cleavage

RNase T1 is an endoribonuclease with specificity for guanine residues in unpaired RNA strands. It mediates cleavage of the 3'phosphodiester bond resulting in 3'-GMP termini. This nt specificity makes it an ideal tool to probe guanines involved in GQ- and G-tetrad formation, as those positions exhibit protection from cleavage when GQ formation takes place.^{44, 229} Thus, this effect usually is K^+ dependent and increases with K^+ concentration.²²⁹ For RNase T1 footprinting analyses (4.4.2), the influence of different cations and different potassium concentrations on the single guanine positions were analyzed. 5'-radiolabeled (^{32}P) AIR-3A was subjected to RNase T1 cleavage under native folding conditions with K^+ concentrations ranging from 0 to 1 mM, thereby ensuring saturated concentrations according to 5.1.1.

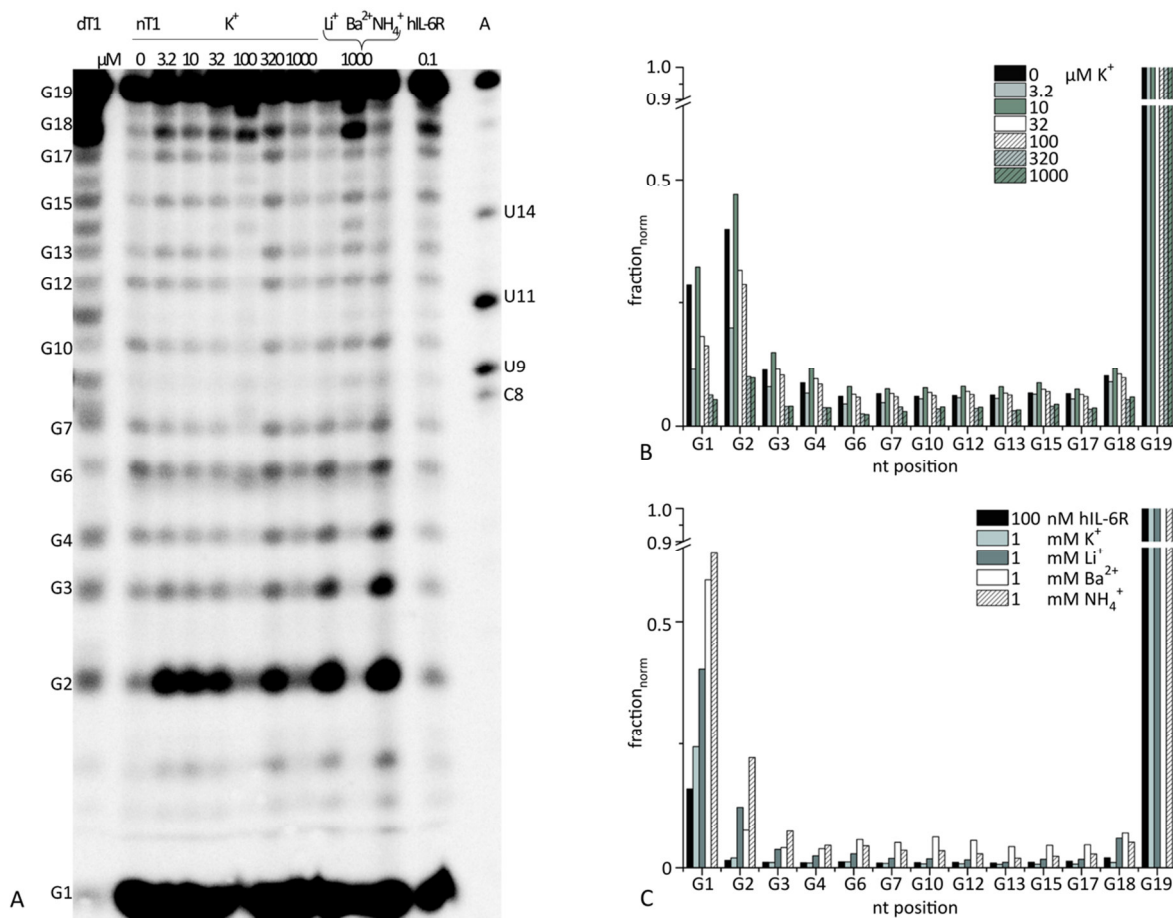


Figure 19: RNase T1 protection assay reveals strong protection of all guanines in AIR-3A. **A)** G-specific T1 cleavage of AIR-3A (5'-end labeled with ^{32}P) under native folding (nT1) conditions (10 mM Tris-HCl (pH 7.5), 0.5 mM EDTA) in presence of different K^+ concentrations, cations and target protein hIL-6R (concentrations as indicated). A denaturing RNase T1 ladder (dT1) and (A) RNase A ladder (C- and U-specific) were applied for band assignment. **B)** T1-protection of different G positions visualized as fractions cleaved in dependence of K^+ revealed overall protection in presence of K^+ , but no significant differences among positions G3 to G18. **C)** T1-protection of G positions in presence of different effectors. Protection increased in the order $NH_4^+ < Ba^{2+} < Li^+ < K^+ < hIL-6R$, whereas no difference among the single positions was observed. For G1 and G2, higher cleavage rates were observed under all conditions. Data were normalized for total counts per lane and in relation to full length present (G19 = 1).

Also, the cations NH_4^+ , Ba^{2+} , Li^+ and target protein hIL-6R were tested for their influence on guanine protection. By denaturing PAGE, obtained fragments were separated in a sequencing gel and analyzed for fragment abundance by autoradiography (Figure 19A).

As shown in Figure 19B, overall protection of guanines as well as an increasing protection of the whole oligo with increasing $[\text{K}^+]$ is visible (decrease in abundance of G1 fragment). Total cleavage in dependence of other effectors decreased in the order hIL-6R > K^+ > Li^+ > Ba^{2+} > NH_4^+ , while cleavage ratios for all positions were ranging in similar quantities except for positions G1 and G2, which seem to be favorable for cleavage in general. Position G19, representing the full length and 5'-end of AIR-3A, could not be probed in this setup due to the lack of a cleavage site for RNase T1. Thus, no information on specific G-positions involved in tetrad formation could be obtained. As there are several possibilities for GQ to fold, due to the large portion of Gs in AIR-3A (68%), it is likely that there are several GQs present at once. AIR-3A is therefore supposed to be polymorphic with no single folding favored. This means that the fragments produced from these different entities overlay with each other, resulting in an apparent pattern of all positions being protected. Another possibility would include AIR-3A to form a three tier bulged QG (see Figure 45).

5.1.3.2. Flexibility of nucleotides in the GQ motif

The findings from RNase protection assays gave cause to investigate the flexibility of all nt positions within the GQ and also the adjacent regions. Therefore, in-line probing (ILP; 4.4.1) was used. This probing technique monitors the susceptibility of nucleotides in a structured RNA for hydrolysis (so called in-line cleavage) due to long term incubation under alkaline conditions (36 h at pH 8.3).⁶⁴ It is applied on GQs to identify increased cleavage in loop regions in presence of K^+ compared to Li^+ and represents a valuable complement to RNase protection assays. ILP was conducted on AIR-3A, but also on AIR-3 to include positions G1 and G19 and probe the GQ in its original flanking sequences. In AIR-3, the 19 nt GQ element is found within nt-position 32 to 50 (see Figure 10). ILP was conducted in presence of Li^+ , K^+ and target protein hIL-6R on 5'-radiolabeled (^{32}P) RNA. Fragments were separated in a denaturing sequencing gel and analyzed by autoradiography. Results from ILP analysis are summarized in Figure 20 and Figure 21, showing only AIR-3 data, but which are in accordance with AIR-3A probing analyses.

RESULTS

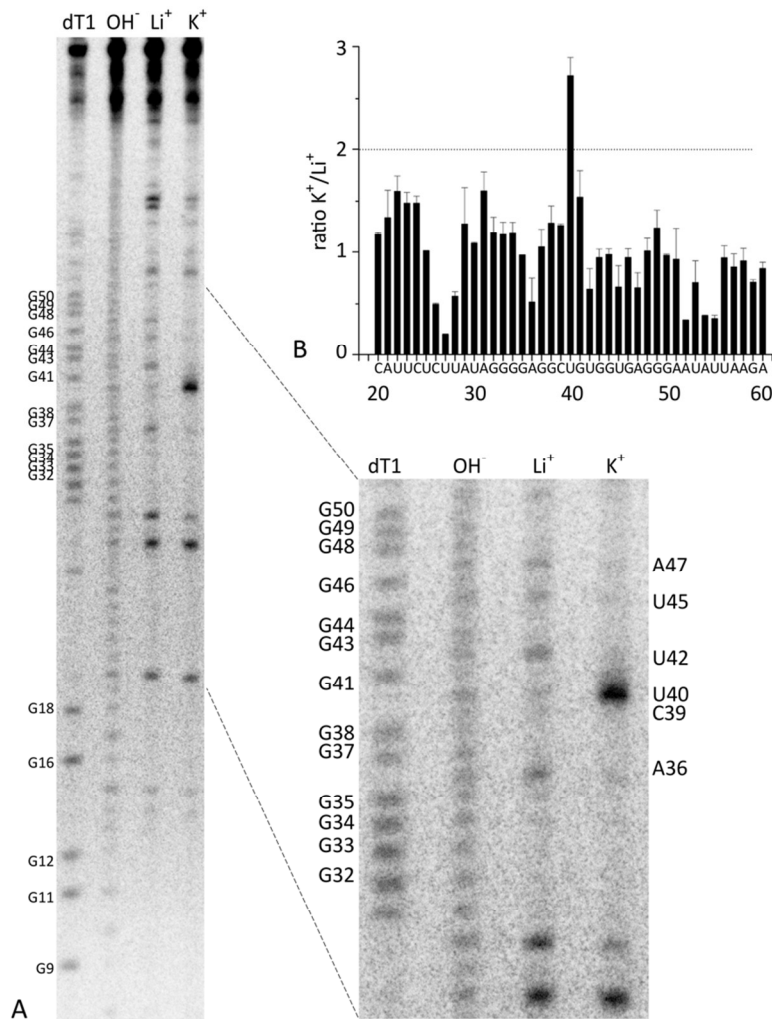


Figure 20: In-line probing (ILP) suggests loop formation in GQ region of AIR-3 in presence of K⁺. **A)** ILP on relevant regions of AIR-3 (5'-end labeled with ³²P, GQ motif formed by nt 32 to 50). Reference ladders dT1 (G-specific) and OH⁻ (alkaline hydrolysis, all positions) were used for band assignment. GQ identity is given by different cleavage patterns in presence of Li⁺ and K⁺, respectively. ILP conditions were 25 mM Tris-HCl, pH 8.3, 5 mM MgCl₂ at room temperature for 36 h with 100 mM Li⁺ or K⁺ present. The GQ region is highlighted as expanded region with Gs assigned on the left and nucleotides in between on the right. **B)** Analysis of ILP results representing ratios for each nt position in lane K⁺ to lane Li⁺ (data were normalized for total counts per lane, normalized band intensities in lane K⁺ or hIL-6R were divided by respective intensity in lane Li⁺). The typical twofold threshold is shown as dotted line and indicates nt positions highly susceptible to ILP cleavage (significant ILP reactivity).

Data obtained from ILP experiments indicate the presence of a highly flexible loop region between the second and third G-tract with strong cleavage of position U40 (U9 in AIR-3A), exceeding the threshold of 2.0, an indication for significant increase of in-line cleavage accessibility (Figure 20B and Figure 21B). This is in accordance with the hypothesized folding, predicting a loop region from position C39 to U42 (Figure 22). ILP reactivities for the other positions in the GQ area (G32 to G35 and G37 to G50) are > 0.6, except for A36, which yielded significantly less cleavage events (Figure 20B, Figure 21B and Figure 22).

RESULTS

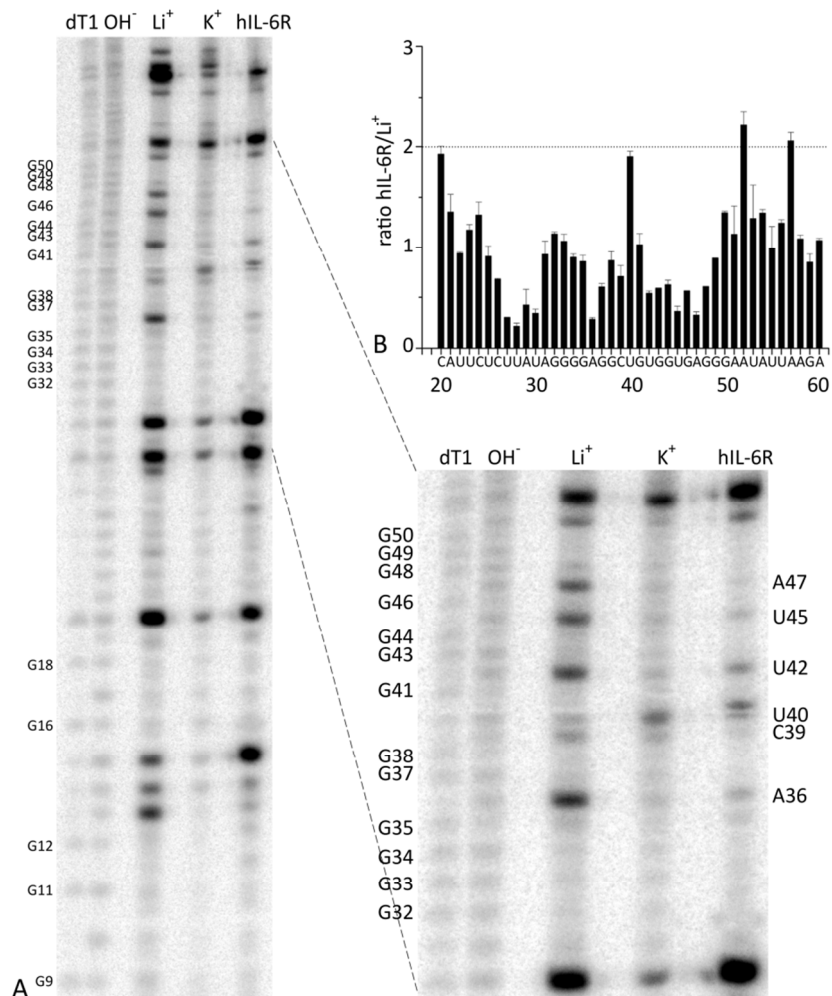


Figure 21: In-line probing (ILP) of AIR-3 indicates conformational change in presence of target hIL-6R. A) ILP on relevant regions of AIR-3 (5'-end labeled with ^{32}P , GQ motif formed by nt 32 to 50). Reference ladders dT1 (G-specific) and OH^- (alkaline hydrolysis, all positions) were used for band assignment. GQ identity is given by difference in cleavage patterns in presence of Li^+ and K^+ , respectively, with further differences by addition of hIL-6R. For this experiment, ILP conditions were the same as used in Figure 20, with additional 200 nM hIL-6R with 100 mM K^+ present in one sample (lane hIL-6R). The GQ region is highlighted as expanded region with Gs assigned on the left and nucleotides in between on the right. **B)** Analysis of ILP results representing ratios for each nt position in lane hIL-6R to lane Li^+ (data were normalized for total counts per lane, normalized band intensities in lane hIL-6R were divided by respective intensity in lane Li^+). The typical twofold threshold is shown as dotted line and indicates nt positions highly susceptible to ILP cleavage (significant ILP reactivity).

In presence of hIL-6R, however, lower accessibility of positions A36, G37, U42, G43, U45, G46 and A47 is represented by decreased reactivity. Therefore, it can be assumed that these nucleotides mediate interaction between RNA and protein, or at least gain additional rigidity to basic hydrolysis upon hIL-6R binding.

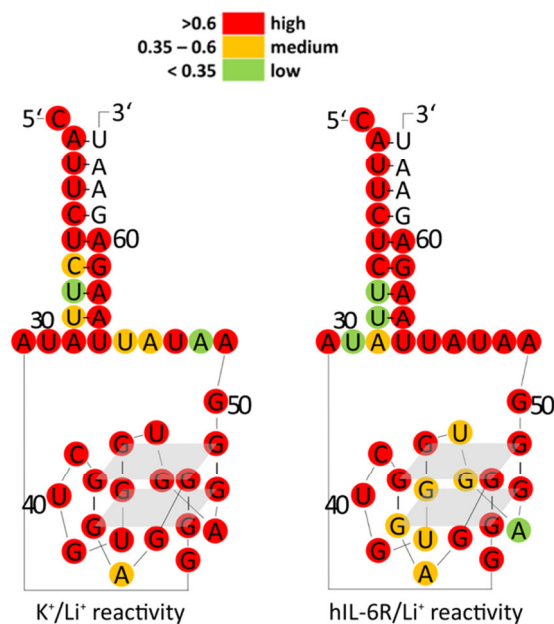


Figure 22: Schematic overview of ILP reactivity of AIR-3 GQ motif in presence of K^+ and hIL-6R. Representation of ILP ratios from Figure 20 and Figure 21, color coded for K^+/Li^+ (left) and hIL-6R/ Li^+ (right) for GQ region flanking areas with the assumption of a two tier GQ. Illustration shows hypothesized GQ within the secondary structure of AIR-3 according to Mfold¹⁹² prediction, forcing nt 32 - 50 to be single-stranded. Data were normalized for total counts per lane.

Also, in the regions preceding and following the GQ, a K^+ dependent protection is observed for positions C26 to U28, A52, A54 and U55. In presence of target protein, this is shifted to protection of U27 to U30 and increased cleavage of the region following the GQ (Figure 22). This may point at a conformational change of AIR-3 in presence of hIL-6R in an induced fit type manner.

5.2. Tolerance of AIR-3 and AIR-3A to nucleotide modifications in target binding

Recently, Kruspe *et al.* presented successful delivery of the prodrug 5-FdU mediated by AIR-3. Next to former studies dealing with stabilization by 2'-F-pyrimidines (2'-F-Py), this presented another possibility to postselectively modify hIL-6R specific aptamers with retained affinity.^{163, 209, 226} In order to further investigate the tolerance to nucleotide modifications, different aptamer variants containing the nucleoside analogs gemcitabine (2',2'-difluorodeoxycytidine) and 5-FdU (Figure 23; Table 24), were produced and tested towards their binding capacity to sIL-6R. Those which retained affinity for the sIL-6R were investigated with respect to their stability and therapeutic potential.

5.2.1. Intrinsic modification of AIR-3 with nucleoside analogs

The nucleoside analogs gemcitabine and 5-FdU were incorporated in AIR-3 templated RNA by *in vitro* T7 transcription (4.1.2) using the respective triphosphates and a variant of T7 RNA polymerase (Y639F) which tolerates a range of modified nucleotide triphosphates as substrates. RNAs were

5.2.1.1. Binding studies of gemcitabine modified AIR-3

Affinity of AIR-3 derivatives towards hIL-6R (*i.e.* soluble recombinant protein sIL-6R) was first assessed in Filter Retention Assays (FRA; 4.3.1), a classical approach to determine aptamer-protein interaction, and further studied in a cell based assay monitoring the capacity of a tested variant to compete with aptamer AIR-3A for binding to target cell line BaF3_hIL6R. For FRA, modified RNAs were 5'-end labeled with ^{32}P (4.1.6).

In Figure 24, results from FRA studies are compared, with Figure 24A showing representative filter scans. AIR-3 variants incorporating gemcitabine retained affinity for hIL-6R in a concentration dependent manner. Although affinity of AIR-3-Gem ($K_d = 103 \pm 10$ nM), AIR-3-Gem-2'FU ($K_d = 73 \pm 5$ nM), AIR-3-Gem-5FdU ($K_d = 167 \pm 2$ nM) was decreased compared to unmodified AIR-3A ($K_d = 55 \pm 5$ nM), it was still in nanomolar range.

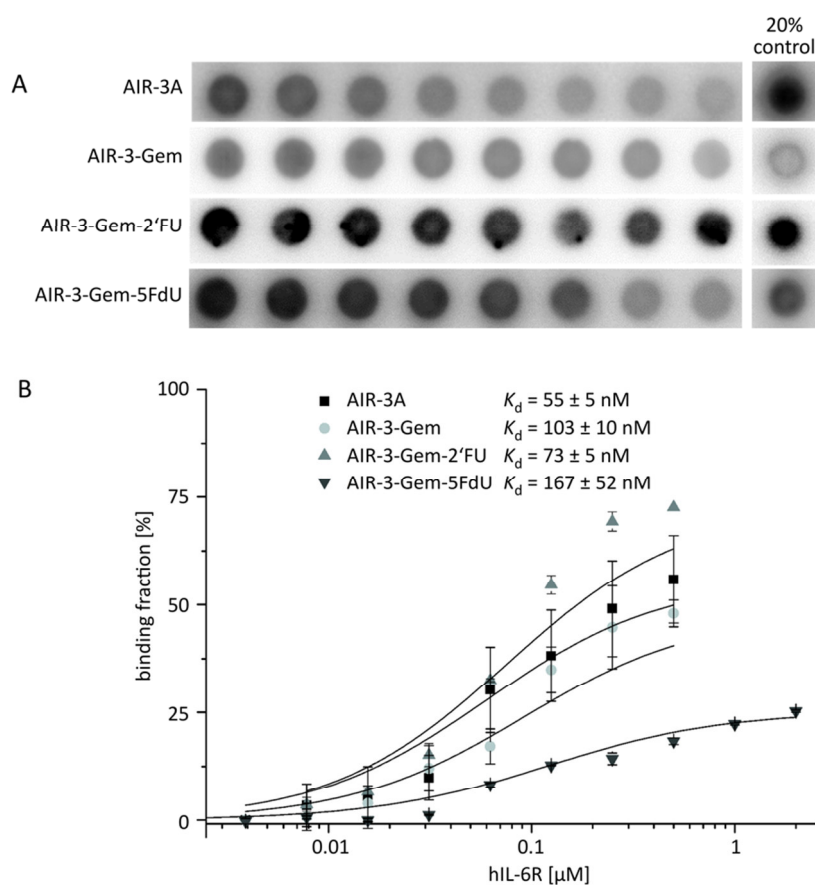


Figure 24: AIR-3 variants containing nucleoside analogs exhibit affinity to recombinant target protein. Binding was assayed by filter retention of RNA bound to hIL-6R. **A)** Representative filters from FRA studies. Constant amounts of ^{32}P 5'-end labeled RNA (< 1 nM) were incubated with increasing amounts of protein. Concentration dependent binding was detected as an increase in signal intensity (detected with imaging software) with increasing hIL-6R concentrations resulting in saturation curves. **B)** In relation to reference amounts (20%) of the respective labeled RNA, ratios were calculated and K_d values determined by application of Hill fit functions. Data points represent mean values of bound RNA, K_d values are given in the Figure (experiments performed in duplicates and triplicates).

Affinity for hIL-6R presented by target cells (BaF3_hIL-6R) was assayed by Flow Cytometry, monitoring the ability of the variants for displacement of fluorescently labeled AIR-3A. As shown in Figure 25, the same tendencies (increase in K_d compared to unmodified aptamer) were observed. As already known for AIR-3A, for AIR-3 variants a generally higher affinity to the native receptor than to recombinant protein was noticed (K_d values given in the Figure). Also, as negative control, the unselected SELEX library with gemcitabine modification (Gem-Pool-RNA) was tested to exclude unspecific binding of the nucleoside analog to hIL-6R. Here, no affinity was detected in either experiment.

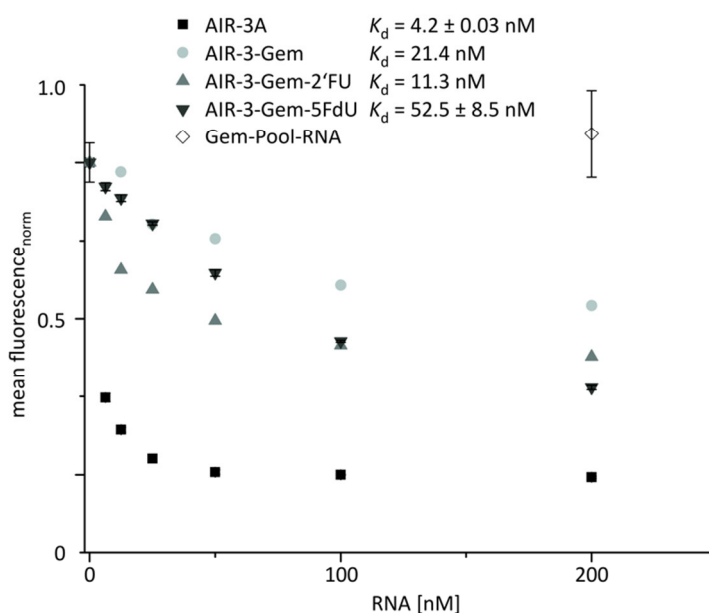


Figure 25: AIR-3 variants containing nucleoside analogs exhibit affinity to target cells. Cellular binding was analyzed by Flow Cytometry on BaF3_hIL-6R target cells. Cells were incubated with AIR-3 variants on ice for binding, washed and subsequently stained with Alexa Flour®647 labeled AIR-3A. Concentration dependent decrease of fluorescence was a measure for binding capacity.

In conclusion, all tested AIR-3 derivatives retained affinity under standard *in vitro* conditions and thereby proved to be suitable for further characterization.

5.2.1.2. Stability of gemcitabine modified AIR-3

In face of possible therapeutic applications of gemcitabine-modified AIR-3, stability is an important issue. Nucleases present in serum represent limitations to oligonucleotide-based therapeutics due to their degradative effect on DNA and RNA. Targeted delivery, in turn, requires the prodrug to reach its target intact in order to specifically deliver the drug at the site of action. Also, degradation sets free the drug beforehand, which increases off-target effects. For that reason, stabilized (chemically modified) oligonucleotides are commonly applied.¹³¹ Therefore, stability of AIR-3 derivatives was determined to assess if and for which time periods cell culture based assays could be performed.

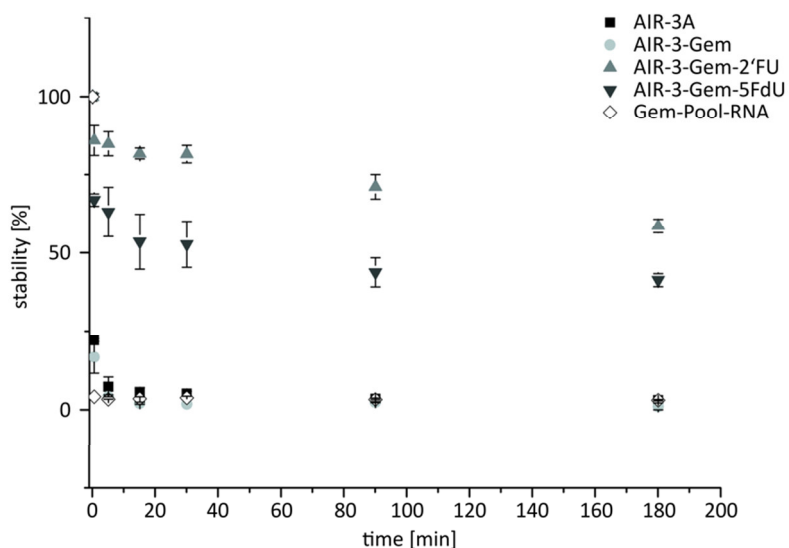


Figure 26: AIR-3 variants containing nucleoside analogs exhibit increased serum stability. Stability of ^{32}P 5'-end labeled AIR-3 variants (AIR-3A, AIR-3-Gem, AIR-3-Gem-2'FU, AIR-3-Gem-5FdU, Gem-Pool-RNA) in DMEM supplemented with 10% FBS at 37 °C. At indicated time points (given in minutes above each gel) aliquots were taken and immediately frozen in liquid N_2 . PAGE separation and analysis by autoradiography revealed remnant amounts of full length RNA. Intensities were normalized to total counts per lane and reference intensity at $t = 0$ min and plotted for comparison.

The stability of modified AIR-3 derivatives was increased from half-lives of several seconds (unmodified AIR-3A and AIR-3-Gem) to approximately 51 min for AIR-3-Gem-5FdU and 238 min for AIR-3-Gem-2'FU (Figure 26). Taken together, these data indicate that the variants AIR-3-Gem-5FdU and AIR-3-Gem-2'FU could be used for incubation in presence of serum, whereas the others would need further stabilization. Under standard cell culture conditions, degradation of these aptamer prodrugs and release of free drug in the media would occur so fast that toxic side effects would have to be expected. For that reason, all toxicity assays with AIR-3 derivatives were performed in serum free medium.

5.2.1.3. Cytotoxic properties of gemcitabine modified AIR-3

Next, potential therapeutic properties of the AIR-3 derivatives were analyzed. On the one hand, cytotoxicity to target cells bearing membrane bound hIL-6R (BaF3_hIL-6R) was assessed and compared to the effect on non-target cells (BaF3_gp130). On the other hand, cell cycle analyses were performed to link apparent effects to drug related actions.

Experiments were conducted on synchronized cell populations (T-block;²³¹ 4.5.9) as well as on non-synchronized cells. Synchronization did not change the effective experimental outcome (quantitative analysis) compared with non-synchronized cell data, but led to cellular changes in size and granularity resulting in discrepancies in Flow Cytometry analysis. Therefore, data presented in this work are taken from non-synchronized cells.

RESULTS

In a first approach, a dose response curve was generated by culturing target cells in presence of the free drug (*i.e.* gemcitabine triphosphate) to assess drug sensitivity. This experiment was conducted in full medium (DMEM, 10% FBS) monitoring the influence of native culture conditions. As gemcitabine triphosphate is no substrate to the nucleoside transporters phosphates needed to be removed enzymatically.²³⁴ The presence of serum phosphatases (in serum supplemented DMEM) was a prerequisite to ensure cellular uptake of gemcitabine and evaluate its toxicity towards BaF3_hIL-6R cells in this assay.

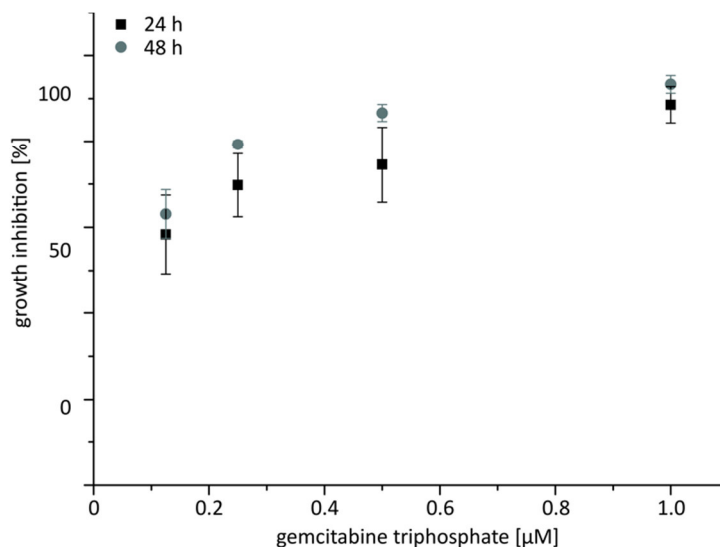


Figure 27: Dose response of BaF3_hIL-6R towards gemcitabine triphosphate. Cells were cultured in full medium at 37 °C and 5% CO₂ in presence of indicated concentrations of gemcitabine triphosphate for 24 and 48 h respectively. Viability was then measured in a colorimetric resazurin based assay and growth inhibition calculated in relation to untreated reference cells. Plotted data represent means of four independent experiments.

From Figure 27, it can be seen that concentrations of 0.5 to 1 μM gemcitabine triphosphate resulted in growth inhibition of 75 to 92%. As modified AIR-3 contains 15 units of gemcitabine, the molar equivalent would need RNA concentrations of at least 33 nM. Considering also the affinity of the variants towards target cells, concentrations exceeding the K_d were needed. For that reason, and with respect to experimental data on AIR-3 mediated 5-FdU delivery,¹⁶³ derivatives were applied at concentrations of 250 nM.

RESULTS

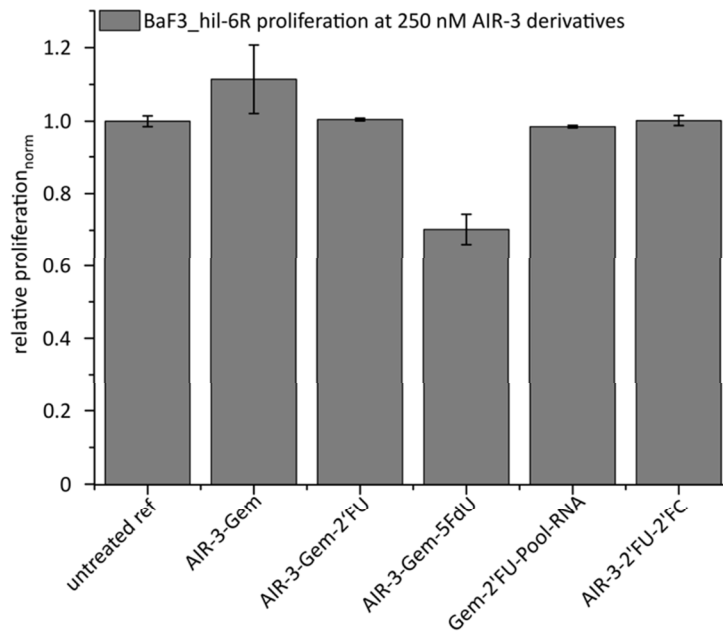


Figure 28: Analysis of cytotoxic effects of gemcitabine derivatized AIR-3 on BaF3_hil-6R target cells. Proliferation of cells incubated with 250 nM of respective RNA for 3 h at 37 °C and 5% CO₂ in serum free DMEM. Cells were then washed and cultured in serum-supplemented DMEM for 24 h. Relative proliferation was assessed in a colorimetric (resazurin) and a luminescence based assay. Compared to untreated reference cells, treatment with derivatives AIR-3-Gem, AIR-3-Gem-2'FU, Gem-2'FU-Pool-RNA or AIR-3-2'FU-2'FC had no or slight pro-proliferative effect. In cells treated with AIR-3-Gem-5FdU proliferation decayed by 29.8% which indicated specific cytotoxicity. Plotted data represent means of triplicates of at least two independent experiments.

Cytotoxicity studies of produced AIR-3 variants revealed no specific toxicity of AIR-3 derivatives containing only gemcitabine as a drug (Figure 28). Also, for 2'F-modified mock control (AIR-3-2'FC-2'FU) and gemcitabine modified unspecific binding control (Gem-2'FU-Pool-RNA) no influence on proliferation was observed. AIR-3-Gem rather exhibited a slight pro-proliferative effect. Only variant AIR-3-Gem-5FdU caused a proliferation decay of $29.8 \pm 4.1\%$ compared to untreated reference cells. Now, this AIR-3 derivative was further examined by comparing its effect on target and non-target cells.

Figure 29 shows that AIR-3-Gem-5FdU displays target specific cytotoxicity. Compared to BaF3_gp130 cells treated with 250 nM AIR-3-Gem-5FdU, proliferation of target cells undergoing the same treatment was decreased by $58.1 \pm 0.6\%$. As none of the tested gemcitabine AIR-3 variants without 5-FdU displayed cytotoxic effects, the possibility of 5-FdU causing proliferation decreases was taken into account.

RESULTS

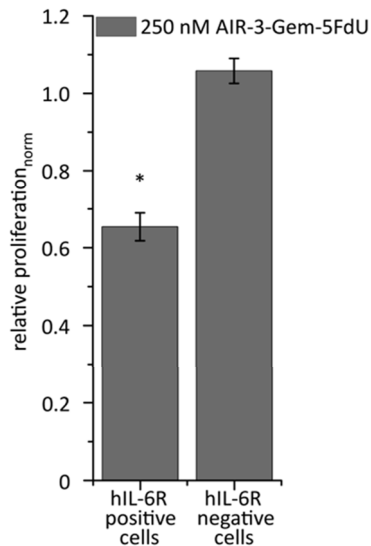


Figure 29: Specific cytotoxic effect of AIR-3-Gem-5FdU on target cells. Proliferation of BaF3_hIL-6R cells in comparison to non-target cells BaF3_gp130. Cells were incubated with AIR-3-Gem-5FdU (250 nM) for 3 h at 37 °C and 5% CO₂ in serum free DMEM, washed and cultured in serum-supplemented DMEM for 24 h. Relative proliferation was assessed in colorimetric (resazurin) and a luminescence based assay. Plotted data represent means of triplicates of at least two independent experiments. Asterisk (*) marks statistically significant proliferation differences ($p \leq 0.05$).

Although anti-proliferative effects of gemcitabine-equipped AIR-3 were not observed, additional cell cycle analyses (4.5.12) were carried out to detect possible effects not apparent otherwise. Gemcitabine is known to have different effects on cell cycle distribution depending on dose and time.²³⁵ Under the conditions tested herein, S-phase arrest would be expected, similar as shown for 5FdU delivery. Figure 30 illustrates results obtained from cell cycle analyses of target cells treated with AIR-3 derivatives.

RESULTS

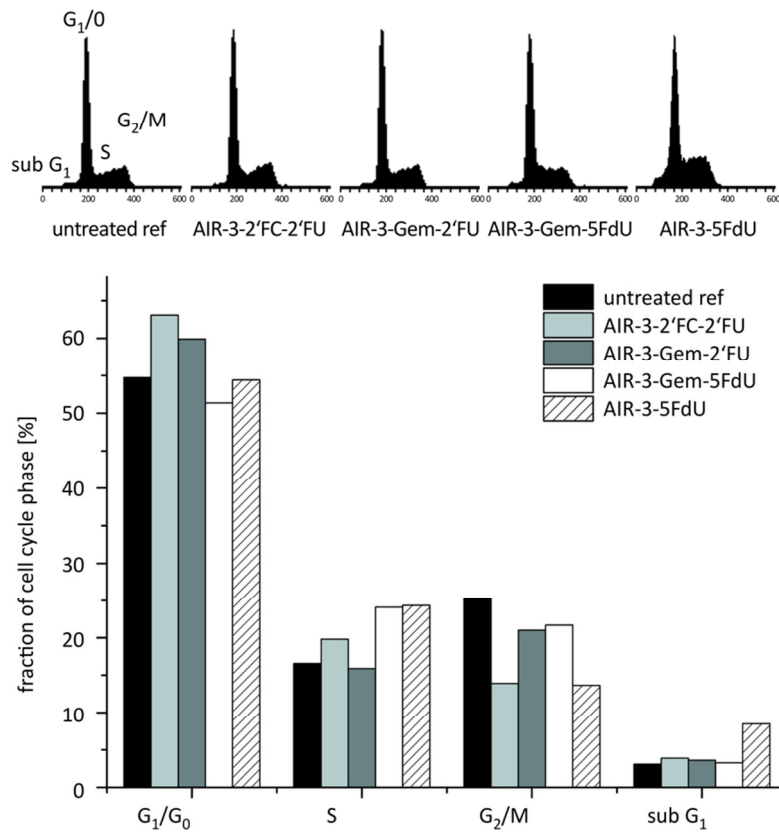


Figure 30: Cell cycle analyses of BaF3_hIL-6R cells treated with AIR-3 derivatives. Representative histograms depicting cell cycle distribution in BaF3_hIL-6R cells treated with gemcitabine- and 5Fdu-derivatized AIR-3 and plot of measured fractions. Cells were incubated with respective RNAs (250 nM) in serum free DMEM for 3 h at 37 °C and 5% CO₂, washed to remove RNA and cultured for further 4 h in serum-supplemented DMEM. For Flow Cytometry analysis, cells were fixed, permeabilized and stained with propidium iodide (PI; 4.5.12).

Negative control 2'FC-2'FU-AIR-3 showed a slight increase in G₁ and S-phase and a decrease in G₂/M phase indicating a proliferative effect. For variant AIR-3-Gem-2'FU in comparison to untreated reference cells, G₂/M phase fraction and G₁/G₀ fraction were slightly increased, while variants including 5Fdu both showed increase in S-phase fractions towards all other samples, with AIR-3-5Fdu being the only derivative causing increased sub-G₁ fraction.

In summary, gemcitabine modification of AIR-3 itself did not result in cytotoxic effects. Therefore, further characterization was performed on double variant AIR-3-Gem-5Fdu only.

AIR-3 mediated delivery was already realized for 5-Fdu, yielding a comparable proliferation decrease of $24,8 \pm 4,2\%$.¹⁶³ Therefore, a comparison of 5-Fdu modified AIR-3 and AIR-3-Gem-5Fdu was carried out to evaluate cytotoxic efficacy of both variants. Published data¹⁶³ were reproducible. To assess additive effects of gemcitabine, culturing time after drug exposition was prolonged to 72 h.

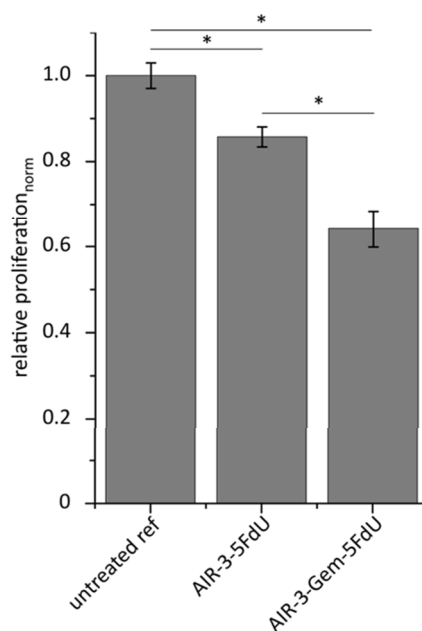


Figure 31: Effects of 5FdU-containing AIR-3 derivatives on target cell proliferation. Proliferation of cells incubated with 250 nM of AIR-3-Gem-5FdU or of AIR-3-5FdU for 3 h at 37 °C and 5% CO₂ in serum free DMEM. Cells were then washed and cultured in serum-supplemented DMEM for 72 h. Relative proliferation was assessed in a colorimetric (resazurin) assay. Plotted data represent means of duplicates. Asterisk (*) marks statistically significant proliferation differences referred to reference indicated by bars ($p \leq 0.05$).

As seen in Figure 31, AIR-3-Gem-5FdU indeed displays increased anti-proliferative effects after a longer time period. For AIR-3-5FdU, proliferation was decreased by $14.3 \pm 2.3\%$ compared to untreated reference cells, as for AIR-3-Gem-5FdU, decrease was in the range of $35.9 \pm 4.3\%$ after three days. This phenomenon is considered further in the discussion section.

5.2.2. AIR-3 variants containing deoxy pyrimidines

Because DNA is less susceptible towards nuclease degradation than RNA, another means of stabilization is the derivatization of nucleotides by their deoxy-analogs. For AIR-3 and AIR-3A, deoxy pyrimidines (dU and dC) were introduced during *in vitro* transcription. Purified products were radio labeled and analyzed by FRA as described above. Figure 32 illustrates the results obtained.

RESULTS

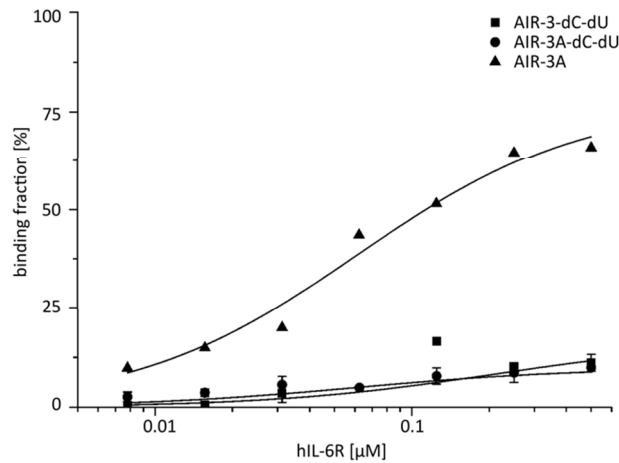


Figure 32: Binding analysis of deoxy derivatives of AIR-3 and AIR-3A. Binding was assayed by filter retention of RNA bound to hIL-6R. Constant amounts of ^{32}P 5'-end labeled RNA (< 1 nM) were incubated with increasing amounts of protein. Data points represent mean values of bound RNA, as a reference unmodified AIR-3A (triangles) was assayed (experiments performed in duplicates (single experiment for AIR-3A) and conducted by Dr. Sven Kruspe).

As seen from the plotted data, no concentration dependent binding could be detected for the tested deoxy derivatives. Compared to native AIR-3A, the variants showed no binding to hIL-6R.

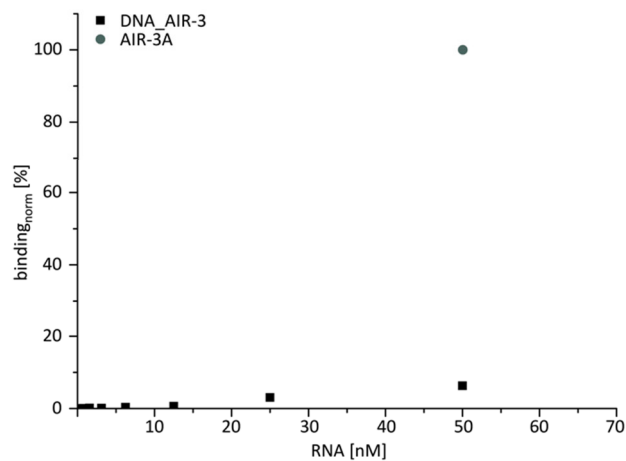


Figure 33: Cellular binding of DNA_AIR-3 to target cells. Fluorescently labeled (Alexa Flour[®]647) DNA_AIR-3 was incubated with BaF-3_hIL-6R cells on ice for binding, washed and analyzed by Flow Cytometry. As a control, AIR-3A (same fluorescent label) was applied on target cells at 50 nM. Data were normalized to this reference.

Also, when an all-DNA analog of AIR-3 (fluorescently labeled with Alexa Flour[®]647) was analyzed for binding to target cells (BaF3_hIL-6R), a total loss of affinity was observed (Figure 33). These results indicate that deoxy-modifications of AIR-3 and AIR-3A are not suitable for stabilization of this aptamer. Possibly they cause structural remodeling of the molecule hampering interaction with hIL-6R.

5.3. Target specificity

AIR-3A is binding specifically to hIL-6R, the target it was selected for. Yet, GQ forming oligonucleotides were shown to display binding to other targets especially to classes of proteins known as GQ-binding proteins. In face of possible therapeutic applications, also binding towards thrombin, a protein for which two different GQ-forming DNA aptamers (TBA and HD22)^{227, 236} were selected. Also different cell lines were tested for affinity to AIR-3A.

5.3.1. Analysis of AIR-3A non-target affinity

First, binding of radio labeled AIR-3A towards thrombin was analyzed by FRA. As shown in Figure 34, AIR-3A does also bind to thrombin. In turn, TBA did not show affinity to hIL-6R (data not shown).

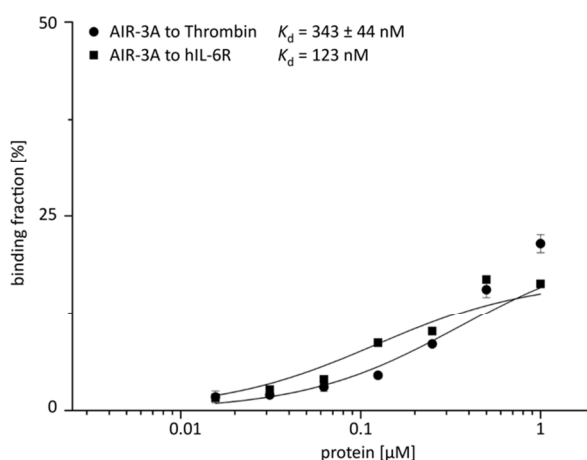


Figure 34: Binding of AIR-3A to thrombin. Binding was assayed by Filter Retention of RNA bound to thrombin. Constant amounts of ³²P 5'-end labeled AIR-3A (< 1 nM) were incubated with increasing amounts of protein. Data points represent mean values of bound RNA, as a reference hIL-6R was used (experiments performed in duplicates (single experiment for hIL-6R)).

As this proof of principle study turned out positive, also different cell lines were tested for affinity of AIR-3A. Target cell lines (PC3, KMS 12 BM, RPMI 8226, LNCaP, U266, HeLa and HEK 293) bearing membrane bound hIL-6R in different amounts were tested, with respect to possible applications in delivery approaches.

RESULTS

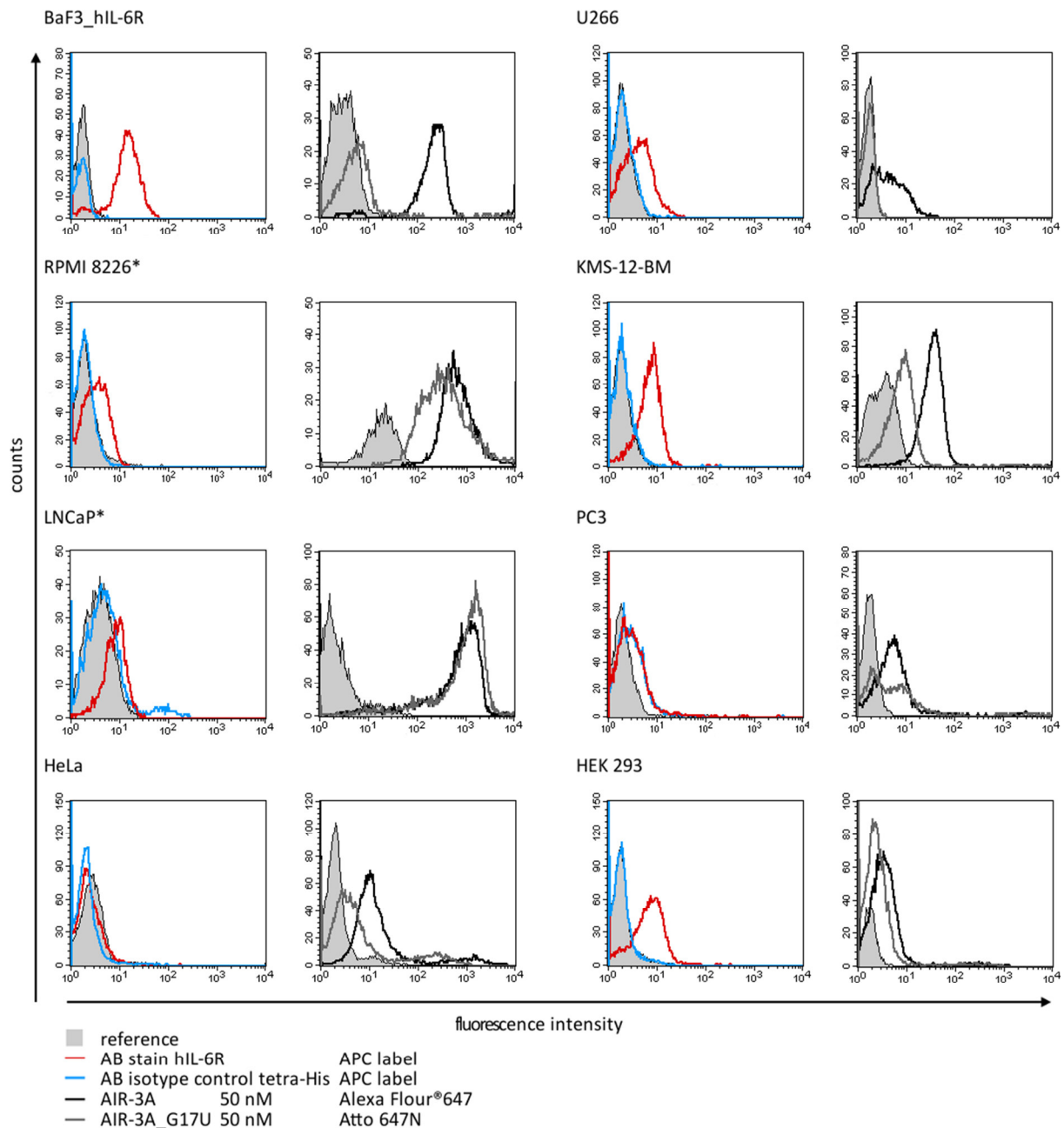


Figure 35: Cellular binding of AIR-3A to target cells. Flow Cytometry analysis of hIL-6R presentation and AIR-3A binding by different cell lines. Histogram plots for representative measurements conducted on each cell line. Immunostaining of cellular presented hIL-6R was conducted using anti-hIL-6R primary antibody (murine) and anti-mouse-IgG₁-APC secondary antibody. Shifts in fluorescence intensity (red curve) indicated hIL-6R presence. As an isotype control, anti-tetra-His mouse IgG₁ was used for the first and anti-mouse-IgG₁-APC for the second stain (blue curve). For detection of aptamer binding, cells were incubated with fluorescently labeled AIR-3A (black curve) or AIR-3A_G17U (dark gray curve) in PBS at 50 nM, washed and analyzed by Flow Cytometry. Binding was observed for all cell lines to different extent and correlation to hIL-6R presence. For each measurement 10000 cells were counted and gated for viable populations. For indicated cell lines (*) data for AIR-3A and AIR-3A_G17U binding were collected by Dr. Sven Kruspe.¹⁹⁷

Figure 35 shows AIR-3A binding to different hIL-6R-positive cell lines. Even though non-target cell lines such as BaF3_gp130 do not have affinity for AIR-3A, it has to be assumed that other proteins and membrane associated molecules than hIL-6R represent targets for AIR-3A.

5.3.2. AIR-3A-aided protein isolation from cell extracts

To further validate the assumption that AIR-3A binds other proteins next to hIL-6R, protein pull-down experiments from protein extracts of three different cell lysates were performed (4.3.3). The lysates emerged from sonification and the dialyzed protein extracts contained different kinds of cellular proteins recovered.

Similar approaches were used by Shangguan *et al.* and Hacht *et al.* to identify cellular proteins interacting with DNA aptamers and GQ forming RNA, respectively.^{107, 228}

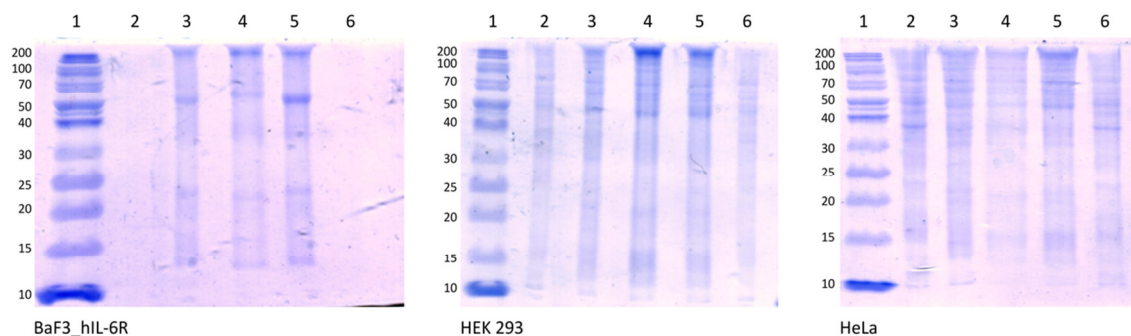


Figure 36: AIR-3A mediated pull-down of cellular proteins from cell extracts. Coomassie stained SDS-PAGE (15%) used to analyze proteins from cellular extracts recognized by AIR-3A. Indicated cell lines were harvested, lysed and dialyzed as described in 4.3.3. Streptavidin coated magnetic beads were used to immobilize biotinylated RNAs (AIR-3A and AIR-3A_G17U). Protein extracts were successively incubated with magnetic beads only, immobilized AIR-3A_G17U (200 pmol) or immobilized AIR-3A (200 pmol) in the presence of 200 pmol tRNA as a competitor. Beads were collected by magnetic separation, washed four times with 1 mL 1x PBS containing 3 mM MgCl₂ and proteins were eluted by heating to 90 °C in 30 µL of loading buffer for 20 min. Samples were analyzed by SDS-PAGE. Lane 1: PageRuler™ Unstained Protein Ladder, 2: protein extract prior to pull-down, 3: proteins captured with magnetic beads only, 4: proteins captured with nonbinding RNA AIR-3A_G17U, 5: proteins captured with aptamer AIR-3A, 6: supernatant of protein extract after pull-down.

In Figure 36, results from AIR-3A mediated pull-down experiments are displayed. From three different cell lines (target cell line BaF-3_hIL-6R, non-target cell lines HEK 293 and HeLa) protein extracts were used and incubated successively with differently functionalized magnetic beads (see caption). Bands not occurring in controls (lanes 3 and 4) represent proteins specifically recognized by AIR-3A while bands appearing in both the GQ forming AIR-3A and the control AIR-3A_G17U are likely unspecific RNA binders. From BaF3_hIL-6R protein extract only a few bands were visible in the gel, pull-down samples from HEK 293 and HeLa extracts comprised a large number of proteins. From identical bands occurring in control lanes (pull-down with streptavidin coated beads only and with non-specifically binding RNA), captured proteins were concluded to be mainly unspecifically bound. Yet, at closer investigation, some bands present in the AIR-3A-aided pull-down from BaF3_hIL-6R and HeLa extracts, but not in the respective controls, were observed (Figure 37). In the pull-down from HEK 293 extract, no decisive differences were found in the band patterns.

RESULTS

For analysis by LC-MS, three bands from AIR-3A-aided pull-down (one from BaF3_hIL-6R and two from HeLa extract analysis, numbers ②, ④ and ⑥ in Figure 37) and the three respective bands from the control experiment with non-binding RNA AIR-3A_G17U (①, ③ and ⑤) were excised from the Coomassie-stained gels and delivered to the *Core Facility Mass Spectrometric Proteomics of the UKE* (N27, Martinstraße 52, 20246 Hamburg).

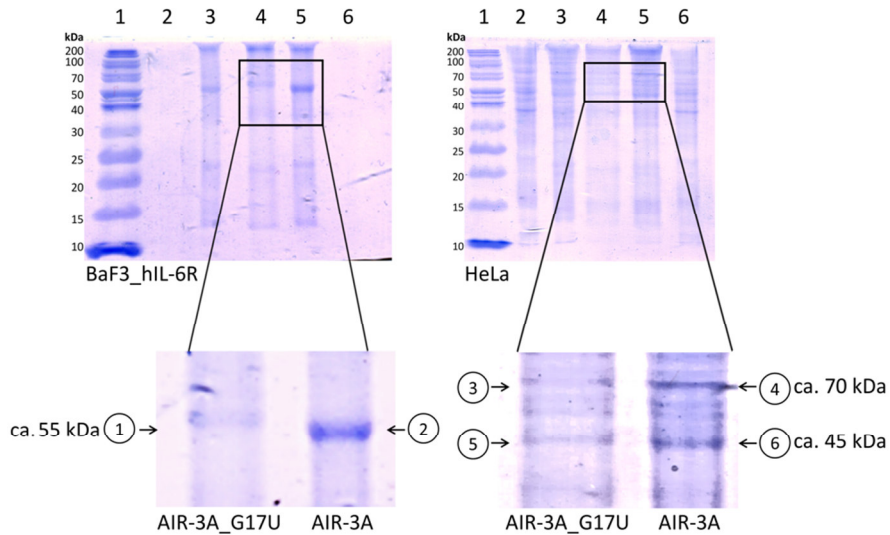


Figure 37: Bands excised from SDS gels for LC-MS analysis after AIR-3A mediated pull-down. The marked bands from BaF3_hIL-6R (①+②) and HeLa (③-⑥) pull-downs showed differences in migration and intensity between the band patterns of proteins captured with AIR-3A (②, ④, ⑥) and non-binding AIR-3A_G17U (①, ③, ⑤) and were analyzed by LC-MS at the *Core Facility Mass Spectrometric Proteomics of the UKE* (for results see Table 25; lane assignment as in Figure 36). Analysis conducted by Sönke Harder and Marcel Kwiatkowski from the group of Prof. Dr. Hartmut Schlüter.

Analyzed proteins from the HeLa pull-down were matched with human protein data sets by the core facility. In the case of BaF3_hIL-6R samples, murine proteins as well as human proteins were matched, as this murine cell line was stably transfected to present human proteins hIL-6R and gp130. Thus, both data sets were screened for proteins uniquely present in the AIR-3A pull-downs. The results are listed in Table 25.

Table 25: Selection of cellular proteins captured by pull-down assays.

Proteins specifically captured with AIR-3A (<i>murine, human</i>)	UniProt Accession code	MW [kDa]	Band	Unique peptides
<i>ATP synthase subunit alpha, mitochondrial</i>	Q03265	56,27	②	11
Cleavage and polyadenylation specificity factor subunit 6 ^[*]	Q16630	59,17	④	5
Heterogeneous nuclear ribonucleoprotein R ^[*]	O43390	70,90	④	4
Trifunctional enzyme subunit beta ^[*]	P55084	51,262	⑥	4
Desmoplakin ^[†]	P15924	331,57	④	9
Junction plakoglobin ^[†]	P14923	81,69	④	6
Keratin, type I cytoskeletal 14 ^[†]	P02533	51,53	④	5
Keratin, type I cytoskeletal 16 ^[†]	P08779	51,24	④	14
Keratin, type II cytoskeletal 6A ^[†]	P02538	60,01	④	4
Keratin, type II cytoskeletal 6C ^[†]	P48668	59,99	④	4
Other unspecifically recovered proteins, formerly shown to bind GQs				
Nuclease-sensitive element-binding protein 1	P67809	35,90	③, ④	6
			⑤, ⑥	4
Nucleolin	P19338	76,57	③, ④	15
			⑤, ⑥	6
Ras GTPase-activating protein-binding protein 1	Q13283	52,13	③, ④	9

*RNA binding proteins, †cytoskeleton associated proteins

From the proteins listed in Table 25, no reliable information on AIR-3A affinity could be derived. The major drawback was represented by the fact that no hIL-6R was detected in the BaF-3_hIL-6R samples. The gel showed one distinct band at approximately 55 kDa in the AIR-3A pull-down (②), which was assumed to contain hIL-6R. Yet, it comprised only one unique match for AIR-3A. This was murine mitochondrial ATP synthase subunit alpha. For this protein, no preferential GQ binding is known. It rather displays general affinity towards mRNA.²³⁷ The other proteins detected in this band were the same as in the control pull-down (①) and are listed in Table 31. Cytoskeletal proteins such as actin and tubulin, which are generally of high abundance, occurred and also keratin, which may also represent a contamination from hair or skin acquired during sample preparation. Next to murine ATP synthase subunit alpha, some human proteins were preferentially isolated from HeLa extract

using AIR-3A. They were either known for general RNA binding ([*] in Table 25) or highly abundant cytoskeletal proteins ([†] in Table 25) that are easily co-precipitated in pull-down assays.^{107, 228} Identified proteins that were formerly shown to bind GQs are Nucleolin and Ras GTPase-activating protein-binding protein 1 and splicing factor Nuclease-sensitive element-binding protein 1 which bind RNA in general.¹⁰⁷

In summary, the results obtained in the attempt to characterize the target specificity of AIR-3A, reflect the general possibility of this G-quadruplex to bind other proteins and cells with very low expression levels of hIL-6R in a concentration dependent manner. Even though this binding may occur by unspecific interactions, as can be suggested from the outcome of pull-down assays compared with non-GQ forming RNA, it is probable that AIR-3A targets other proteins next to hIL-6R that have affinity for GQs. Yet, no popular candidates were identified as specific targets of AIR-3A. But as the functions and properties of GQ binding proteins are not yet fully understood but remain subject of research, the impact of proteins identified by AIR-3A mediated pull-down might gain importance in the future. A list of all proteins identified during LC-MS analysis that were either specifically recognized by AIR-3A or by both, AIR-3A and AIR-3A_G17U, is attached in section 10.5.

5.4. Influence of AIR-3A presence on endocytic behavior

It has been shown that AIR-3A binds to hIL-6R presented on cell membranes and is internalized in endocytic processes with the receptor.²³² Also, lysosomal fate of the endocytosed aptamer has been suggested.¹⁶³ In an attempt to better understand cellular uptake and possible influence of AIR-3A on endocytosis, co-localization of aptamer fluorescence and different stains (hIL-6R detection, murine transferrin (mTrf) and lysosomes (LysoTracker® Green)) were investigated by confocal Laser Scanning Microscopy (cLSM; 4.5.4). Also, quantification of receptor internalization (fluorescent immunodetection) in presence of AIR-3A was realized by Flow Cytometry (4.5.3).

All measurements were performed in 1x PBS. Cells were washed thoroughly to remove remnant serum proteins and prevent unspecific cellular uptake or RNase activity.

5.4.1. Subcellular localization of endocytosed hIL-6R and AIR-3A

To assess whether lysosomal localization holds also true for target protein hIL-6R, immunostaining (APC-labeled secondary antibody [AB]) of cellular hIL-6R was detected simultaneously with staining of lysosomes with LysoTracker®, a dye exhibiting fluorescence at low pH only (Figure 38).

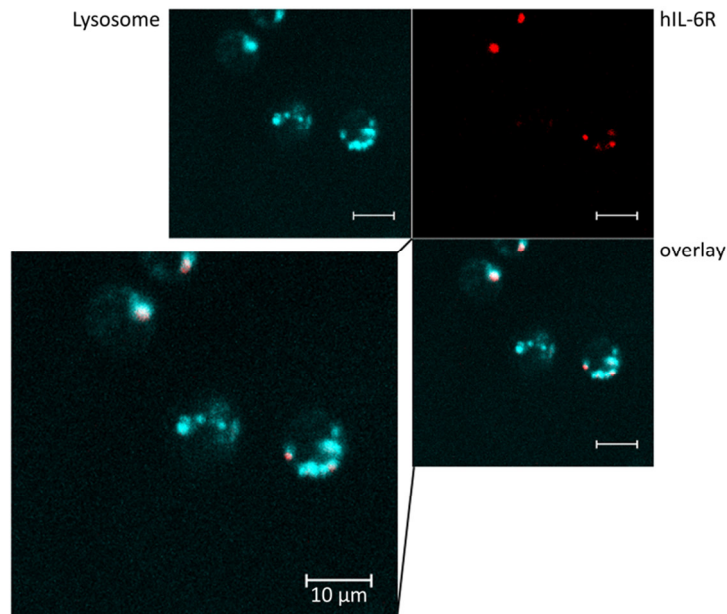


Figure 38: Co-localization of hIL-6R and lysosomes after endocytosis visualized by cLSM. BaF3_hIL-6R cells were incubated with LysoTracker® Green (10 nM) and anti-hIL-6R primary AB on ice for 30 min followed by washing and subsequent 30 min incubation with secondary APC-conjugated AB. After washing and further incubation for 10 min at 37 °C, subcellular localization was analyzed using cLSM. Single stains were conducted beforehand to adjust settings threshold and to avoid crosstalk signals between the two fluorescence channels. Fluorescence corresponding to hIL-6R (red) was detected by excitation at $\lambda_{ex} = 633$ nm, LT fluorescence by excitation at $\lambda_{ex} = 488$ nm. Panel displays LT fluorescence (UL, green), hIL-6R fluorescence (UR, red) and overlay of both fluorescence channels (LR and zoomed in as inset LL): LP 475 nm, LP 650 nm. Scale bars 10 μ m.

Both lysosomes and hIL-6R fluorescence were visible as compartmentalized vesicles. After endocytosis, hIL-6R shows co-localization with the lysosome as indicated by overlaying fluorescent foci. This means that a portion of hIL-6R undergoes lysosomal degradation independently of AIR-3A presence, which is in accordance with the literature.²³⁸

Another aspect investigated was the endocytic pathway taken by hIL-6R. Though little is known about the detailed mechanism, studies testing several inhibitors for endocytosis suggested that different pathways were used for hIL-6R uptake.¹⁹⁷ Therefore, it was investigated whether endocytosis in a clathrin-dependent manner could be detected. That for, as a standard control, clathrin-dependent endocytosis of transferrin receptor (TfR) was visualized by fluorescently labeled mTrf, and co-staining of hIL-6R was detected by cLSM.

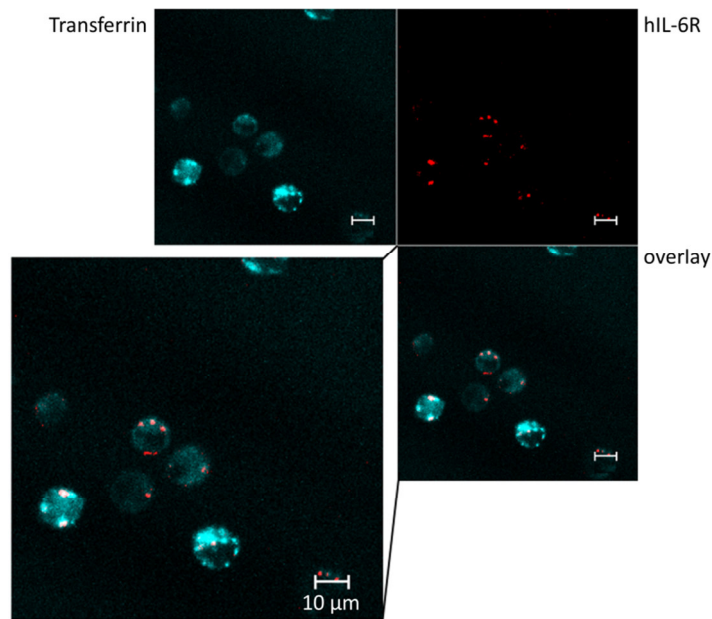


Figure 39: Co-localization of hIL-6R and mTransferrin after endocytosis visualized by cLSM. BaF3_hIL-6R cells were incubated with Alexa Flour®488 labeled mTrf (10 µg/mL) and anti-hIL-6R primary AB on ice for 30 min followed by washing and subsequent 30 min incubation with APC-conjugated secondary AB. After washing and further incubation for 10 min at 37 °C subcellular localization was analyzed using cLSM. Single stains were conducted beforehand to adjust settings threshold as to avoid crosstalk signals between the two fluorescence channels. Fluorescence corresponding to hIL-6R (red) was detected by excitation at $\lambda_{ex} = 633$ nm, mTrf fluorescence by excitation at $\lambda_{ex} = 488$ nm. Panel displays mTrf fluorescence (UL, green), hIL-6R fluorescence (UR, red) and overlay of both fluorescence channels (LR and zoomed in as inset LL): LP 475 nm, LP 650 nm. Scale bars 10 µm.

Concomitant detection of endocytosis revealed partial co-localization of TfR (green) and hIL-6R (red). Some of the respective foci overlaid as illustrated in Figure 39. Yet, a portion of red fluorescence corresponding to internalized hIL-6R was internalized independently from TfR. The assumption of hIL-6R undertaking different endocytic ways was thereby confirmed.

Next, endocytic behavior of AIR-3A in presence of the tested co-localization compounds was examined. In a similar approach, the target cell line BaF3_hIL-6R was incubated simultaneously with Alexa Flour®647 labeled AIR-3A and anti-hIL-6R primary antibody (detected with FITC-conjugated secondary AB), Alexa Flour®488 labeled mTrf or LT.

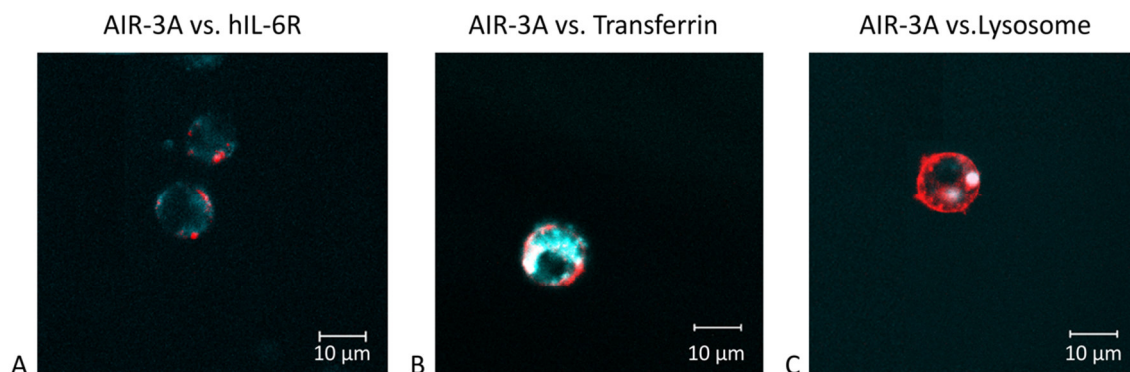


Figure 40: Co-localization of AIR-3A and hIL-6R, mTrf or LT after endocytosis visualized by cLSM. Endocytic fate of AIR-3A was analyzed on BaF3_hIL-6R cells. Cells were incubated with **A)** anti-hIL-6R primary antibody and FITC-labeled secondary AB as subsequent stain on ice for 30 min each. Then Alexa Flour®647 labeled AIR-3A (50 nM) was added for 10 min at 37 °C. **B)** Alexa Flour®488 labeled mTrf (10 µg/mL) or **C)** LysoTracker® Green (10 nM) were incubated with Alexa Flour®647 labeled AIR-3A (50 nM) simultaneously for 10 min at 37 °C. Subcellular localization was analyzed using cLSM. Single stains were conducted beforehand to adjust settings threshold as to avoid crosstalk signals between the two fluorescence channels. Fluorescence corresponding to AIR-3A (red) was detected by excitation at $\lambda_{ex} = 633$ nm, mTrf- hIL-6R- and LT fluorescence were detected by excitation at $\lambda_{ex} = 488$ nm (green). Figures represent overlays of both fluorescence channels: LP 475 nm, LP 650 nm. Scale bars 10 µm.

As presented in Figure 40A, aptamer fluorescence is partially co-localized with subcellular hIL-6R signals. Subcellular distribution of hIL-6R is broader compared to vesicular AIR-3A. Thus, some receptor molecules stained with antibody remained free of on-bound AIR-3A. According to Figure 40B, AIR-3A showed partial co-localization with mTrf as well. This indicated that clathrin-dependent endocytosis is a possible route for AIR-3A to enter the cell. As this co-localization was not exclusive but some foci were spotted independently, AIR-3A is not limited to this pathway either. After endocytosis, lysosomal localization of AIR-3A could be confirmed (Figure 40C). The compartmentalized appearance coincided with hIL-6R fluorescence detected after uptake (Figure 38). This suggested disposition of the fluorescence species in the endocytic vesicle and prevention of endosomal escape.

5.4.2. Analysis of AIR-3A influence on hIL-6R presentation and endocytosis over time

In a further approach to identify influences on hIL-6R endocytosis, fluorescence from immunostained hIL-6R in dependence of different effectors was investigated in a time-course experiment. For hIL-6 stimulation, reduction of hIL-6R present on the cell-surface was shown until recycling processes returned the receptor to the membrane.²³⁸ Cells were stained for hIL-6R detection with antibodies on ice and allowed to undergo endocytosis under culturing conditions for different time intervals. Immediately after incubation, cells were washed and analyzed for antibody fluorescence by Flow Cytometry. Effectors tested were the actual ligand hIL-6, aptamer AIR-3A and non-binding variant

AIR-3A_G17U (representing unspecific RNA interaction). Also, additional influence of pre-incubation with AIR-3A prior to immunostaining was analyzed.

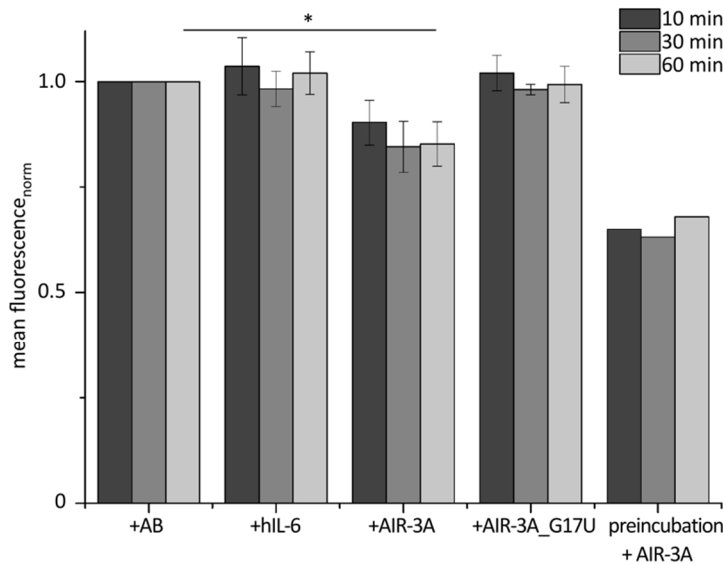


Figure 41: Cellular uptake of hIL-6R in dependence of presence of different effectors. Uptake was monitored by Flow Cytometry detection of hIL-6R immunofluorescence on BaF3_hIL-6R cells. Cells were harvested, washed and kept on ice for immunostaining (anti-hIL-6R primary AB, APC-labeled secondary AB). Effectors were added to cell suspensions in 1x PBS: hIL-6 (10 ng/mL), AIR-3A or AIR-3A_G17U (100 nM each). One experiment included extra incubation with AIR-3A (100 nM) prior to AB staining and further aptamer presence during time-course study. Samples were taken after 10, 30 and 60 min, washed and analyzed counting at least 10000 cells per sample. Cellular auto fluorescence was taken from untreated cells and subtracted from all samples. Measured mean fluorescence was then normalized to AB fluorescence without further effector treatment at respective time points. Plotted data represent means from three independent experiments except for pre-incubation with AIR-3A, which was taken from a single experiment. Asterisk (*) marks statistically significant proliferation differences referred to reference indicated by bar ($p \leq 0.05$).

As represented in Figure 41, AIR-3A incubation induced fluorescence reduction compared to sole AB treatment at different time points. Presence of ligand hIL-6 or non-binding RNA AIR-3A_G17U did not result in a statistically significant change of fluorescence intensities. Only AIR-3A clearly reduced signal intensities by 10% after 10 min incubation to 15% after 30 and 60 min. As an exemplary reference, influence of additional 10 min pre-incubation with AIR-3A was plotted, resulting in fluorescence reduction by 32 to 37%. This decrease in immunofluorescence argues for reduced uptake of hIL-6R or indicates increased lysosomal localization in dependence of AIR-3A, which is discussed in the following section.

6. Discussion

Aptamers are short monomolecular oligonucleotides (20-70 nt) that display affinity towards a certain target molecule which they specifically recognize. This specific binding property results from intramolecular folding that makes each aptamer unique in its 3D-structure. Different classes of molecules can serve as targets for aptamer selection ranging from small ions to macromolecules like proteins. Application of aptamers is often directed towards therapeutics or diagnostics. They can either display inhibitory properties or their recognition potential is used for directed delivery of effectors (e.g. markers, drugs) to the target. In that respect the structure-function relationship of aptamers is of interest. Hydrogen bonds, electrostatic interactions, π -effects, cationic contributions and van der Waals forces can influence the interaction with the target.

Oligonucleotides can adopt different structures of which the helical duplex (as found in DNA) is the most prominent. In the case of aptamers, the intramolecular assembly results in paired, helical structures and unpaired bulged or loop regions.² For unpaired stretches, further interactions are possible. One example is the formation of G-quadruplexes. This structural motif is characterized by sets of four Hoogsteen-bonded guanines that are arranged in a near planar fashion (G-tetrad). Several tetrads can stack on top of each other, forming a GQ which is stabilized by cations that are coordinated in-between the tetrads. Sites with the potential for GQ formation were found all over the genomes and transcriptomes of different species with significant enrichment in functional regions such as promoters or telomeres.²³⁹ Thus they were suggested to play a role in regulation of biological functions as they display for example repressive or progressive influence on translation *in vitro*.^{63, 67}

One aptamer combining specific target recognition with the structural GQ motif is AIR-3. AIR-3 was selected for binding to human Interleukin-6 receptor (hIL-6R) by Cindy Meyer in 2009 (published in 2012).¹⁹¹ Dysregulation of hIL-6R, its ligand Interleukin-6 (hIL-6) and the respective signaling cascade is connected with severity and progression of diseases as rheumatoid arthritis, multiple sclerosis and cancer.²⁰³⁻²⁰⁵ The 106 nt RNA aptamer AIR-3 has high affinity for recombinant hIL-6R ($K_d = 20$ nM). Its truncation AIR-3A, consisting of the 19 nt GQ forming binding motif, was shown to bind hIL-6R positive cells ($K_d = 8.5$ nM) and undergo endocytosis in complex with hIL-6R.²³² Recently, it was also used for targeted drug delivery of photosensitizer chlorin e6 and nucleoside analog 5-fluoro-2'-deoxyuridine (5-FdU).^{163, 212} Despite these advances in applications of AIR-3A, structural resolution remained limited to the discovery of the GQ which folds with parallel topology and the identification of essential guanines to maintain affinity.^{211, 232}

Part of this thesis dealt therefore with the elucidation of structural aspects of AIR-3 and AIR-3A not investigated so far.

6.1. Structural investigation of AIR-3 and AIR-3A

In course of this thesis, the dependency of AIR-3A GQ formation on cations was investigated.

In former works, this was analyzed with respect to Na^+ and K^+ presence, using thermal melting UV-spectroscopy and CD spectroscopy. Potassium dependent formation of a GQ in AIR-3A with a parallel stranded topology was revealed.²³²

Against this background, folding was now investigated under influence of different cations and cation concentrations.

6.1.1. Cationic influence and dimerization of AIR-3A

CD spectroscopy detected titration experiments are suitable to characterize folding kinetics and determine the GQ affinity for a certain cation as well as the reaction order. Use of ideal salt concentrations is beneficial to rule out unspecific cationic interactions that might falsify structure analysis. For AIR-3A titrations were conducted in presence of K^+ , Li^+ , Ba^{2+} , NH_4^+ and TMA^+ , and GQ formation was monitored as a difference in ellipticity at 262 nm. Concentrations ranged from 100 nM to 100 mM. Lithium was used as a control to represent the “unfolded” state as Li^+ cations are known to interfere with GQ folding.

For potassium, a $K_{1/2}^+$ value of $159 \pm 12 \mu\text{M}$ was found. This is remarkable, as assays were usually performed at K^+ concentrations of 10 mM, which is far beyond the saturation concentration found herein.²³² The fraction folded plot (Figure 12B) illustrated the saturation curve which contained one point of inflection. This indicated that only one binding site for K^+ and, consequently, two G-tetrads were present (two-tier GQ).

For comparison with the literature, a titration experiment on a GQ-forming RNA from *Arabidopsis thaliana* presented by Mullen *et al.* is shown in Figure 42. This example for the G3A G-quadruplex illustrates that fraction folding plots give valuable information on the reaction order. Two transitions were visible in that case, resulting in two different $K_{1/2}^+$ values.

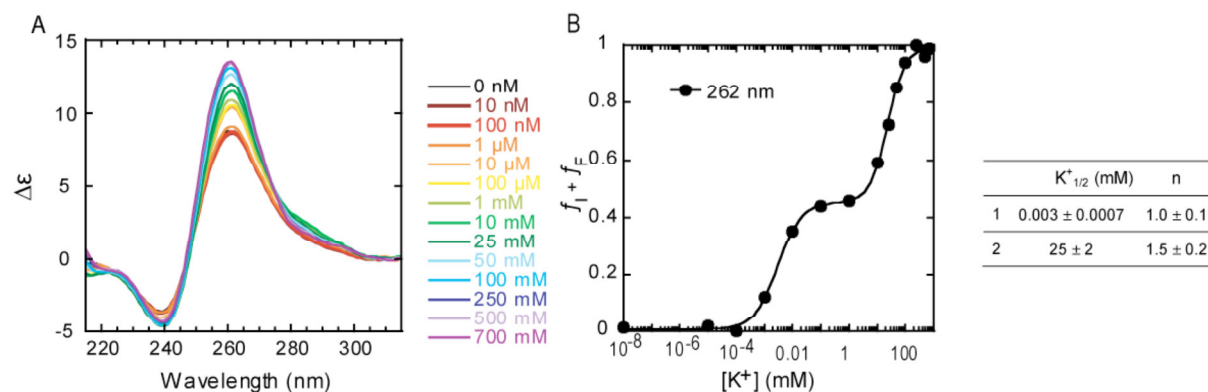


Figure 42: Exemplary illustration of a GQ (G3A) showing a two-transition folding. (A) CD titration and (B) fit to two transitions using a three state Hill Equation. Two transitions from unfolded to intermediate to fully folded were detected by K^+ titration on G3A. Figure taken unmodified and caption adapted from Mullen *et al.* (Figure S3).²²⁹

It can therefore be concluded that for AIR-3A only one transition occurred. Alternatively, the obtained data could be interpreted as simultaneous binding of two K^+ . The fit according to a two-state Hill equation resulted in a mean Hill-coefficient (representing the number of binding sites) of $n = 1.5$. Comparative fits with fixed parameters of $n = 1$ or $n = 2$ on this plot (Figure 43) showed that $n = 1$ displayed a less suitable fit than the assumption of two binding sites. Additionally, the determined value of 1.5 binding sites would match the hypothesis of AIR-3A dimers complexing three K^+ .

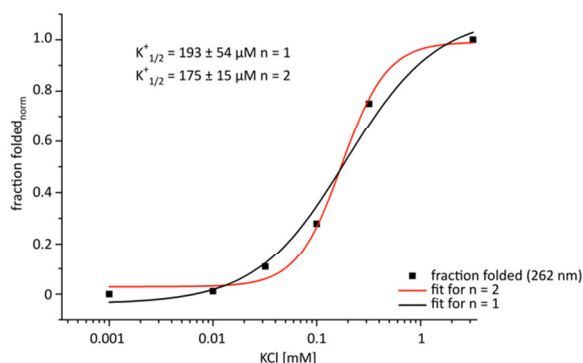


Figure 43: Comparative fits with fixed parameters for evaluation of the experimentally determined Hill coefficient (see Figure 12). To evaluate the fit obtained for the fraction folded plot of CD-detected K^+ titrations on AIR-3A, Hill coefficients were fixed to $n = 1$ (black curve) or $n = 2$ (red curve). As seen from the plot, the assumption of two K^+ bound fitted better with the data and resembled the experimental fit.

Also at higher K^+ concentrations, the amplitude did not increase in intensity which showed that saturation was reached at 1 mM. Another feature visible at higher K^+ concentrations was the appearance of a shoulder peak at 300 nm. According to Pandey *et al.*, this can indicate the presence of polymorphic GQ foldings.²⁴⁰ As expected due to its interference with GQ formation, Li^+ (1-100 mM) influenced the CD signal by keeping it less pronounced and on background level (Figure 13). The shallow curve remaining is caused by general base stacking which occurs independently from GQ formation.²⁴¹

The concentration dependency of CD signal intensity found for titrations with Ba^{2+} revealed coordination of this cation by AIR-3A. In this case, saturation was already reached at 320 μM (Figure 14). This reflects a greater affinity for Ba^{2+} compared to K^+ . Coordination and GQ-stabilizing effect of cations depend on charge and ionic radii. The ideal radius for coordination between two tetrads was found to be in the range of 1.3-1.5 Å.²²⁷ This corresponds to the ionic radius of K^+ (1.33 Å) as well as Ba^{2+} (1.34 Å). In fact, the twofold charge of Ba^{2+} has a greater potential for electrostatic compensation of the negatively charged oxygens in the GQ than K^+ . The fraction folded plot indicated presence of only one transition and Ba^{2+} affinity was calculated to 3.35 μM with $n = 2.4$ binding sites. But as AIR-3A displayed faster saturation with Ba^{2+} , the plot contained only one data point in the region of state-transition. The reaction order could therefore not be reliably determined.

Possible applications for barium cations coordinated within the GQ of AIR-3A are in the field of further structural investigations. Due to its high atomic number ($Z = 56$), Ba^{2+} is used as radiocontrast agent in X-ray imaging. This could be exploited insofar as GQ bound Ba^{2+} may function as inherent scattering agent in X-ray analysis of AIR-3A.

Ionic radius of ammonium cations (NH_4^+ , 1.43 Å) also proved to be suitable for GQ coordination.^{227, 242} For AIR-3A, this could be confirmed by CD-detected titration (Figure 15A). As one goal was to determine the number of K^+ complexed within the GQ motif and gain information on the number of tetrad, native MS analysis was conducted, a method which is also suitable to monitor dimerization events. Generally, native MS aims at preserving quaternary structures to investigate complex topologies and dynamics. Interference of salts (present in standard buffers) with the sample during the ionization process is ruled out by application of volatile buffers. Usually, ammonium acetate represents a suitable system for native MS applications. However, coordination of NH_4^+ by AIR-3A (confirmed by GQ formation in absence of K^+ and presence of NH_4^+) excluded this buffer system for the desired investigation. Trimethylammonium acetate (TMAA) represented an alternative which was successfully applied for AIR-3A in CD spectroscopy, allowing for GQ folding only when K^+ was added to the solution (Figure 15B). The TMA^+ cation is not complexed in the GQ, which is probably due to steric hindrance emanating from the methyl residues.

Thereby, buffer conditions were optimized and preliminary native MS results confirmed the presence of dimers in solution (Figure 16). As remnant salt hampered the detection of distinct aptamer/ K^+ -complexes, the determination of K^+ and, derived from that, tetrad numbers could not be achieved. Therefore, the desalting process will need to be optimized for future analysis by native MS. This could be realized by increasing the number of cycles of RNA precipitation and dissolving in TMAA (4.4.7) and better results might be obtained by precipitation of the RNA in presence of Li^+ prior to desalting. Also, several controls would need to be included as for example desalted AIR-3A omitting K^+ (to monitor if dimerization depends on GQ-formation and salt concentration), non-GQ forming G-rich oligonucleotides (to compare for K^+ binding under other structural conditions) and native MS in presence of target hIL-6R to review the theory of template-assisted dimerization. Finally, the optimized procedure could be applied to investigate coordination-behavior of other cations such as Ba^{2+} .

A complementary method to investigate cation dependent GQ formation that would give useful additional information is UV-detected thermal melting. Also, different RNA concentrations could be applied in UV- and CD spectroscopy to identify intermolecular interactions that influence melting temperatures and ellipticity. Especially concerning the dimerization hypothesis, this could be useful. In the present study, concentrations of 5 μ M were used in all titrations.

Dimerization was not only detected in MS analysis but also hinted at in different experimental results. As such, native PAGE analysis proved presence of higher migrating AIR-3A species in presence of K^+ which did not occur with Li^+ in the sample (Figure 17A). However, further bands next to the monomer in the Li^+ treated sample were observed. Probably this was due to K^+ present in the gel which led to formation of GQ intermediates during electrophoresis.

Microscale Thermophoresis (MST) indicated that the concentration stoichiometry of AIR-3A and hIL-6R was 2:1 in solution (Figure 18), which could either support the dimerization theory or the presence of two binding sites for AIR-3A.

Further validation of the dimerization process is needed. Additional experiments should include the investigation by MST in presence of Li^+ which would help to identify whether dimers or two monomers bind to hIL-6R. For native PAGE in presence of Li^+ , K^+ should be omitted completely. This could be achieved by analyzing K^+ and Li^+ treated AIR-3A in different gels, including controls for dimerizing and monomeric oligonucleotides each. In addition, different AIR-3A concentrations should be applied to detect possible concentration dependencies. Also, AIR-3A could be compared to other RNAs and DNAs with similar guanine content to reveal the cause of its apparent higher migration behavior. Figure 17B represents DLS data obtained for AIR-3A in preparation of small angle X-ray scattering (SAXS). Oligomerization of AIR-3A was visible at concentrations of 40 μ M under standard conditions using PBS. This reflects the aggregation behavior of AIR-3A and is in favor of dimerization and oligomerization. Also, it represents a drawback for approaches in crystallizing the aptamer as fast nucleation kinetics and disordered aggregation are disadvantageous with respect to crystal formation. As in crystallization homogeneity is a precept, another drawback would be a polymorphic character which was indicated for AIR-3A by CD spectroscopy.²⁴³ For the actual SAXS measurement, buffer conditions could be optimized to achieve homogeneous particles.

The SAXS experiment with AIR-3A was conducted by Katharina Berg, Erica Valentini and Eileen Magbanua (Hamburg) in an attempt to analyze the global shape and size of the aptamer. Figure 44 shows the results. Also, molecular modeling of the possible GQ structure was realized by Martin Zacharias (TU Munich). SAXS data were modeled to yield the *ab initio* shape as shown in the superimposition of DAMMIN and SASREF model (Figure 44A). The structural parameters suggested a dimeric formation and confirmed the results discussed above.

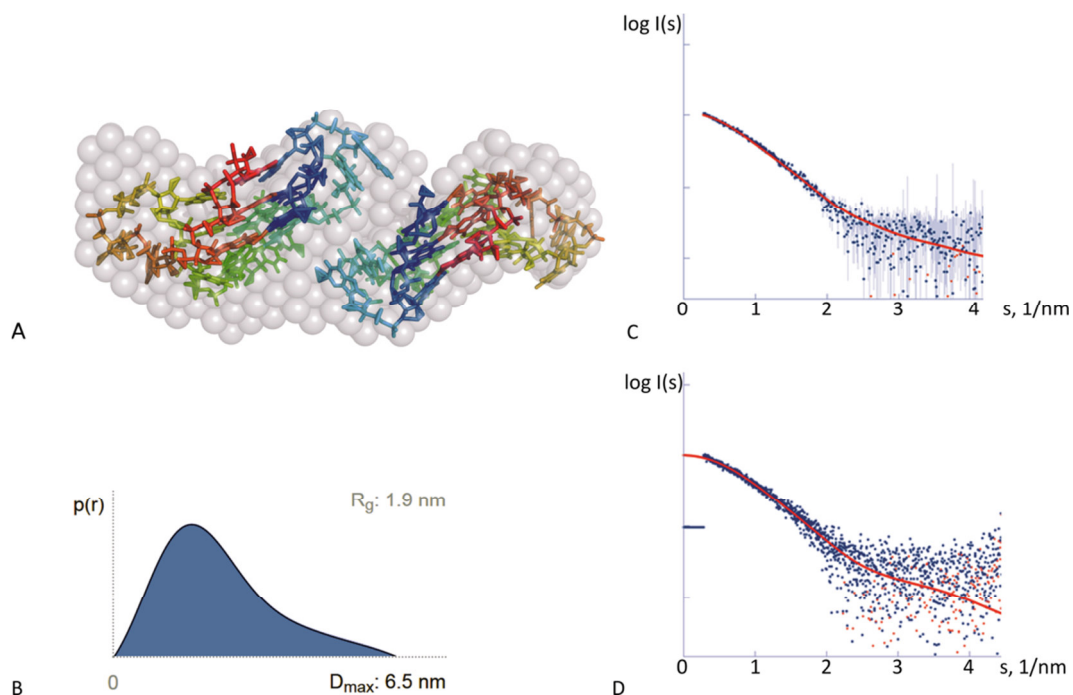


Figure 44: SAXS data for AIR-3A suggest dimer formation in solution. **A)** Superimposition of *ab initio* and hybrid models obtained with DAMMIN (gray semi-transparent spheres) and SASREF (rainbow-colored sticks). Two molecules of AIR-3A fit as **B)** Illustration of $p(r)$ distribution with derived structural parameters R_g and D_{max} . The goodness-of-fits for **(C)** DAMMIN ($\chi^2 = 1.118$) and **(D)** SASREF ($\chi^2 = 1.043$) models with SAXS experimental data represented as blue dots and fits as red curves (these experiments were performed and analyzed by Katharina Berg and Eileen Magbanua (Hamburg University both), in cooperation with Erica Valentini (EMBL Hamburg) and Martin Zacharias (TU Munich)).

The model supposed that dimerization occurred through tetrad stacking of two AIR-3A molecules (Figure 44A). The scattering curve is shown with superimposed fits (Figure 44C and D) as well as its Fourier transform $p(r)$ representing the pair distribution, which describes the distance between electrons from the scattering sample (Figure 44B). The collected data suggested a maximum particle distance (D_{max}) of 6.5 nm and the radius of gyration was calculated to $R_g = 1.9$ nm.

In summary, stoichiometric analyses pointed at an RNA:protein-ratio of 2:1. Taking into account that in solution oligomerization of AIR-3A was observed by PAGE, DLS and SAXS it can be assumed that the binding species is dimeric.

6.1.2. Structure probing for revelation of tetrad composition at nucleotide resolution

Based on the findings from the experiments on cationic influence, structure probing analyses were carried out on AIR-3 and AIR-3A. Methods applied in the past to resolve structural features at nucleotide resolution were for example Damage Selection, which helped to identify the binding motif¹⁹⁰ as well as nucleotide exchanges at different positions in AIR-3A to identify Gs that were essential for GQ integrity and target binding.²¹¹ The results showed that nucleotides G2, **G4**, G6, G7, **G10**, G12, G13, G15, **G17**, **G18**, **G19** were crucial and G3, A5, U11, A16 beneficial to maintain affinity and stability, while exchange of G1, C8, U9 and U14 displayed little to no influence. In summary,

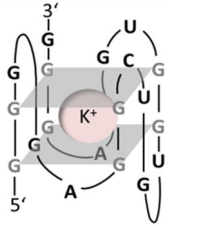
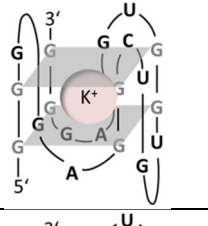
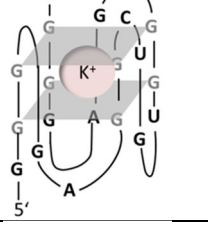
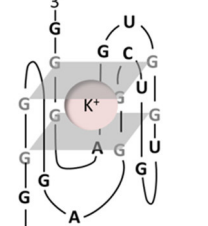
twelve out of thirteen guanines in AIR-3A were shown to have importance for the aptamer's function of which the five Gs shown in bold were suggested to take part in GQ folding as their exchange resulted in significantly reduced melting temperatures.^{197, 211}

For further discussion, analysis of AIR-3A using the QGRS mapper software (a tool that predicts probability of GQ formation in quadruplex forming G-rich sequences)²³³ was looked at.

The calculations revealed that two-tier QGs of AIR-3A are thermodynamically favored. The tool predicts eleven overlapping GQs of which those that contain 19 or 18 nt as well as the hypothesized 17 nt GQ (Figure 10) are listed in Table 26. Shorter predicted GQs were omitted as from the nucleotide exchange analyses relevance of nucleotides present in position G2 to G19 was proved. The probability of occurrence is represented by the G-score which can reach a maximum value of 21 (high probability). The most probable foldings predicted for AIR-3A with scores of 19 and 20 are depicted in the first column (Table 26).

Variation between them is characterized by differences in contribution of the 5'- and 3'-terminal Gs. In general, these three resemble each other and their co-existence is probable due to their similar and high G-scores. Furthermore the high number of Gs located in the termini might cause a switching in their GQ integration which would contribute to the heterogeneity of foldings. The four less probable variants neglect contributions of central guanines to the GQ and will not be discussed further.

Table 26: Probable GQs in AIR-3A as predicted by QGRS mapper.

scheme	nt	AIR-3A section (5'→3' direction) GQ motif underlined	G-score
	18	<u>GGGGAGGCUGUGGGUGAGG</u>	20
	19	<u>GGGGAGGCUGUGGGUGAGGG</u>	20
	18	<u>GGGAGGCUGUGGGUGAGGG</u>	19
	17	<u>GGGAGGCUGUGGGUGAGG*</u>	19
-	18	<u>GGGGAGGCUGUGGGUGAGG</u>	14
-	19	<u>GGGGAGGCUGUGGGUGAGGG</u>	14
-	18	<u>GGGGAGGCUGUGGGUGAGG</u>	12
-	19	<u>GGGGAGGCUGUGGGUGAGGG</u>	11

*formerly hypothesized folding of AIR-3A¹⁹⁷

In theory, AIR-3A could also form three-tier GQs, but due to the fact that this is thermodynamically inconvenient, neither predictions nor G-scores were determinable. For the sake of completeness, however, one example is presented in Figure 45. In this hypothesized three-tier GQ, all guanines except for G1 would be involved in GQ formation. The connecting loops contain only one nucleotide each. Also, bulges formed by C8 and U9 as well as by U14 would be present.

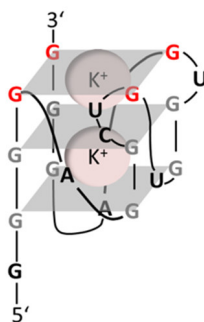


Figure 45: Assumption of a three-tier GQ formed by AIR-3A. Hypothetic folding of AIR-3A into a three-tier parallel stranded quadruplex complexing two K^+ .

Although this folding model integrates all relevant Gs into the GQ, it is unlikely to form. The loops in this model are much shorter than in the high scored folding predictions (Table 26). Although large loops can destabilize GQ integrity³⁰ and increase nuclease susceptibility, loops in general often mediate interactions²⁴⁴ and may therefore be beneficial for AIR-3A affinity towards hIL-6R.

Now, these findings were complemented with secondary structure analysis by in-line probing (ILP) and RNase T1 protection assays to gain more information on the identity of quadruplex associated guanines. Protection from RNase T1 cleavage is a method particularly suitable for GQ investigations as it probes only Gs. The endoribonuclease specifically cleaves guanine residues in unpaired RNA strands. Gs that are involved in G-tetrad formation are thereby less susceptible to RNase attack. Thus, RNAs that form G-quadruplexes display a different cleavage pattern under conditions promoting GQ folding (K^+ present) compared to being unfolded.

An approach that is suitable to generally monitor structural deviations in RNA under different conditions is in-line probing. This method probes susceptibility of nucleotides towards hydrolysis under slightly alkaline conditions (pH 8.3). It can for example be used to identify nucleotides involved in target interaction. Also, folded and unfolded GQs can be analyzed as Gs undergoing tetrad-formation become less susceptible to in-line cleavage.

Both methods have in common that by cleavage RNA fragments are generated which can be separated (e.g. by gel electrophoresis) and quantified to identify positions that are differentially affected depending their folding state.

Structure probing analyses on AIR-3 and AIR-3A revealed a general T1 protection of Gs in the GQ region and also observed ILP reactivities among them were similar. This gives rise to the assumptions that

- either all Gs took part in GQ formation, forming a three-tier bulged GQ (Figure 45) or
- different GQ foldings co-existed at once of which protection/reactivity patterns overlaid in the probings, resulting in similar signal intensities for all Gs.

In conclusion, this indicated that the hypothesized GQ structure (Figure 10) is only one of several possible foldings. These could be further analyzed and differentiated by structural analyses of AIR-3

variants with different G exchanges as for example the variants tested in former studies.²²⁶ In a first step, the retained ability for GQ formation as well as target affinity should be confirmed. Reducing the variability for tetrad contribution among the guanines might then decrease the polymorphic properties.

In detail, the analysis of AIR-3 confirmed the probability for C39 to U42 to form a loop region. Moreover, the reactivity profile indicated predicted loop positions A36, U42, U45, G46 and A47 as well as tetrad associated G37 and G43 to take part in target interaction. Another new observation was the shift in reactivity for GQ flanking sites C26 to U30 and A52 to U55 in presence of hIL-6R. A possible explanation is an induced fit mechanism, causing the AIR-3 quadruplex to adopt an energetically favorable conformation when interacting with the target protein. Yet, also in presence of hIL-6R, no singular folding was observed.

From the findings on GQ folding it can be assumed that AIR-3A is polymorphic. The other possibility of AIR-3A forming a three-tier bulged QG is less probable when data from SAXS and molecular modeling (see 6.1.1) are included, because then the RNA model can no further be superimposed on the SAXS models. One discrepancy facing polymorphism of AIR-3A represents its high affinity to target protein hIL-6R and the fact that AIR-3A cannot be eluted from the surface of target cells by high salt washes. This means that binding cannot be exclusively mediated by ionic interactions.

6.2. Derivatization of AIR-3 and AIR-3A

Next to structural aspects, also derivatives of AIR-3 and AIR-3A were investigated in the present study. On the one hand, a drug delivery approach with nucleoside analog gemcitabine was conducted based on recent findings by Kruspe *et al.*^{163, 212} On the other hand, derivatization with deoxy pyrimidines was assayed as a complementation to former findings on base- and sugar-modifications of the aptamers.^{226, 245}

Gemcitabine is a therapeutically relevant analog of cytosine with cytostatic properties which is applied in pancreatic cancer therapy.^{156, 157} Nucleoside analog delivery was already realized for AIR-3 by derivatization with 5-fluoro-2'-deoxyuridine (5-FdU), using the aptamer as a potent prodrug.²⁴⁰ Now gemcitabine, included as intrinsic modification in AIR-3, was tested for its cytotoxic potential towards target cells (BaF3_hIL-6R). Different AIR-3 variants comprising gemcitabine, 5-FdU, stabilized pyrimidines (2'FU and 2'FC) or combinations of these were investigated.

Variants were successfully produced by *in vitro* transcription and analyzed for stability and target affinity. It was found that gemcitabine provided a stabilizing modification, especially in combination with 5-FdU or 2'FU, where half-lives significantly increased from less than one minute for the unmodified aptamer to 51 min and > 200 min, respectively. Affinity towards hIL-6R was tested by filter retention assays and cellular binding and was confirmed for all tested variants. This represents a

remarkable feature of AIR-3 as it was now shown to bear intrinsic modification by two different nucleoside analogs as well as 2'-F-pyrimidines under retained binding capacity.

Although target cells were generally susceptible to gemcitabine as confirmed in the dose response assay (Figure 27), no specific cytostatic effect was obtained by treatment with AIR-3 derivatives containing only gemcitabine as a drug (Figure 28; AIR-3-Gem, AIR-3-Gem-2'FU, AIR-3-2'FU-2'FC). Only when combined with 5-FdU, specific cytotoxicity was observed as decreased proliferation and S-phase arrest (Figure 29 and Figure 30). However, the contribution of gemcitabine to the observed effects remained unclear. Compared to AIR-3-5FdU, effects of AIR-3-Gem-5FdU were found to be pronounced only 72 h after treatment with the prodrug.

As gemcitabine provided a further stabilizing modification in AIR-3 bearing 5-FdU, it is possible that after cellular uptake, lysosomal degradation of the aptamer was slowed down compared to AIR-3-5FdU resulting in a delayed effect. As gemcitabine, similar to 5-FdU, causes S-phase arrest,²³⁵ cell cycle analyses did not provide sufficient information to discriminate between effects of the two drugs applied simultaneously. For future gemcitabine delivery approaches it would therefore be sensible to analyze treated cells additionally by other means. For example, occurrence of gemcitabine induced DNA strand breaks could be detected by TUNEL (Terminal deoxynucleotidyl transferase dUTP nick end labeling) assay. This method is suitable to selectively identify DNA strand breaks that result from apoptotic signaling cascades. Different causes of cell death can thereby be differentiated. During the assay, nicked DNA is *in situ* 3'-end labeled by the enzyme terminal deoxynucleotidyl transferase, which catalyzes the addition of dUTP (fluorescently or otherwise labeled). Fluorescent detection of the added dUTPs allows for fast quantification of damaged DNA in cell populations by Flow Cytometry.²⁴⁶⁻²⁴⁸

Deoxy modifications applied on the one hand as deoxy pyrimidine integrations (AIR-3-dC-dU and AIR-3A-dC-dU; Figure 32) and on the other hand as an all-DNA analog of AIR-3 (DNA_AIR-3; Figure 33) turned out to interfere with the binding capacity of AIR-3 and AIR-3A, causing complete loss of affinity. Therefore, they were no suitable means of stabilization.

Exchange of all nucleotides including guanines with deoxy analogs might have led to disturbed formation of the GQ as DNA is less likely to adopt the all-parallel GQ topology found in AIR-3(A). This may explain the negative impact on target affinity, and could be assayed further by CD spectroscopic analyses. As also exchange of pyrimidines only resulted in loss of affinity, it can be assumed that conformational changes occurred, causing the secondary structure and global shape of the aptamer to form differently as to not allow specific target interaction. This change on the level of secondary structures and GQ formation could be proven by adequate structure probing approaches (DMS probing, cation dependent RT pausing). With regard to this it has to be noted that hIL-6R specific DNA aptamer AID-1²²¹ forms a GQ as well. The deviation in primary sequence between the

two aptamers is therefore supposed to be a crucial factor allowing GQ formation in AID-1 but not in DNA analogs of AIR-3(A).

With these findings, in-depth exchange possibilities in AIR-3 were examined, which in summary represent the tolerance of this aptamer to be modified for use in different applications. Here, the presence of the GQ forming binding motif represents a benefit because as long as GQ formation is ensured, maintained binding capacity is probable. Modifications can therefore be applied more easily compared to differently structured RNAs, as quadruplexes are very stable and form with high cooperativity. This stability renders the oligonucleotides also less susceptible to nuclease degradation, a fact that can be enhanced by introduction of stabilizing nucleotide modifications as long as they don't interfere with GQ folding.

6.3. Analyses on AIR-3A target specificity

AIR-3A displays specific binding towards its target hIL-6R. Yet, as G-quadruplex forming oligonucleotides often show binding towards other targets (especially to so-called G-quadruplex binding proteins), side specificities of AIR-3A were investigated. As such, binding was assayed on thrombin (a protein for which two different GQ-forming DNA aptamers (TBA and HD22)^{227, 236} were selected) and different cell lines with varying expression levels of hIL-6R. Additionally, AIR-3A-aided pull-down assays of cellular proteins from cell extracts were performed and analyzed by LC-MS to identify proteins that are targeted by the aptamer.

By filter retention analysis, concentration dependent binding of radio labeled AIR-3A to thrombin ($K_d = 343 \pm 44$ nM) was detected. Thrombin is supposed to have general affinity for GQs as from two independent SELEX approaches, GQ forming aptamers emerged. Compared to hIL-6R binding ($K_d = 60$ nM), thrombin is bound with less affinity which might be due to the fact that thrombin has specificity rather to anti-parallel than to parallel GQs. Usually, dissociation constants of GQs for their binding proteins are in the low nanomolar range.¹⁰⁷ This finding can be regarded as a proof of principle and would need to be proved by binding studies on other GQ binding proteins such as nucleolin or FMRP, which have affinity for RNA GQs.^{111, 118} Unspecific binding is supposed to occur especially towards basic proteins as GQs create a polyanionic shape with high charge density.²³⁹

Although the number of identified proteins that specifically bind GQs constantly increases, no common features or proof of function were constituted. As not only binding but also manipulation (e.g. stabilization/destabilization) of GQs by proteins was found, a link to regulative mechanisms seems likely.²³⁹

Concerning cell specificity of AIR-3A, observed affinities were not necessarily correlated with expression levels of hIL-6R (Figure 35) as analyzed by Flow Cytometry detection of immunostains and fluorescently labeled aptamer. As such, cell lines LNCaP, PC3 and HeLa showed aptamer binding but

displayed only a marginal shift in hIL-6R detection. It may be that due to its GQ formation, AIR-3A is has affinity for other membrane bound proteins as well or, as non-GQ forming control AIR-3A_G17U was bound to a similar extent as AIR-3A by RPMI 8226, PC3, LNCaP and HEK 293, unspecific RNA binding occurred.

The central aim of the subsequent pull-down experiments from cell extracts (from BaF3_hIL-6R, HEK 293 and HeLa) was to isolate and identify proteins that bind to AIR-3A as a GQ. Captured proteins revealed several bands in SDS-PAGE analysis (Figure 36) which argues for unspecific protein binding. The next step to elucidate aptamer-protein interactions was the mass spectrometric analysis of selected bands that occurred in presence of AIR-3A, but not when magnetic beads only or non-specifically binding RNA (tRNA and non-GQ forming control AIR-3A_G17U) were present (Figure 36). One band from the BaF3_hIL-6R samples and two bands from HeLa pull-downs were selected. For each sample, the respective region in the control experiment was analyzed as well. HEK 293 pull-downs yielded no visible differences.

From the results obtained by LC-MS analysis, it was discovered AIR-3A binds other proteins of which some are exclusively targeted as they are not found in the control experiment using non-GQ RNA (Table 25). Although it was probable that AIR-3A targets other proteins next to hIL-6R that have affinity for GQs, no popular candidates were identified as specific targets of AIR-3A. For instance, nucleolin was identified in both the experiment and the control pull-down (Table 25). In general, the identified proteins were mainly either of RNA binding character (e.g. heterogeneous nuclear ribonucleoprotein R), cytoskeletal proteins (e.g. actin, tubulin, vimentin) or common contaminants such as keratin. Binding to cytoskeletal proteins reflects their high abundance rather than specific binding as was already suggested by von Hacht *et al.*¹⁰⁷ From the fact that not even in the positive control (using AIR-3A for protein pull-down from lysate of BaF3_hIL-6R target cells) the target protein hIL-6R was detected, it can be assumed that basic optimization of the capturing procedure and/or MS analysis would be needed to obtain reliable results. Also, different salt concentrations should be tested during incubation and elution, to exclude unspecific RNA binding. To test the capturing assay in the first place and assure recovery of targeted proteins, addition of recombinant hIL-6R to the lysate could serve as a proof of principle.

The impact of the proteins exclusively recognized by AIR-3A might then gain importance and could be further analyzed regarding their affinity towards other GQs and the characteristics of molecular interactions between GQs and proteins. In this manner, binding motifs could be identified that are not known to date. As the functions and properties of GQ binding proteins are not yet fully understood but remain subject of research, future findings may help to understand how interactions between GQs and proteins are connected with regulative properties.

Another considerable aspect is the possibility that the target molecule hIL-6R may be a GQ binding protein itself. Next to AIR-3, two other aptamers (AID-1 and RAID3), independently selected for hIL-6R, were shown to form GQs.^{209, 210} Additionally, AID-1 also has affinity for HIV-1 integrase which in turn is known to bind GQs.²⁴⁹ In contrast, aptamer TBA with specificity for thrombin does not bind to hIL-6R.

Recently, von Hacht *et al.* identified several GQ binding proteins serving as targets for mRNA G-quadruplexes that were found to usually have exclusive affinity for specific targets.¹⁰⁷ Against this background, side affinities for hIL-6R specific GQ aptamers can be considered as expected.

Recapitulatory, the general possibility of AIR-3A binding to other proteins and cells with very low expression levels of hIL-6R was shown. Binding occurred in a concentration dependent manner even though it may be mediated by unspecific interactions, as the outcome of pull-down assays suggests. The impact that the G-quadruplex motif in the aptamer has on these protein interactions remains to be clarified as does the role of hIL-6R in GQ binding. Yet, it should be kept in mind that the proposed induced fit mechanism, indicated by conformational changes in AIR-3 upon binding (6.1.2), argues for specific structural features of AIR-3A, making it suitable for strong and selective interaction with hIL-6R depending on the environmental conditions. There are numerous questions that remain to be solved concerning the common properties of GQ binding proteins as well as the endogenous functions and the interplay of the GQs targeting them.

6.4. Endocytic fate

Receptor mediated endocytosis is the common endocytic path among signal transduction associated receptors and it often is clathrin mediated. Lysosomal localization of hIL-6R was known to occur²³⁸ and has also been suggested for AIR-3A.^{197, 211} In this work, the aptamer's influence on subcellular localization and turnover of hIL-6R were investigated as well as the endocytic whereabouts of AIR-3A itself.

By means of antibody detection, hIL-6R was co-localized with lysosomes and partially with transferrin (mTrf), which is an indicator for clathrin mediated endocytosis. AIR-3A co-localized with subcellular hIL-6R signals partially and its fluorescence was vesicularized, which suggested that the fluorescent species was trapped within the vesicle. As expected from the results obtained from hIL-6R, AIR-3A also showed partial co-localization with mTrf. From the fact that some foci were spotted independently, AIR-3A and hIL-6R may not be limited to the clathrin mediated pathway. Lysosomal localization of the aptamer was confirmed. Whether this represents a naturally occurring phenomenon or was merely induced by antibody interaction remains unclear. A more reliable method would be the detection of ligand hIL-6 to monitor trafficking and the natural incidence of lysosomal fate of hIL-6R.

The influence of AIR-3A presence on the abundance of lysosomal degradation was not clearly resolved. A hint towards this assumption is the reduction of hIL-6R immunofluorescence with aptamer present compared to other effectors (Figure 41). On the one hand, AIR-3A could have an impact on hIL-6R presentation on the cellular surface, but as fluorescence decay was shown to be larger than in presence of the actual target hIL-6, the aptamer must take a part in cellular regulation that is not yet understood. On the other hand, fluorescent detection of anti-hIL-6R antibody was realized using APC-labeled secondary antibody. APC is a protein and is thereby more likely to be affected by lysosomal degradation in its fluorescence properties than other organic dyes. Therefore, experiments could be repeated with another dye sturdier in presence of lysosomal enzymes such as for example fluorescein or rhodamine based dyes. Consequently, increased degradation of APC by lysosomal proteases would explain decreased fluorescence and argues for increased lysosomal fate of hIL-6R after interaction with AIR-3A. All these findings give rise to the consideration that AIR-3A might possess regulatory function on cellular endocytosis of hIL-6R and possibly other processes. This may be connected with the fact that AIR-3A is supposed to bind hIL-6R in domain D1 which is responsible for hIL-6R transport.¹⁹⁵ To clarify if regulative effects of AIR-3A exist, further investigations would need to be considered. As such, one possibility would be to monitor changes in cellular mRNA levels in response to AIR-3A treatment, detected by deep sequencing.

In this context, a predicted mRNA for RASSF1, a gene encoding Ras association domain-containing protein 1, might represent an interesting study subject for further investigation. If verifiable, this mRNA may represent a natural equivalent of AIR-3A, as it contains a variant of this aptamer (AIR-3A_C8A_U14A). It could function as a possible control element for Ras protein signal transduction. By signal transduction induced upon hIL-6 binding, hIL-6R is linked to this signaling pathway. How interaction between this membrane-bound receptor and a possible cellular mRNA could take place remains however questionable.

Possible first experiments to link this mRNA to possible regulatory functions of AIR-3A include a) verification of its existence for example by RT-PCR, b) template generation and *in vitro* transcription of the respective fragment, c) evaluation of hIL-6R affinity, d) intracellular cross-linking of the mRNA and isolation of cross-linked associated proteins.

This hypothesis is vague and would need intense consideration. However, regulative effects of AIR-3A, such as modulation of hIL-6R uptake and trafficking, represent an interesting field to continue research on this aptamer, as it may help to increase understanding of dysregulations in hIL-6R homeostasis which are associated with inflammation and disease.

7. Future prospects

In the present study, insight into the structural properties and target specificity of hIL-6R RNA aptamer AIR-3A was gained. Although this GQ forming aptamer has been dealt with in earlier publications and was subjected to intensive characterization, the focus lay now on clarification of GQ folding in dependence of cation presence and identity and the contribution of nucleotides to quadruplex formation as well as target binding interaction. It turned out that several features had been undiscovered so far. In this regard, it was found that no specific structuring can be determined, but that AIR-3A displays a polymorphic GQ and that it is likely to oligomerize in solution as well as in presence of target molecule hIL-6R.

Concerning structural elucidation of AIR-3 and AIR-3A, it can be assumed that, due to the polymorphic character of the GQ, further analyses should be conducted on less variable variants. Design of aptamers derived from AIR-3A that fold into defined quadruplexes may be beneficial with regard to the possibility of broadening the scope of analysis methods applicable. As such, NMR and X-ray crystallography could yield valuable information on the 3D-structure as well as on the process of folding and the degree of association.

Comparison of different variants could then help to investigate the interaction surfaces of RNA and protein and gain knowledge on the properties that make hIL-6R a suitable target for GQs. With the polymorphic AIR-3A, these methods cannot be used, as signals of the different species overlay and impede analysis.

Regarding secondary structure analyses, AIR-3A variants could be subjected to chemical and enzymatic probing. Here, SHAPE could be another option to identify flexible nucleotide positions.²⁵⁰ Also probing with RNase U2,⁴⁷ which cleaves A-specific, could be used as a complement to RNase T1. Footprinting experiments in presence of hIL-6R could then also help to find out which nucleotides mediate target interaction.^{251, 252} Interaction could further be monitored by UV cross-linking experiments as presented in former works.^{197, 245} These approaches could be optimized for identification of amino acid residues involved in RNA binding.²⁵³⁻²⁵⁵

In this work, the proposed lysosomal fate of AIR-3A after cellular uptake¹⁹⁷ was confirmed. For future investigations, the cellular whereabouts and trafficking, as well as stability of the aptamer are of interest. This could be examined in a time resolved manner. On the one hand, it could be achieved by co-localization with further cellular compartments using faster techniques compared to cLSM such as confocal spinning disc laser microscopy. Also, double labeled AIR-3A (two different fluorescent dyes

conjugated to 5'- and 3'-end allowing for Förster resonance energy transfer (FRET)) could thereby be followed throughout the cell with the benefit of detecting degradation of the aptamer as a decay of FRET signal intensity and differentiation of the fluorescence of the two dyes. Another method yielding high spatial and time resolution is represented by in-liquid transmission electron microscopy (TEM).²⁵⁶ This novel technique was already applied for visualization of DNA functionalized gold nanoparticles as a proof that electron microscopy works in aqueous solution, and it is currently worked on for application in cellular detection. Against this background, coordination of cations with scattering potential (such as Ba²⁺) could serve as a labeling to visualize AIR-3A during endocytosis and inside the cell by in-liquid TEM. Further cations suitable in this respect, such as Sr²⁺, could be analyzed by CD detected titrations as well.

To quantify cellular uptake of AIR-3A as well as its stability, quantitative real time PCR could be applied.²⁵⁷ After incubation with AIR-3A, surface bound aptamer could be removed and cells cultured for different time periods, after which total RNA is isolated and analyzed by RT-PCR for abundance of AIR-3A. This could give information on the extent of lysosomal degradation and help to compare intracellular stability of derivatized AIR-3(A). Also, influence of aptamer treatment on the transcriptome could be investigated with respect to regulative properties.

Before further aptamer aided drug deliveries are established, stabilization of AIR-3A should be focused on. Next to 2'F modifications (which are only applicable for AIR-3, but not for AIR-3A), integration of 3'-inverted thymidine or 5'-PEG could increase the half-life.¹³¹

The efficiency of drug delivery and release could be improved by addition of endosomal escape agents.¹⁰⁶ This would for example enable application of siRNA-AIR-3A conjugates. Targeted delivery could also be achieved by aptamer-functionalized drug-encapsulating liposomes.²⁵⁸ This would increase the drug load per aptamer molecule and result in a more pronounced cytotoxic effect.

Further targets of AIR-3A could be identified by intracellular crosslinking. However, in preparation of such experiments, optimization of the pull down experiments established in this study would be necessary to verify AIR-3A specificity and reproducibility of the assay.

To tackle the task of signaling inhibition, experiments could be designed to multimerize AIR-3A in a controlled manner. Alternatively, conjugation of AIR-3A and RAID3 would be possible. This could result in an aptamer derivative with higher affinity and slower off rate. Although neither RAID3 nor AIR-3A alone affect receptor interaction with hIL-6 or gp130, the conjugate might interfere with it by sheer size.

Finally, the other aptamers with hIL-6R specificity could be subjected to further analysis. As such, identification of the binding site of AID-1 might give insight into the GQ binding potential of the receptor. Especially as AID-1 was shown to compete for binding with AIR-3A,²⁵⁹ and is therefore supposed to target the same site, this could yield valuable information. RAID3 showed no competition and therefore complements AIR-3A. Structural analyses could be performed to further characterize this aptamer. As RAID3 has already been stabilized and was shown to be internalized by target cells, it represents an alternative tool for aptamer mediated drug delivery using the hIL-6R system.

8. References

1. Watson JD, Crick FH. Molecular structure of nucleic acids; a structure for deoxyribose nucleic acid. *Nature* 1953; 171:737-8.
2. Moore PB. Structural motifs in RNA. *Annual review of biochemistry* 1999; 68:287-300.
3. Hendrix DK, Brenner SE, Holbrook SR. RNA structural motifs: building blocks of a modular biomolecule. *Quarterly reviews of biophysics* 2005; 38:221-43.
4. Mukundan VT, Phan AT. Bulges in G-quadruplexes: broadening the definition of G-quadruplex-forming sequences. *Journal of the American Chemical Society* 2013; 135:5017-28.
5. Petersheim M, Turner DH. Base-stacking and base-pairing contributions to helix stability: thermodynamics of double-helix formation with CCGG, CCGGp, CCGGAp, ACCGGp, CCGGUp, and ACCGGUp. *Biochemistry* 1983; 22:256-63.
6. Phillips K, Dauter Z, Murchie AI, Lilley DM, Luisi B. The crystal structure of a parallel-stranded guanine tetraplex at 0.95 Å resolution. *Journal of molecular biology* 1997; 273:171-82.
7. Sundquist WI, Klug A. Telomeric DNA dimerizes by formation of guanine tetrads between hairpin loops. *Nature* 1989; 342:825-9.
8. Henderson E, Hardin CC, Walk SK, Tinoco I, Jr., Blackburn EH. Telomeric DNA oligonucleotides form novel intramolecular structures containing guanine-guanine base pairs. *Cell* 1987; 51:899-908.
9. Macaya RF, Schultze P, Smith FW, Roe JA, Feigon J. Thrombin-binding DNA aptamer forms a unimolecular quadruplex structure in solution. *Proceedings of the National Academy of Sciences of the United States of America* 1993; 90:3745-9.
10. Rachwal PA, Brown T, Fox KR. Effect of G-tract length on the topology and stability of intramolecular DNA quadruplexes. *Biochemistry* 2007; 46:3036-44.
11. Huppert JL. Four-stranded nucleic acids: structure, function and targeting of G-quadruplexes. *Chem Soc Rev* 2008; 37:1375-84.
12. Huppert JL. Structure, location and interactions of G-quadruplexes. *The FEBS journal* 2010; 277:3452-8.
13. Bang I. Untersuchungen über die Guanylsäure. *Biochemische Zeitschrift* 1910; 26.
14. Davis JT. G-quartets 40 years later: from 5'-GMP to molecular biology and supramolecular chemistry. *Angew Chem Int Ed Engl* 2004; 43:668-98.
15. Gellert M, Lipsett MN, Davies DR. Helix formation by guanylic acid. *Proceedings of the National Academy of Sciences of the United States of America* 1962; 48:2013-8.
16. Tran PL, De Cian A, Gros J, Moriyama R, Mergny JL. Tetramolecular quadruplex stability and assembly. *Top Curr Chem* 2013; 330:243-73.
17. Ida R, Wu G. Direct NMR detection of alkali metal ions bound to G-quadruplex DNA. *Journal of the American Chemical Society* 2008; 130:3590-602.
18. Reshetnikov RV, Sponer J, Rassokhina OI, Kopylov AM, Tsvetkov PO, Makarov AA, et al. Cation binding to 15-TBA quadruplex DNA is a multiple-pathway cation-dependent process. *Nucleic acids research* 2011; 39:9789-802.
19. Bishop JS, Guy-Caffey JK, Ojwang JO, Smith SR, Hogan ME, Cossum PA, et al. Intramolecular G-quartet motifs confer nuclease resistance to a potent anti-HIV oligonucleotide. *The Journal of biological chemistry* 1996; 271:5698-703.
20. Cao Z, Huang CC, Tan W. Nuclease resistance of telomere-like oligonucleotides monitored in live cells by fluorescence anisotropy imaging. *Anal Chem* 2006; 78:1478-84.
21. Hardin CC, Watson T, Corregan M, Bailey C. Cation-dependent transition between the quadruplex and Watson-Crick hairpin forms of d(CGCG3GCG). *Biochemistry* 1992; 31:833-41.
22. Lane AN, Chaires JB, Gray RD, Trent JO. Stability and kinetics of G-quadruplex structures. *Nucleic acids research* 2008; 36:5482-515.
23. Galezowska E, Gluszynska A, Juskowiak B. Luminescence study of G-quadruplex formation in the presence of Tb³⁺ ion. *Journal of inorganic biochemistry* 2007; 101:678-85.

24. Worlinsky JL, Basu S. Detection of quadruplex DNA by luminescence enhancement of lanthanide ions and energy transfer from lanthanide chelates. *The journal of physical chemistry B* 2009; 113:865-8.
25. Gilli GB, F.; Ferretti, V.; Bertolasi, V. Evidence for resonance-assisted hydrogen bonding from crystal-structure correlations on the enol form of the beta-diketone fragment. *J Am Chem Soc* 1989; 111:1023-8.
26. Fonseca Guerra C, Zijlstra H, Paragi G, Bickelhaupt FM. Telomere structure and stability: covalency in hydrogen bonds, not resonance assistance, causes cooperativity in guanine quartets. *Chemistry* 2011; 17:12612-22.
27. Laguerre A, Stefan L, Larrouy M, Genest D, Novotna J, Pirrotta M, et al. A twice-as-smart synthetic G-quartet: PyroTASQ is both a smart quadruplex ligand and a smart fluorescent probe. *Journal of the American Chemical Society* 2014; 136:12406-14.
28. Rhodes D, Lipps HJ. G-quadruplexes and their regulatory roles in biology. *Nucleic acids research* 2015; 43:8627-37.
29. Burge S, Parkinson GN, Hazel P, Todd AK, Neidle S. Quadruplex DNA: sequence, topology and structure. *Nucleic acids research* 2006; 34:5402-15.
30. Guedin A, Gros J, Alberti P, Mergny JL. How long is too long? Effects of loop size on G-quadruplex stability. *Nucleic acids research* 2010; 38:7858-68.
31. Agarwala P, Pandey S, Maiti S. The tale of RNA G-quadruplex. *Organic & biomolecular chemistry* 2015; 13:5570-85.
32. Smith FW, Feigon J. Quadruplex structure of *Oxytricha* telomeric DNA oligonucleotides. *Nature* 1992; 356:164-8.
33. Gavathiotis E, Searle MS. Structure of the parallel-stranded DNA quadruplex d(TTAGGGT)₄ containing the human telomeric repeat: evidence for A-tetrad formation from NMR and molecular dynamics simulations. *Organic & biomolecular chemistry* 2003; 1:1650-6.
34. Cheong C, Moore PB. Solution structure of an unusually stable RNA tetraplex containing G- and U-quartet structures. *Biochemistry* 1992; 31:8406-14.
35. Vasilyev N, Polonskaia A, Darnell JC, Darnell RB, Patel DJ, Serganov A. Crystal structure reveals specific recognition of a G-quadruplex RNA by a beta-turn in the RGG motif of FMRP. *Proceedings of the National Academy of Sciences of the United States of America* 2015; 112:E5391-400.
36. Patel PK, Hosur RV. NMR observation of T-tetrads in a parallel stranded DNA quadruplex formed by *Saccharomyces cerevisiae* telomere repeats. *Nucleic acids research* 1999; 27:2457-64.
37. Zhang N, Gorin A, Majumdar A, Kettani A, Chernichenko N, Skripkin E, et al. V-shaped scaffold: a new architectural motif identified in an A x (G x G x G x G) pentad-containing dimeric DNA quadruplex involving stacked G(anti) x G(anti) x G(anti) x G(syn) tetrads. *Journal of molecular biology* 2001; 311:1063-79.
38. Kettani A, Gorin A, Majumdar A, Hermann T, Skripkin E, Zhao H, et al. A dimeric DNA interface stabilized by stacked A.(G.G.G.G).A hexads and coordinated monovalent cations. *Journal of molecular biology* 2000; 297:627-44.
39. Lu M, Guo Q, Kallenbach NR. Thermodynamics of G-tetraplex formation by telomeric DNAs. *Biochemistry* 1993; 32:598-601.
40. Mergny JL, Phan AT, Lacroix L. Following G-quartet formation by UV-spectroscopy. *FEBS letters* 1998; 435:74-8.
41. Kypr J, Kejnovska I, Renciuik D, Vorlickova M. Circular dichroism and conformational polymorphism of DNA. *Nucleic acids research* 2009; 37:1713-25.
42. Randazzo A, Spada GP, da Silva MW. Circular dichroism of quadruplex structures. *Top Curr Chem* 2013; 330:67-86.
43. Kwok CK, Balasubramanian S. Targeted Detection of G-Quadruplexes in Cellular RNAs. *Angew Chem Int Ed Engl* 2015; 54:6751-4.
44. Haeusler AR, Donnelly CJ, Periz G, Simko EA, Shaw PG, Kim MS, et al. C9orf72 nucleotide repeat structures initiate molecular cascades of disease. *Nature* 2014; 507:195-200.

45. Beaudoin JD, Jodoin R, Perreault JP. In-line probing of RNA G-quadruplexes. *Methods* 2013; 64:79-87.
46. Sun D, Hurley LH. Biochemical techniques for the characterization of G-quadruplex structures: EMSA, DMS footprinting, and DNA polymerase stop assay. *Methods Mol Biol* 2010; 608:65-79.
47. Ehresmann C, Baudin F, Mougél M, Romby P, Ebel JP, Ehresmann B. Probing the structure of RNAs in solution. *Nucleic acids research* 1987; 15:9109-28.
48. Parkinson GN, Lee MP, Neidle S. Crystal structure of parallel quadruplexes from human telomeric DNA. *Nature* 2002; 417:876-80.
49. Webba da Silva M. NMR methods for studying quadruplex nucleic acids. *Methods* 2007; 43:264-77.
50. Mergny JL, Maurizot JC. Fluorescence resonance energy transfer as a probe for G-quartet formation by a telomeric repeat. *Chembiochem : a European journal of chemical biology* 2001; 2:124-32.
51. Patel DJ, Phan AT, Kuryavyi V. Human telomere, oncogenic promoter and 5'-UTR G-quadruplexes: diverse higher order DNA and RNA targets for cancer therapeutics. *Nucleic acids research* 2007; 35:7429-55.
52. Marchand A, Gabelica V. Native electrospray mass spectrometry of DNA G-quadruplexes in potassium solution. *Journal of the American Society for Mass Spectrometry* 2014; 25:1146-54.
53. Heck AJ. Native mass spectrometry: a bridge between interactomics and structural biology. *Nat Methods* 2008; 5:927-33.
54. Rosati S, Yang Y, Barendregt A, Heck AJ. Detailed mass analysis of structural heterogeneity in monoclonal antibodies using native mass spectrometry. *Nature protocols* 2014; 9:967-76.
55. Shah S, Friedman SH. An ESI-MS method for characterization of native and modified oligonucleotides used for RNA interference and other biological applications. *Nature protocols* 2008; 3:351-6.
56. Jaumot J, Gargallo R. Experimental methods for studying the interactions between G-quadruplex structures and ligands. *Current pharmaceutical design* 2012; 18:1900-16.
57. Murat P, Singh Y, Defrancq E. Methods for investigating G-quadruplex DNA/ligand interactions. *Chem Soc Rev* 2011; 40:5293-307.
58. Kang SG, Henderson E. Identification of non-telomeric G4-DNA binding proteins in human, E. coli, yeast, and Arabidopsis. *Molecules and cells* 2002; 14:404-10.
59. Sundquist WI, Heaphy S. Evidence for interstrand quadruplex formation in the dimerization of human immunodeficiency virus 1 genomic RNA. *Proceedings of the National Academy of Sciences of the United States of America* 1993; 90:3393-7.
60. Norseen J, Johnson FB, Lieberman PM. Role for G-quadruplex RNA binding by Epstein-Barr virus nuclear antigen 1 in DNA replication and metaphase chromosome attachment. *Journal of virology* 2009; 83:10336-46.
61. Tuesuwan B, Kern JT, Thomas PW, Rodriguez M, Li J, David WM, et al. Simian virus 40 large T-antigen G-quadruplex DNA helicase inhibition by G-quadruplex DNA-interactive agents. *Biochemistry* 2008; 47:1896-909.
62. Murat P, Balasubramanian S. Existence and consequences of G-quadruplex structures in DNA. *Current opinion in genetics & development* 2014; 25:22-9.
63. Bugaut A, Balasubramanian S. 5'-UTR RNA G-quadruplexes: translation regulation and targeting. *Nucleic acids research* 2012; 40:4727-41.
64. Kwok CK, Ding Y, Shahid S, Assmann SM, Bevilacqua PC. A stable RNA G-quadruplex within the 5'-UTR of Arabidopsis thaliana ATR mRNA inhibits translation. *The Biochemical journal* 2015; 467:91-102.
65. Gomez D, Guedin A, Mergny JL, Salles B, Riou JF, Teulade-Fichou MP, et al. A G-quadruplex structure within the 5'-UTR of TRF2 mRNA represses translation in human cells. *Nucleic acids research* 2010; 38:7187-98.
66. Shahid R, Bugaut A, Balasubramanian S. The BCL-2 5' untranslated region contains an RNA G-quadruplex-forming motif that modulates protein expression. *Biochemistry* 2010; 49:8300-6.

67. Agarwala P, Pandey S, Mapa K, Maiti S. The G-quadruplex augments translation in the 5' untranslated region of transforming growth factor beta2. *Biochemistry* 2013; 52:1528-38.
68. Beaudoin JD, Perreault JP. Exploring mRNA 3'-UTR G-quadruplexes: evidence of roles in both alternative polyadenylation and mRNA shortening. *Nucleic acids research* 2013; 41:5898-911.
69. Millevoi S, Moine H, Vagner S. G-quadruplexes in RNA biology. *Wiley interdisciplinary reviews RNA* 2012; 3:495-507.
70. Xu Y, Suzuki Y, Ito K, Komiyama M. Telomeric repeat-containing RNA structure in living cells. *Proceedings of the National Academy of Sciences of the United States of America* 2010; 107:14579-84.
71. Konig SL, Evans AC, Huppert JL. Seven essential questions on G-quadruplexes. *Biomolecular concepts* 2010; 1:197-213.
72. Huang WC, Tseng TY, Chen YT, Chang CC, Wang ZF, Wang CL, et al. Direct evidence of mitochondrial G-quadruplex DNA by using fluorescent anti-cancer agents. *Nucleic acids research* 2015; 43:10102-13.
73. Miyoshi D, Matsumura S, Nakano S, Sugimoto N. Duplex dissociation of telomere DNAs induced by molecular crowding. *Journal of the American Chemical Society* 2004; 126:165-9.
74. Schoeftner S, Blasco MA. Chromatin regulation and non-coding RNAs at mammalian telomeres. *Seminars in cell & developmental biology* 2010; 21:186-93.
75. Schaffitzel C, Berger I, Postberg J, Hanes J, Lipps HJ, Pluckthun A. In vitro generated antibodies specific for telomeric guanine-quadruplex DNA react with *Styloynchia lemnae* macronuclei. *Proceedings of the National Academy of Sciences of the United States of America* 2001; 98:8572-7.
76. Biffi G, Tannahill D, McCafferty J, Balasubramanian S. Quantitative visualization of DNA G-quadruplex structures in human cells. *Nature chemistry* 2013; 5:182-6.
77. Henderson A, Wu Y, Huang YC, Chavez EA, Platt J, Johnson FB, et al. Detection of G-quadruplex DNA in mammalian cells. *Nucleic acids research* 2014; 42:860-9.
78. Laguerre A, Hukezalie K, Winckler P, Katranji F, Chanteloup G, Pirrotta M, et al. Visualization of RNA-Quadruplexes in Live Cells. *Journal of the American Chemical Society* 2015; 137:8521-5.
79. Monchaud D, Teulade-Fichou MP. A hitchhiker's guide to G-quadruplex ligands. *Organic & biomolecular chemistry* 2008; 6:627-36.
80. Rodriguez R, Miller KM, Forment JV, Bradshaw CR, Nikan M, Britton S, et al. Small-molecule-induced DNA damage identifies alternative DNA structures in human genes. *Nature chemical biology* 2012; 8:301-10.
81. Cogo S, Xodo LE. G-quadruplex formation within the promoter of the KRAS proto-oncogene and its effect on transcription. *Nucleic acids research* 2006; 34:2536-49.
82. Morgan RK, Batra H, Gaerig VC, Hockings J, Brooks TA. Identification and characterization of a new G-quadruplex forming region within the kRAS promoter as a transcriptional regulator. *Biochimica et biophysica acta* 2015; 1859:235-45.
83. Siddiqui-Jain A, Grand CL, Bearss DJ, Hurley LH. Direct evidence for a G-quadruplex in a promoter region and its targeting with a small molecule to repress c-MYC transcription. *Proceedings of the National Academy of Sciences of the United States of America* 2002; 99:11593-8.
84. Yuan L, Tian T, Chen Y, Yan S, Xing X, Zhang Z, et al. Existence of G-quadruplex structures in promoter region of oncogenes confirmed by G-quadruplex DNA cross-linking strategy. *Scientific reports* 2013; 3:1811.
85. Tan J, Vonnrhein C, Smart OS, Bricogne G, Bollati M, Kusov Y, et al. The SARS-unique domain (SUD) of SARS coronavirus contains two macrodomains that bind G-quadruplexes. *PLoS pathogens* 2009; 5:e1000428.
86. Collie GW, Parkinson GN. The application of DNA and RNA G-quadruplexes to therapeutic medicines. *Chem Soc Rev* 2011; 40:5867-92.
87. Oganessian L, Bryan TM. Physiological relevance of telomeric G-quadruplex formation: a potential drug target. *BioEssays : news and reviews in molecular, cellular and developmental biology* 2007; 29:155-65.

88. Balasubramanian S, Hurley LH, Neidle S. Targeting G-quadruplexes in gene promoters: a novel anticancer strategy? *Nat Rev Drug Discov* 2011; 10:261-75.
89. Di Antonio M, Biffi G, Mariani A, Raiber EA, Rodriguez R, Balasubramanian S. Selective RNA versus DNA G-quadruplex targeting by in situ click chemistry. *Angew Chem Int Ed Engl* 2012; 51:11073-8.
90. Neidle S, Parkinson G. Telomere maintenance as a target for anticancer drug discovery. *Nat Rev Drug Discov* 2002; 1:383-93.
91. Mergny JL, Helene C. G-quadruplex DNA: a target for drug design. *Nat Med* 1998; 4:1366-7.
92. Blackburn EH. Telomeres: no end in sight. *Cell* 1994; 77:621-3.
93. Kim NW, Piatyszek MA, Prowse KR, Harley CB, West MD, Ho PL, et al. Specific association of human telomerase activity with immortal cells and cancer. *Science* 1994; 266:2011-5.
94. de Lange T. Activation of telomerase in a human tumor. *Proceedings of the National Academy of Sciences of the United States of America* 1994; 91:2882-5.
95. Sun D, Thompson B, Cathers BE, Salazar M, Kerwin SM, Trent JO, et al. Inhibition of human telomerase by a G-quadruplex-interactive compound. *Journal of medicinal chemistry* 1997; 40:2113-6.
96. Nasiri HR, Bell NM, McLuckie KI, Husby J, Abell C, Neidle S, et al. Targeting a c-MYC G-quadruplex DNA with a fragment library. *Chem Commun (Camb)* 2014; 50:1704-7.
97. Ou TM, Lu YJ, Zhang C, Huang ZS, Wang XD, Tan JH, et al. Stabilization of G-quadruplex DNA and down-regulation of oncogene c-myc by quindoline derivatives. *Journal of medicinal chemistry* 2007; 50:1465-74.
98. Brazda V, Haronikova L, Liao JC, Fojta M. DNA and RNA quadruplex-binding proteins. *Int J Mol Sci* 2014; 15:17493-517.
99. Ballal RD, Saha T, Fan S, Haddad BR, Rosen EM. BRCA1 localization to the telomere and its loss from the telomere in response to DNA damage. *The Journal of biological chemistry* 2009; 284:36083-98.
100. Zaug AJ, Podell ER, Cech TR. Human POT1 disrupts telomeric G-quadruplexes allowing telomerase extension in vitro. *Proceedings of the National Academy of Sciences of the United States of America* 2005; 102:10864-9.
101. Takahama K, Takada A, Tada S, Shimizu M, Sayama K, Kurokawa R, et al. Regulation of telomere length by G-quadruplex telomere DNA- and TERRA-binding protein TLS/FUS. *Chem Biol* 2013; 20:341-50.
102. Soldatenkov VA, Vetcher AA, Duka T, Ladame S. First evidence of a functional interaction between DNA quadruplexes and poly(ADP-ribose) polymerase-1. *ACS chemical biology* 2008; 3:214-9.
103. Chen S, Su L, Qiu J, Xiao N, Lin J, Tan JH, et al. Mechanistic studies for the role of cellular nucleic-acid-binding protein (CNBP) in regulation of c-myc transcription. *Biochimica et biophysica acta* 2013; 1830:4769-77.
104. Xiao J, McGown LB. Mass spectrometric determination of ILPR G-quadruplex binding sites in insulin and IGF-2. *Journal of the American Society for Mass Spectrometry* 2009; 20:1974-82.
105. Paramasivam M, Membrino A, Cogoi S, Fukuda H, Nakagama H, Xodo LE. Protein hnRNP A1 and its derivative Up1 unfold quadruplex DNA in the human KRAS promoter: implications for transcription. *Nucleic acids research* 2009; 37:2841-53.
106. Melko M, Douguet D, Bensaid M, Zongaro S, Verheggen C, Gecz J, et al. Functional characterization of the AFF (AF4/FMR2) family of RNA-binding proteins: insights into the molecular pathology of FRAXE intellectual disability. *Human molecular genetics* 2011; 20:1873-85.
107. von Hacht A, Seifert O, Menger M, Schutze T, Arora A, Konthur Z, et al. Identification and characterization of RNA guanine-quadruplex binding proteins. *Nucleic acids research* 2014; 42:6630-44.
108. Sun H, Karow JK, Hickson ID, Maizels N. The Bloom's syndrome helicase unwinds G4 DNA. *The Journal of biological chemistry* 1998; 273:27587-92.
109. Fry M, Loeb LA. Human werner syndrome DNA helicase unwinds tetrahelical structures of the fragile X syndrome repeat sequence d(CGG)n. *The Journal of biological chemistry* 1999; 274:12797-802.

110. Wu Y, Shin-ya K, Brosh RM, Jr. FANCD1 helicase defective in Fanconi anemia and breast cancer unwinds G-quadruplex DNA to defend genomic stability. *Molecular and cellular biology* 2008; 28:4116-28.
111. Schaeffer C, Bardoni B, Mandel JL, Ehresmann B, Ehresmann C, Moine H. The fragile X mental retardation protein binds specifically to its mRNA via a purine quartet motif. *Embo J* 2001; 20:4803-13.
112. Verheij C, Bakker CE, de Graaff E, Keulemans J, Willemsen R, Verkerk AJ, et al. Characterization and localization of the FMR-1 gene product associated with fragile X syndrome. *Nature* 1993; 363:722-4.
113. Verkerk AJ, Pieretti M, Sutcliffe JS, Fu YH, Kuhl DP, Pizzuti A, et al. Identification of a gene (FMR-1) containing a CGG repeat coincident with a breakpoint cluster region exhibiting length variation in fragile X syndrome. *Cell* 1991; 65:905-14.
114. Martin GM. Genetic syndromes in man with potential relevance to the pathobiology of aging. *Birth defects original article series* 1978; 14:5-39.
115. Ellis NA, German J. Molecular genetics of Bloom's syndrome. *Human molecular genetics* 1996; 5 Spec No:1457-63.
116. Johnson JE, Cao K, Ryvkin P, Wang LS, Johnson FB. Altered gene expression in the Werner and Bloom syndromes is associated with sequences having G-quadruplex forming potential. *Nucleic acids research* 2010; 38:1114-22.
117. Bole M, Menon L, Mihailescu MR. Fragile X mental retardation protein recognition of G quadruplex structure per se is sufficient for high affinity binding to RNA. *Molecular bioSystems* 2008; 4:1212-9.
118. Hanakahi LA, Sun H, Maizels N. High affinity interactions of nucleolin with G-G-paired rDNA. *The Journal of biological chemistry* 1999; 274:15908-12.
119. Takahama K, Miyawaki A, Shitara T, Mitsuya K, Morikawa M, Hagihara M, et al. G-Quadruplex DNA- and RNA-Specific-Binding Proteins Engineered from the RGG Domain of TLS/FUS. *ACS chemical biology* 2015; 10:2564-9.
120. Lupold SE, Hicke BJ, Lin Y, Coffey DS. Identification and characterization of nuclease-stabilized RNA molecules that bind human prostate cancer cells via the prostate-specific membrane antigen. *Cancer Research* 2002; 62:4029-33.
121. Holeman LA, Robinson SL, Szostak JW, Wilson C. Isolation and characterization of fluorophore-binding RNA aptamers. *Fold Des* 1998; 3:423-31.
122. Rajendran M, Ellington AD. Selection of fluorescent aptamer beacons that light up in the presence of zinc. *Anal Bioanal Chem* 2008; 390:1067-75.
123. Shangguan D, Li Y, Tang ZW, Cao ZHC, Chen HW, Mallikaratchy P, et al. Aptamers evolved from live cells as effective molecular probes for cancer study. *Proceedings of the National Academy of Sciences of the United States of America* 2006; 103:11838-43.
124. Ellington AD, Szostak JW. In vitro selection of RNA molecules that bind specific ligands. *Nature* 1990; 346:818-22.
125. Tuerk C, Gold L. Systematic evolution of ligands by exponential enrichment: RNA ligands to bacteriophage T4 DNA polymerase. *Science* 1990; 249:505-10.
126. Cho EJ, Lee JW, Ellington AD. Applications of aptamers as sensors. *Annu Rev Anal Chem (Palo Alto Calif)* 2009; 2:241-64.
127. Levy-Nissenbaum E, Radovic-Moreno AF, Wang AZ, Langer R, Farokhzad OC. Nanotechnology and aptamers: applications in drug delivery. *Trends in biotechnology* 2008; 26:442-9.
128. Keefe AD, Pai S, Ellington A. Aptamers as therapeutics. *Nature Reviews Drug Discovery* 2010; 9:537-50.
129. Foy JWD, Rittenhouse K, Modi M, Patel M. Local tolerance and systemic safety of pegaptanib sodium in the dog and rabbit. *J Ocul Pharmacol Th* 2007; 23:452-66.
130. Preclinical and phase 1A clinical evaluation of an anti-VEGF pegylated aptamer (EYE001) for the treatment of exudative age-related macular degeneration. *Retina* 2002; 22:143-52.
131. Kruspe S, Mittelberger F, Szameit K, Hahn U. Aptamers as drug delivery vehicles. *ChemMedChem* 2014; 9:1998-2011.

132. Mayer G, Ahmed MSL, Dolf A, Endl E, Knolle PA, Famulok M. Fluorescence-activated cell sorting for aptamer SELEX with cell mixtures. *Nature protocols* 2010; 5:1993-2004.
133. Tolle F, Mayer G. Dressed for success - applying chemistry to modulate aptamer functionality. *Chem Sci* 2013; 4:60-7.
134. Thiel KW, Giangrande PH. Intracellular delivery of RNA-based therapeutics using aptamers. *Therapeutic delivery* 2010; 1:849-61.
135. Guo KT, Paul A, Schichor C, Ziemer G, Wendel HP. Cell-SELEX: Novel perspectives of aptamer-based therapeutics. *Int J Mol Sci* 2008; 9:668-78.
136. Dirkwager RM, Kinghorn AB, Richards JS, Tanner JA. APTEC: aptamer-tethered enzyme capture as a novel rapid diagnostic test for malaria. *Chem Commun (Camb)* 2015; 51:4697-700.
137. Missailidis S, Hardy A. Aptamers as inhibitors of target proteins. *Expert Opin Ther Pat* 2009; 19:1073-82.
138. Bock LC, Griffin LC, Latham JA, Vermaas EH, Toole JJ. Selection of single-stranded DNA molecules that bind and inhibit human thrombin. *Nature* 1992; 355:564-6.
139. Ng EW, Shima DT, Calias P, Cunningham ET, Jr., Guyer DR, Adamis AP. Pegaptanib, a targeted anti-VEGF aptamer for ocular vascular disease. *Nat Rev Drug Discov* 2006; 5:123-32.
140. Xiang D, Shigdar S, Qiao G, Wang T, Kouzani AZ, Zhou SF, et al. Nucleic acid aptamer-guided cancer therapeutics and diagnostics: the next generation of cancer medicine. *Theranostics* 2015; 5:23-42.
141. Rosenberg JE, Bambury RM, Van Allen EM, Drabkin HA, Lara PN, Harzstark AL, et al. A phase II trial of AS1411 (a novel nucleolin-targeted DNA aptamer) in metastatic renal cell carcinoma. *Investigational new drugs* 2014; 32:178-87.
142. Chu TC, Twu KY, Ellington AD, Levy M. Aptamer mediated siRNA delivery. *Nucleic acids research* 2006; 34:e73.
143. Wu X, Ding B, Gao J, Wang H, Fan W, Wang X, et al. Second-generation aptamer-conjugated PSMA-targeted delivery system for prostate cancer therapy. *International journal of nanomedicine* 2011; 6:1747-56.
144. Jacobson O, Weiss ID, Wang L, Wang Z, Yang X, Dewhurst A, et al. 18F-Labeled Single-Stranded DNA Aptamer for PET Imaging of Protein Tyrosine Kinase-7 Expression. *Journal of nuclear medicine : official publication, Society of Nuclear Medicine* 2015; 56:1780-5.
145. Ray P, Cheek MA, Sharaf ML, Li N, Ellington AD, Sullenger BA, et al. Aptamer-mediated delivery of chemotherapy to pancreatic cancer cells. *Nucleic acid therapeutics* 2012; 22:295-305.
146. Li N, Larson T, Nguyen HH, Sokolov KV, Ellington AD. Directed evolution of gold nanoparticle delivery to cells. *Chem Commun (Camb)* 2010; 46:392-4.
147. Leaderer D, Cashman SM, Kumar-Singh R. Topical application of a G-Quartet aptamer targeting nucleolin attenuates choroidal neovascularization in a model of age-related macular degeneration. *Experimental eye research* 2015; 140:171-8.
148. Shieh YA, Yang SJ, Wei MF, Shieh MJ. Aptamer-based tumor-targeted drug delivery for photodynamic therapy. *ACS nano* 2010; 4:1433-42.
149. Wilner SE, Wengerter B, Maier K, de Lourdes Borba Magalhaes M, Del Amo DS, Pai S, et al. An RNA alternative to human transferrin: a new tool for targeting human cells. *Molecular therapy Nucleic acids* 2012; 1:e21.
150. Zhang MZ, Yu RN, Chen J, Ma ZY, Zhao YD. Targeted quantum dots fluorescence probes functionalized with aptamer and peptide for transferrin receptor on tumor cells. *Nanotechnology* 2012; 23:485104.
151. Dai F, Zhang Y, Zhu X, Shan N, Chen Y. The anti-chemoresistant effect and mechanism of MUC1 aptamer-miR-29b chimera in ovarian cancer. *Gynecologic oncology* 2013; 131:451-9.
152. Chen H, Zhao J, Zhang M, Yang H, Ma Y, Gu Y. MUC1 aptamer-based near-infrared fluorescence probes for tumor imaging. *Molecular imaging and biology : MIB : the official publication of the Academy of Molecular Imaging* 2015; 17:38-48.
153. Subramanian N, Kanwar JR, Athalya PK, Janakiraman N, Khetan V, Kanwar RK, et al. EpCAM aptamer mediated cancer cell specific delivery of EpCAM siRNA using polymeric nanocomplex. *Journal of biomedical science* 2015; 22:4.

154. Zhou J, Li H, Li S, Zaia J, Rossi JJ. Novel dual inhibitory function aptamer-siRNA delivery system for HIV-1 therapy. *Mol Ther* 2008; 16:1481-9.
155. Lopes de Campos WR, Chirwa N, London G, Rotherham LS, Morris L, Mayosi BM, et al. HIV-1 subtype C unproductively infects human cardiomyocytes in vitro and induces apoptosis mitigated by an anti-Gp120 aptamer. *PLoS One* 2014; 9:e110930.
156. Galmarini CM, Mackey JR, Dumontet C. Nucleoside analogues and nucleobases in cancer treatment. *The Lancet Oncology* 2002; 3:415-24.
157. Burris HA, 3rd, Moore MJ, Andersen J, Green MR, Rothenberg ML, Modiano MR, et al. Improvements in survival and clinical benefit with gemcitabine as first-line therapy for patients with advanced pancreas cancer: a randomized trial. *Journal of clinical oncology : official journal of the American Society of Clinical Oncology* 1997; 15:2403-13.
158. Gyllensvärd A. Phase III Studie: Gemcitabin, 5-FU, Folinsäure vs. Gemcitabin allein in der Therapie des fortgeschrittenen, inoperablen Pankreaskarzinom –Endauswertung. Universität Berlin. 2008.
159. Malet-Martino M, Jolimaitre P, Martino R. The prodrugs of 5-fluorouracil. *Current medicinal chemistry Anti-cancer agents* 2002; 2:267-310.
160. Maybaum J, Ullman B, Mandel HG, Day JL, Sadee W. Regulation of RNA- and DNA-directed actions of 5-fluoropyrimidines in mouse T-lymphoma (S-49) cells. *Cancer Res* 1980; 40:4209-15.
161. Kunz C, Focke F, Saito Y, Schuermann D, Lettieri T, Selfridge J, et al. Base excision by thymine DNA glycosylase mediates DNA-directed cytotoxicity of 5-fluorouracil. *PLoS Biol* 2009; 7:e91.
162. Gmeiner WH. Novel chemical strategies for thymidylate synthase inhibition. *Current medicinal chemistry* 2005; 12:191-202.
163. Kruspe S, Hahn U. An Aptamer Intrinsically Comprising 5-Fluoro-2'-deoxyuridine for Targeted Chemotherapy. *Angew Chem Int Ed Engl* 2014; 53:10541-4.
164. Huang P, Chubb S, Hertel LW, Grindey GB, Plunkett W. Action of 2',2'-Difluorodeoxycytidine on DNA-Synthesis. *Cancer Res* 1991; 51:6110-7.
165. Huang P, Plunkett W. Induction of Apoptosis by Gemcitabine. *Semin Oncol* 1995; 22:19-25.
166. Galmarini CM, Mackey JR, Dumontet C. Nucleoside analogues: mechanisms of drug resistance and reversal strategies. *Leukemia* 2001; 15:875-90.
167. Plunkett W, Huang P, Gandhi V. Preclinical characteristics of gemcitabine. *Anti-cancer drugs* 1995; 6 Suppl 6:7-13.
168. Vanhaperen VWTR, Veerman G, Vermorken JB, Peters GJ. 2',2'-Difluoro-Deoxycytidine (Gemcitabine) Incorporation into Rna and DNA of Tumor-Cell Lines. *Biochemical pharmacology* 1993; 46:762-6.
169. Shi Z, Azuma A, Sampath D, Li YX, Huang P, Plunkett W. S-Phase arrest by nucleoside analogues and abrogation of survival without cell cycle progression by 7-hydroxystaurosporine. *Cancer Res* 2001; 61:1065-72.
170. Tsujie M, Nakamori S, Nakahira S, Takahashi Y, Hayashi N, Okami J, et al. Human equilibrative nucleoside transporter 1, as a predictor of 5-fluorouracil resistance in human pancreatic cancer. *Anticancer Res* 2007; 27:2241-9.
171. Spratlin J, Sangha R, Glubrecht D, Dabbagh L, Young JD, Dumontet C, et al. The absence of human equilibrative nucleoside transporter 1 is associated with reduced survival in patients with gemcitabine-treated pancreas adenocarcinoma. *Clinical cancer research : an official journal of the American Association for Cancer Research* 2004; 10:6956-61.
172. Xu ZW, Friess H, Buchler MW, Solioz M. Overexpression of Bax sensitizes human pancreatic cancer cells to apoptosis induced by chemotherapeutic agents. *Cancer Chemother Pharmacol* 2002; 49:504-10.
173. Xu Z, Friess H, Solioz M, Aebi S, Korc M, Kleeff J, et al. Bcl-x(L) antisense oligonucleotides induce apoptosis and increase sensitivity of pancreatic cancer cells to gemcitabine. *International journal of cancer Journal international du cancer* 2001; 94:268-74.
174. Shi X, Liu S, Kleeff J, Friess H, Buchler MW. Acquired resistance of pancreatic cancer cells towards 5-Fluorouracil and gemcitabine is associated with altered expression of apoptosis-regulating genes. *Oncology* 2002; 62:354-62.

175. Tsujie M, Nakamori S, Nakahira S, Takeda S, Takahashi Y, Hayashi N, et al. Schedule-dependent therapeutic effects of gemcitabine combined with uracil-tegafur in a human pancreatic cancer xenograft model. *Pancreas* 2006; 33:142-7.
176. Doherty GJ, McMahon HT. Mechanisms of endocytosis. *Annual review of biochemistry* 2009; 78:857-902.
177. Kotula JW, Pratico ED, Ming X, Nakagawa O, Juliano RL, Sullenger BA. Aptamer-mediated delivery of splice-switching oligonucleotides to the nuclei of cancer cells. *Nucleic acid therapeutics* 2012; 22:187-95.
178. van Dam EM, Ten Broeke T, Jansen K, Spijkers P, Stoorvogel W. Endocytosed transferrin receptors recycle via distinct dynamin and phosphatidylinositol 3-kinase-dependent pathways. *The Journal of biological chemistry* 2002; 277:48876-83.
179. Goodman OB, Jr., Barwe SP, Ritter B, McPherson PS, Vasko AJ, Keen JH, et al. Interaction of prostate specific membrane antigen with clathrin and the adaptor protein complex-2. *International journal of oncology* 2007; 31:1199-203.
180. Gorden P, Carpentier JL, Cohen S, Orci L. Epidermal growth factor: morphological demonstration of binding, internalization, and lysosomal association in human fibroblasts. *Proceedings of the National Academy of Sciences of the United States of America* 1978; 75:5025-9.
181. Hanover JA, Willingham MC, Pastan I. Kinetics of transit of transferrin and epidermal growth factor through clathrin-coated membranes. *Cell* 1984; 39:283-93.
182. Iacopetta BJ, Rothenberger S, Kuhn LC. A role for the cytoplasmic domain in transferrin receptor sorting and coated pit formation during endocytosis. *Cell* 1988; 54:485-9.
183. Traub LM. Tickets to ride: selecting cargo for clathrin-regulated internalization. *Nature reviews Molecular cell biology* 2009; 10:583-96.
184. Sorkin A, von Zastrow M. Endocytosis and signalling: intertwining molecular networks. *Nature reviews Molecular cell biology* 2009; 10:609-22.
185. Liu HY, Gao X. A universal protein tag for delivery of SiRNA-aptamer chimeras. *Scientific reports* 2013; 3:3129.
186. Mellman I, Fuchs R, Helenius A. Acidification of the endocytic and exocytic pathways. *Annual review of biochemistry* 1986; 55:663-700.
187. Verma UN, van den Blink B, Pillai R, Chawla J, Mazumder A, Herscovitz HB, et al. Paclitaxel vs cyclophosphamide in peripheral blood stem cell mobilization: comparative studies in a murine model. *Experimental hematology* 1999; 27:553-60.
188. Kichler A, Mason AJ, Bechinger B. Cationic amphipathic histidine-rich peptides for gene delivery. *Biochimica et biophysica acta* 2006; 1758:301-7.
189. Berg K, Selbo PK, Prasmickaite L, Tjelle TE, Sandvig K, Moan J, et al. Photochemical internalization: a novel technology for delivery of macromolecules into cytosol. *Cancer Res* 1999; 59:1180-3.
190. Meyer C. Interleukin-6-Rezeptor spezifische RNA-Aptamere. Dissertation. University of Hamburg. 2009.
191. Meyer C, Eydeler K, Magbanua E, Zivkovic T, Piganeau N, Lorenzen I, et al. Interleukin-6 receptor specific RNA aptamers for cargo delivery into target cells. *RNA biology* 2012; 9:67-80.
192. Zuker M. Mfold web server for nucleic acid folding and hybridization prediction. *Nucleic acids research* 2003; 31:3406-15.
193. Nishimoto N, Kishimoto T. Interleukin 6: from bench to bedside. *Nature clinical practice Rheumatology* 2006; 2:619-26.
194. Rincon M. Interleukin-6: from an inflammatory marker to a target for inflammatory diseases. *Trends in immunology* 2012; 33:571-7.
195. Vollmer P, Oppmann B, Voltz N, Fischer M, Rose-John S. A role for the immunoglobulin-like domain of the human IL-6 receptor. *Intracellular protein transport and shedding. European journal of biochemistry / FEBS* 1999; 263:438-46.
196. Varghese JN, Moritz RL, Lou MZ, Van Donkelaar A, Ji H, Ivancic N, et al. Structure of the extracellular domains of the human interleukin-6 receptor alpha -chain. *Proceedings of the National Academy of Sciences of the United States of America* 2002; 99:15959-64.

197. Kruspe S. Aptamervermittelter Wirkstofftransport. Dissertation. University of Hamburg. 2014.
198. Silver JS, Hunter CA. gp130 at the nexus of inflammation, autoimmunity, and cancer. *Journal of leukocyte biology* 2010; 88:1145-56.
199. Heinrich PC, Behrmann I, Haan S, Hermanns HM, Muller-Newen G, Schaper F. Principles of interleukin (IL)-6-type cytokine signalling and its regulation. *The Biochemical journal* 2003; 374:1-20.
200. Garbers C, Janner N, Chalaris A, Moss ML, Floss DM, Meyer D, et al. Species specificity of ADAM10 and ADAM17 proteins in interleukin-6 (IL-6) trans-signaling and novel role of ADAM10 in inducible IL-6 receptor shedding. *The Journal of biological chemistry* 2011; 286:14804-11.
201. Jones SA, Horiuchi S, Topley N, Yamamoto N, Fuller GM. The soluble interleukin 6 receptor: mechanisms of production and implications in disease. *FASEB J* 2001; 15:43-58.
202. Fischer M, Goldschmitt J, Peschel C, Brakenhoff JP, Kallen KJ, Wollmer A, et al. I. A bioactive designer cytokine for human hematopoietic progenitor cell expansion. *Nat Biotechnol* 1997; 15:142-5.
203. Ataie-Kachoeie P, Pourgholami MH, Morris DL. Inhibition of the IL-6 signaling pathway: a strategy to combat chronic inflammatory diseases and cancer. *Cytokine & growth factor reviews* 2013; 24:163-73.
204. Kishimoto T. Factors affecting B-cell growth and differentiation. *Annual review of immunology* 1985; 3:133-57.
205. Tanaka T, Narazaki M, Kishimoto T. IL-6 in inflammation, immunity, and disease. *Cold Spring Harbor perspectives in biology* 2014; 6:a016295.
206. Carbone G, Wilson A, Diehl SA, Bunn J, Cooper SM, Rincon M. Interleukin-6 receptor blockade selectively reduces IL-21 production by CD4 T cells and IgG4 autoantibodies in rheumatoid arthritis. *International journal of biological sciences* 2013; 9:279-88.
207. van Rhee F, Wong RS, Munshi N, Rossi JF, Ke XY, Fossa A, et al. Siltuximab for multicentric Castleman's disease: a randomised, double-blind, placebo-controlled trial. *The Lancet Oncology* 2014; 15:966-74.
208. Gupta S, Hirota M, Waugh SM, Murakami I, Suzuki T, Muraguchi M, et al. Chemically modified DNA aptamers bind interleukin-6 with high affinity and inhibit signaling by blocking its interaction with interleukin-6 receptor. *The Journal of biological chemistry* 2014; 289:8706-19.
209. Mittelberger F, Meyer C, Waetzig GH, Zacharias M, Valentini E, Svergun DI, et al. RAID3 - An interleukin-6 receptor-binding aptamer with post-selective modification-resistant affinity. *RNA biology* 2015; 12:1043-53.
210. Magbanua E, Zivkovic T, Hansen B, Beschorner N, Meyer C, Lorenzen I, et al. d(GGGT)(4) and r(GGGU)(4) are both HIV-1 inhibitors and interleukin-6 receptor aptamers. *RNA biology* 2013; 10:216-27.
211. Eydeler K. Charakterisierung von RNA-Aptameren mit Spezifität für den humanen Interleukin-6-Rezeptor. Dissertation. University of Hamburg. 2011.
212. Kruspe S, Meyer C, Hahn U. Chlorin e6 Conjugated Interleukin-6 Receptor Aptamers Selectively Kill Target Cells Upon Irradiation. *Molecular therapy Nucleic acids* 2014; 3:e143.
213. Bates PJ, Kahlon JB, Thomas SD, Trent JO, Miller DM. Antiproliferative activity of G-rich oligonucleotides correlates with protein binding. *The Journal of biological chemistry* 1999; 274:26369-77.
214. Mukundan VT, Do NQ, Phan AT. HIV-1 integrase inhibitor T30177 forms a stacked dimeric G-quadruplex structure containing bulges. *Nucleic acids research* 2011; 39:8984-91.
215. Olsthoorn RC. G-quadruplexes within prion mRNA: the missing link in prion disease? *Nucleic acids research* 2014; 42:9327-33.
216. Proske D, Gilch S, Wopfner F, Schatzl HM, Winnacker EL, Famulok M. Prion-protein-specific aptamer reduces PrP^{Sc} formation. *Chembiochem : a European journal of chemical biology* 2002; 3:717-25.
217. Mashima T, Nishikawa F, Kamatari YO, Fujiwara H, Saimura M, Nagata T, et al. Anti-prion activity of an RNA aptamer and its structural basis. *Nucleic acids research* 2013; 41:1355-62.

218. Shum KT, Tanner JA. Differential inhibitory activities and stabilisation of DNA aptamers against the SARS coronavirus helicase. *Chembiochem : a European journal of chemical biology* 2008; 9:3037-45.
219. Huang H, Suslov NB, Li NS, Shelke SA, Evans ME, Koldobskaya Y, et al. A G-quadruplex-containing RNA activates fluorescence in a GFP-like fluorophore. *Nature chemical biology* 2014; 10:686-91.
220. Zhu L, Li C, Zhu Z, Liu D, Zou Y, Wang C, et al. In vitro selection of highly efficient G-quadruplex-based DNAzymes. *Anal Chem* 2012; 84:8383-90.
221. Magbanua E, Zivkovic T, Hansen B, Beschorner N, Meyer C, Lorenzen I, et al. d(GGGT) 4 and r(GGGU) 4 are both HIV-1 inhibitors and interleukin-6 receptor aptamers. *RNA biology* 2013; 10:216-27.
222. Onyshchenko MI, Gaynutdinov TI, Englund EA, Appella DH, Neumann RD, Panyutin IG. Stabilization of G-quadruplex in the BCL2 promoter region in double-stranded DNA by invading short PNAs. *Nucleic acids research* 2009; 37:7570-80.
223. Fiset JF, Montagna DR, Mihailescu MR, Wolfe MS. A G-rich element forms a G-quadruplex and regulates BACE1 mRNA alternative splicing. *Journal of neurochemistry* 2012; 121:763-73.
224. Biffi G, Tannahill D, Balasubramanian S. An intramolecular G-quadruplex structure is required for binding of telomeric repeat-containing RNA to the telomeric protein TRF2. *Journal of the American Chemical Society* 2012; 134:11974-6.
225. Hirashima K, Seimiya H. Telomeric repeat-containing RNA/G-quadruplex-forming sequences cause genome-wide alteration of gene expression in human cancer cells in vivo. *Nucleic acids research* 2015; 43:2022-32.
226. Meyer C, Berg K, Eydeler-Haeder K, Lorenzen I, Grotzinger J, Rose-John S, et al. Stabilized Interleukin-6 receptor binding RNA aptamers. *RNA biology* 2014; 11:57-65.
227. Kankia BI, Marky LA. Folding of the thrombin aptamer into a G-quadruplex with Sr(2+): stability, heat, and hydration. *Journal of the American Chemical Society* 2001; 123:10799-804.
228. Shangguan D, Cao Z, Meng L, Mallikaratchy P, Sefah K, Wang H, et al. Cell-specific aptamer probes for membrane protein elucidation in cancer cells. *J Proteome Res* 2008; 7:2133-9.
229. Mullen MA, Assmann SM, Bevilacqua PC. Toward a digital gene response: RNA G-quadruplexes with fewer quartets fold with higher cooperativity. *Journal of the American Chemical Society* 2012; 134:812-5.
230. Piekna-Przybylska D, Sullivan MA, Sharma G, Bambara RA. U3 region in the HIV-1 genome adopts a G-quadruplex structure in its RNA and DNA sequence. *Biochemistry* 2014; 53:2581-93.
231. Roch AM, Panaye G, Michal Y, Quash G. Methional, a cellular metabolite, induces apoptosis preferentially in G2/M-synchronized BAF3 murine lymphoid cells. *Cytometry* 1998; 31:10-9.
232. Meyer C, Eydeler K, Magbanua E, Zivkovic T, Piganeau N, Lorenzen I, et al. Interleukin-6 receptor specific RNA aptamers for cargo delivery into target cells. *RNA biology* 2012; 9:67-80.
233. Kikin O, D'Antonio L, Bagga PS. QGRS Mapper: a web-based server for predicting G-quadruplexes in nucleotide sequences. *Nucleic acids research* 2006; 34:W676-82.
234. Hodge LS, Taub ME, Tracy TS. The deaminated metabolite of gemcitabine, 2',2'-difluorodeoxyuridine, modulates the rate of gemcitabine transport and intracellular phosphorylation via deoxycytidine kinase. *Drug metabolism and disposition: the biological fate of chemicals* 2011; 39:2013-6.
235. Cappella P, Tomasoni D, Faretta M, Lupi M, Montalenti F, Viale F, et al. Cell cycle effects of gemcitabine. *International journal of cancer Journal international du cancer* 2001; 93:401-8.
236. Tasset DM, Kubik MF, Steiner W. Oligonucleotide inhibitors of human thrombin that bind distinct epitopes. *Journal of molecular biology* 1997; 272:688-98.
237. Castello A, Fischer B, Eichelbaum K, Horos R, Beckmann BM, Strein C, et al. Insights into RNA Biology from an Atlas of Mammalian mRNA-Binding Proteins. *Cell* 2012; 149:1393-406.
238. Zohlnhofer D, Graeve L, Rose-John S, Schooltink H, Dittrich E, Heinrich PC. The hepatic interleukin-6 receptor. Down-regulation of the interleukin-6 binding subunit (gp80) by its ligand. *FEBS letters* 1992; 306:219-22.

239. Simonsson T. G-quadruplex DNA structures--variations on a theme. *Biol Chem* 2001; 382:621-8.
240. Pandey S, Agarwala P, Maiti S. Effect of loops and G-quartets on the stability of RNA G-quadruplexes. *The journal of physical chemistry B* 2013; 117:6896-905.
241. Kocman V, Plavec J. A tetrahelical DNA fold adopted by tandem repeats of alternating GGG and GCG tracts. *Nature communications* 2014; 5:5831.
242. Hud NV, Schultze P, Sklenar V, Feigon J. Binding sites and dynamics of ammonium ions in a telomere repeat DNA quadruplex. *Journal of molecular biology* 1999; 285:233-43.
243. Russo Krauss I, Merlino A, Vergara A, Sica F. An overview of biological macromolecule crystallization. *Int J Mol Sci* 2013; 14:11643-91.
244. Tucker WO, Shum KT, Tanner JA. G-quadruplex DNA Aptamers and their Ligands: Structure, Function and Application. *Current pharmaceutical design* 2012; 18:2014-26.
245. Otto S. Charakterisierung der Bindungsfläche zwischen dem Aptamer AIR-3/3A und dem humanen Interleukin-6-Rezeptor. Master's Thesis. University of Hamburg. 2015.
246. Lozano GM, Bejarano I, Espino J, Gonzalez D, Ortiz A, Garcia JF, et al. Relationship between Caspase Activity and Apoptotic Markers in Human Sperm in Response to Hydrogen Peroxide and Progesterone. *J Reprod Develop* 2009; 55:615-21.
247. Negoescu A, Lorimier P, LabatMoleur F, Drouet C, Robert C, Guillermet C, et al. In situ apoptotic cell labeling by the TUNEL method: Improvement and evaluation on cell preparations. *J Histochem Cytochem* 1996; 44:959-68.
248. Negoescu A, Guillermet C, Lorimier P, Brambilla E, Labat-Moleur F. Importance of DNA fragmentation in apoptosis with regard to TUNEL specificity. *Biomed Pharmacother* 1998; 52:252-8.
249. Li T, Shi L, Wang E, Dong S. Multifunctional G-quadruplex aptamers and their application to protein detection. *Chemistry* 2009; 15:1036-42.
250. Wilkinson KA, Merino EJ, Weeks KM. Selective 2'-hydroxyl acylation analyzed by primer extension (SHAPE): quantitative RNA structure analysis at single nucleotide resolution. *Nature protocols* 2006; 1:1610-6.
251. Gopinath SC. Mapping of RNA-protein interactions. *Analytica chimica acta* 2009; 636:117-28.
252. Fourmy D, Yoshizawa S. Protein-RNA footprinting: an evolving tool. *Wiley interdisciplinary reviews RNA* 2012; 3:557-66.
253. Bley CJ, Qi X, Rand DP, Borges CR, Nelson RW, Chen JJ. RNA-protein binding interface in the telomerase ribonucleoprotein. *Proceedings of the National Academy of Sciences of the United States of America* 2011; 108:20333-8.
254. Christian H, Hofele RV, Urlaub H, Ficner R. Insights into the activation of the helicase Prp43 by biochemical studies and structural mass spectrometry. *Nucleic acids research* 2014; 42:1162-79.
255. Meisenheimer KM, Koch TH. Photocross-linking of nucleic acids to associated proteins. *Crit Rev Biochem Mol* 1997; 32:101-40.
256. Keskin S, Besztejan S, Kassier G, Manz S, Bucker R, Riekeberg S, et al. Visualization of Multimerization and Self-Assembly of DNA-Functionalized Gold Nanoparticles Using In-Liquid Transmission Electron Microscopy. *The journal of physical chemistry letters* 2015; 6:4487-92.
257. Thiel WH, Bair T, Peek AS, Liu X, Dassie J, Stockdale KR, et al. Rapid identification of cell-specific, internalizing RNA aptamers with bioinformatics analyses of a cell-based aptamer selection. *Plos One* 2012; 7:e43836.
258. Jiang F, Liu B, Lu J, Li F, Li D, Liang C, et al. Progress and Challenges in Developing Aptamer-Functionalized Targeted Drug Delivery Systems. *Int J Mol Sci* 2015; 16:23784-822.
259. Živković T. Interleukin-6-Rezeptor-spezifische DNA-Aptamere. University of Hamburg. 2010.

9. Acknowledgments

I wish to thank Professor Dr. Ulrich Hahn for providing this project and supervising my work throughout the last years. Uli, I am grateful for the possibility to independently organize my research in your lab and all the positive remarks and support I received from you that helped me grow as a research scientist! Also, I thank Prof. Dr. Zoya Ignatova for being so kind as to agree reviewing this thesis! Thanks to the members of my examination commission for their support toward the success of this final step of my doctorate! Thank is also due to my co supervisor Prof. R. G. Dwayne Miller whose enthusiasm, continuous encouragement and helpful support I gratefully acknowledge!

A huge THANK YOU to my fabulous working group uniting heroes, princesses, angels, EtOH addicts and lots of wit, wisdom and inventiveness! Of course, also neighboring clans are acknowledged for good manners, great beer, lots of fun and enriching scientific exchange. Special thanks to: Katrin for carefully proofreading what I have written, being endlessly patient and positive, helping me to improve, to Kati for always being there when help or advice was needed during the years as well as for spontaneous proofreading and helpful comments, to Asia for agitating for minority rights and cheerful colors in our lab (and for being a lovely person). Thanks to Eileen, continuous positive, helpful and funny member of the Hahn lab. Thanks to Sarah, Tatjana, Marge and Elena for exceptional technical assistance, and Danny, Marcia, Julia, Sonia and Anja for administrative support! Thanks to all whose names are not listed here but who contributed to this work before and with me. I gratefully acknowledge funding through the International Max Planck Research School for Ultrafast Imaging & Structural Dynamics and the exchange with my fellows from grad school of whom I'd like to mention Elke, Steph, Alessandra and Sercan.

Thanks to all my collaborators for prosperous cooperation: Lirong He and Patrick Théato (TMC UHH), Marcel Kwiatkowski, Sönke Harder, Hartmut Schlüter (Core Facility Mass Spectrometric Proteomics, UKE Hamburg), Boris Krichel, Charlotte Uetrecht (HPI, Leibniz Institute for Experimental Virology, Hamburg), Erica Valentini and Dmitri Svergun (EMBL Hamburg) and Martin Zacharias (Biomolecular Dynamics, TU Munich). Thanks also to David Monchaud for helpful discussions, Aude Hallenbach and all my other practical students for their productive help!

Thanks to all my friends, for the time off aboard the #homeoffice, for every tapir_(TOY) in sight, thanks to coffee, tea, chocolate, books and music.

Lastly, I wish to express my deepest gratitude to those who made it possible to get this far: Amélie, who deserves a title herself for accepting my dedication to this project, my family for providing me with unconditional love, support and the essentials needed to grow into what I am today, Sven for supporting, caring and standing by me despite of myself and of course, my very special friend Philine!

10. Appendices

10.1. GHS hazard statements

Table 27: Hazard statements according to GHS.

code	statement
H225	Highly flammable liquid and vapour.
H226	Flammable liquid and vapour.
H301	Toxic if swallowed.
H302	Harmful if swallowed
H303	Maybe harmful if swallowed.
H312	Harmful in contact with skin.
H314	Causes severe skin burns and eye damage.
H315	Causes skin irritation.
H317	May cause an allergic skin reaction.
H319	Causes serious eye irritation.
H331	Toxic if inhaled.
H332	Harmful if inhaled.
H334	May cause allergy or asthma symptoms or breathing difficulties if inhaled.
H335	May cause respiratory irritation.
H340	May cause genetic defects.
H341	Suspected of causing genetic defects.
H350	May cause cancer.
H351	Suspected of causing cancer.
H360	May damage fertility or the unborn child.
H361	Suspected of damaging fertility or the unborn child.
H372	Causes damage to (affected) organs through prolonged or repeated exposure.
H411	Toxic to aquatic life with long lasting effects.

10.2. GHS precautionary statements

Table 28: Precautionary statements according to GHS.

code	statement
P201	Obtain special instructions before use.
P202	Do not handle until all safety precautions have been read and understood.
P210	Keep away from heat/sparks/open flames/hot surfaces. - No smoking.
P261	Avoid breathing dust/fumes/gas/mist/vapours/spray.
P264	Wash ... thoroughly after handling.
P270	Do not eat, drink or smoke when using this product.
P280	Wear protective gloves/protective clothing/eye protection/face protection.
P281	Use personal protective equipment as required.
P301	IF SWALLOWED:
P302	IF ON SKIN:
P304	IF INHALED:
P305	IF IN EYES:
P307	IF ON CLOTHING
P308	IF exposed or concerned:
P310	Immediately call a POISON CENTER or doctor/physician.
P311	Call a POISON CENTER or doctor/physician.
P312	Call a POISON CENTER or doctor/physician if you feel unwell.
P313	Get medical advice/attention.
P330	Rinse mouth.
P331	Do NOT induce vomiting.
P337	If eye irritation persists, ...
P338	Remove contact lenses if present and easy to do. Continue rinsing.
P341	If breathing is difficult, remove victim to fresh air and keep at rest in a position comfortable for breathing.
P342	If experiencing respiratory symptoms:
P351	Rinse cautiously with water for several minutes.
P352	Wash with plenty of soap and water.
P405	Store locked up.
P501	Dispose of contents/container in accordance with local/regional/national/international regulation

10.3. Hazardous compounds according to GHS

Compounds used and their hazardous categorization according to the Globally Harmonized System of Classification and Labeling of Chemicals (GHS) are given in Table 29.

Table 29: List of hazardous compounds.

compound	GHS label	H-statements	P-statements
5-Fluoro-2'-deoxyuridine	GHS06, GHS08	H301, H315, H319, H341	P201, P202, P264, P270, P280 P301+P310
Gemcitabine	GHS07, GHS08, GHS09	H302, H312, H315, H319, H340, H351, H360, H372, H411	P264, P280, P201, P202, P281, P260, P273 P362+P364
Acrylamid	GHS06, GHS08	H350, H340, H361f, H301f, 372, H332, H312, H319, H315, H317	P201, P280, P301+P310, P305+P351+P338, P308+P313
APS	GHS03, GHS07, GHS08	H272, H302, H315, H319, H334, H335, H317	P280, P305+P351+P338, P302+P352, P304+P341, P342+P311
Barium chloride dihydrate	GHS06	H301, H332	P308+P310
DTT	GHS07	H302, H315, H319	P302+P352, P305+P351+P338
Acetic acid	GHS02, GHS05	H226, H314	P280, P301+P330+P331, P307+P310, P305+P351+P338
Ethanol	GHS02	H225	P210
Ethidium bromide	GHS06, GHS08	H330, H341, H302, H315, H319, H335	P281, P302+P352, P305+P351+P338, P304+P340, P309, P310
Isopropanol	GHS02, GHS07	H225, H319 H336	P210, P233, P305+P351+P338
Methanol	GHS02, GHS06, GHS08	H225 H331, H311, H301, H370	P210 P233, P280, P302+P352, P309+P310
Sodium acetate	Not hazardous according to GHS		
Natriumhydroxid	GHS05	H314, H290	P280, P301+P330+P331, P309+P310, P305+P351+P338
Hydrochloric acid, conc.	GHS05, GHS07	H314, H335	P260, P301+P330+P331, P303+P361+P353, P305+P351+P338, P405, P501
Propidium iodide	GHS06, GHS07, GHS08	H301, H315, H319, H332, H335, H340, H341	P201, P281, P301+P310 P305+P351+P338 P330
Sodium-dodecyl-sulfate	GHS02, GHS06	H228, H311, H302, H335, H315, H319	P210, P280, P304+P340, P305+P351+P338, P309+P310
Tetramethylethylendiamin	GHS02, GHS05, GHS07	H225, H332, H302, H314	P210, P233, P280, P301+P330+P331, P305+P351+P338, P309+P310
Tris	GHS07	H315, H319, H335	P261, P305+P351+P338
Trypan blue	GHS08	H350	P280, P201, P202, P308+313 P405, P501

10.4. CMR substances

CMR substances used in course of this work are given in Table 30.

Table 30: CMR substances used in this work.

CAS number	compound	Application and amounts used	Category I or II
79-06-1	Acrylamide	30-40% aqueous solutions for polymerization. Total amount: 500 mL	K: 1B M: 1B R _f : 2
56-65-5	γ ³² P-ATP	radio labeling of nucleic acids Total amount: 300 μ L	
1239-45-8	Ethidium bromide	10 mg/mL aqueous solutions for staining of polyacrylamide gels (0.5 mg/mL final concentrations). Total amount: 30 mL	M: 2
25535-16-4	Propidium iodide	aqueous solutions for staining of cellular DNA (10 μ g/mL). Total amount: 30 mL	M: 1B

10.5. List of proteins identified by LC-MS analysis (5.3.2)

Table 31: Proteins (murine) from BaF3_hIL-6R lysate identified by LC-MS.

Protein	UniProt Accession code	MW [kDa]	Band	Unique peptides
ATP synthase subunit alpha, mitochondrial	Q03265	56,27	②	11
ATP synthase subunit beta, mitochondrial	P56480	50,10	①, ②	6
Tubulin alpha-1A chain	P68369	50,12	①, ②	6
Tubulin alpha-1B chain	P05213	49,88	①, ②	6
Tubulin alpha-1C chain	P68373	41,71	①, ②	4
Actin, cytoplasmic 1	P60710	41,77	①, ②	4
Actin, cytoplasmic 2	P63260	49,93	①, ②	4
Tubulin alpha-3 chain	P05214	53,66	①, ②	5
Vimentin	P20152	49,64	①, ②	5
Tubulin beta-5 chain	P99024	49,88	①, ②	4
Tubulin beta-2A chain	Q7TMM9	49,92	①, ②	4
Tubulin beta-2B chain	Q9CWF2	49,55	①, ②	4
Tubulin beta-4A chain	Q9D6F9	49,80	①, ②	4
Tubulin beta-4B chain	P68372	59,72	①, ②	5

Table 32: Proteins (human) from BaF3_hIL-6R lysate identified by LC-MS.

Protein	UniProt Accession code	MW [kDa]	Band	Unique peptides
Keratin, type I cuticular Ha3-I	O76009	45,911	②	1
Keratin, type I cuticular Ha3-II	Q14525	46,185	②	1
ATP synthase subunit alpha, mitochondrial	P25705	59,714	②	7
Keratin, type II cytoskeletal 1b	Q7Z794	61,864	②	0
Keratin, type I cuticular Ha4	O76011	49,392	②	1
Keratin, type II cuticular Hb3	P78385	54,161	②	3
Keratin, type II cuticular Hb1	Q14533	54,893	②	3
Keratin, type II cuticular Hb6	O43790	53,466	②	3
Putative keratin-87 protein	A6NCN2	29,099	②	2
Keratin, type II cytoskeletal 75	O95678	59,524	②	1
Keratin, type II cytoskeletal 79	Q5XKE5	57,8	②	0
Tubulin beta-8 chain	Q3ZCM7	49,744	②	2
Keratin, type I cuticular Ha2	Q14532	50,31	②	0
Tubulin beta-8 chain-like protein LOC260334	A6NNZ2	49,541	②	2
Keratin, type I cuticular Ha5	Q92764	50,329	②	0
Tubulin beta-6 chain	Q9BUF5	49,825	②	2
Antithrombin-III	P01008	52,569	②	1
Eukaryotic initiation factor 4A-I	P60842	46,125	②	1
14-3-3 protein gamma	P61981	28,285	②	1
14-3-3 protein theta	P27348	27,747	②	1
Canalicular multispecific organic anion transporter	O15438	169,234	②	1
14-3-3 protein epsilon	P62258	29,155	②	1
Elongation factor 1-gamma	P26641	50,087	②	1
14-3-3 protein zeta/delta	P63104	27,728	②	1
Keratin, type I cuticular Ha6	O76013	52,214	②	1
Pyruvate kinase PKM	P14618	57,9	②	1

APPENDICES

Protein	UniProt Accession code	MW [kDa]	Band	Unique peptides
14-3-3 protein eta	Q04917	28,201	②	1
Rho guanine nucleotide exchange factor 12	Q9NZN5	173,125	②	1
Tubulin beta-1 chain	Q9H4B7	50,295	②	1
14-3-3 protein beta/alpha	P31946	28,065	②	1
Eukaryotic initiation factor 4A-II	Q14240	46,373	②	1
14-3-3 protein sigma	P31947	27,757	②	1
Serum albumin	P02768	69,32	①, ②	19
Keratin, type II cytoskeletal	P04264	66,00	①, ②	14
Keratin, type I cytoskeletal 10	P13645	58,79	①, ②	12
Keratin, type II cytoskeletal 2 epidermal	P35908	65,39	①, ②	8
ATP synthase subunit beta, mitochondrial	P06576	56,53	①, ②	10
Keratin, type I cytoskeletal 9	P35527	62,03	①, ②	11
Vimentin	P08670	53,62	①, ②	7
Tubulin alpha-1B chain	P68363	50,12	①, ②	6
Tubulin alpha-1A chain	Q71U36	50,10	①, ②	6
Tubulin alpha-1C chain	Q9BQE3	49,86	①, ②	6
Keratin, type I cuticular Ha1	Q15323	47,21	①, ②	2
Ig gamma-1 chain C region	P01857	36,08	①, ②	4
Actin, cytoplasmic 2	P63261	41,77	①, ②	4
Actin, cytoplasmic 1	P60709	41,71	①, ②	4
Elongation factor 1-alpha 1	P68104	50,11	①, ②	5
Putative elongation factor 1-alpha-like 3	Q5VTE0	50,15	①, ②	5
Glyceraldehyde-3-phosphate dehydrogenase	P04406	36,03	①, ②	4
Ig gamma-2 chain C region	P01859	35,88	①, ②	3
Ig kappa chain C region	P01834	11,60	①, ②	4
Tubulin beta chain	P07437	49,64	①, ②	5
Histone H4	P62805	11,36	①, ②	3
Tubulin alpha-3E chain	Q6PEY2	49,83	①, ②	4

APPENDICES

Protein	UniProt Accession code	MW [kDa]	Band	Unique peptides
Tubulin beta-4A chain	P04350	49,55	①, ②	4
Alpha-enolase	P06733	47,14	①, ②	3
Tubulin alpha-3C/D chain	Q13748	49,93	①, ②	4
Tubulin beta-4B chain	P68371	49,80	①, ②	4
Ig gamma-4 chain C region	P01861	35,92	①, ②	2
Tubulin beta-2A chain	Q13885	49,88	①, ②	4
Elongation factor 1-alpha 2	Q05639	50,44	①, ②	3
Tubulin beta-2B chain	Q9BVA1	49,92	①, ②	4
Keratin, type II cuticular Hb5	P78386	55,77	①, ②	4
Histone H2B type F-S	P57053	13,94	①, ②	3
Actin, alpha skeletal muscle	P68133	42,02	①, ②	2
Histone H2B type 1-N	Q99877	13,91	①, ②	3
Actin, aortic smooth muscle	P62736	41,98	①, ②	2
Tubulin alpha-4A chain	P68366	49,89	①, ②	3
Histone H2B type 1-H	Q93079	13,88	①, ②	3
Histone H2B type 1-C/E/F/G/I	P62807	13,90	①, ②	3
60 kDa heat shock protein, mitochondrial	P10809	61,02	①, ②	1
Actin, alpha cardiac muscle 1	P68032	41,99	①, ②	2
Histone H2B type 1-D	P58876	13,93	①, ②	3
Histone H2B type 1-M	Q99879	13,98	①, ②	3
Histone H2B type 2-F	Q5QNW6	13,91	①, ②	3
Tubulin beta-3 chain	Q13509	50,40	①, ②	3
Actin, gamma-enteric smooth muscle	P63267	41,85	①, ②	2
Lysozyme C	P61626	16,53	①, ②	2
Histone H2B type 1-K	O60814	13,88	①, ②	3
Histone H2B type 1-L	Q99880	13,94	①, ②	3
Tubulin alpha-8 chain	Q9NY65	50,06	①, ②	2
Histone H2B type 3-B	Q8N257	13,90	①, ②	2
Histone H2B type 1-J	P06899	13,90	①, ②	2

APPENDICES

Protein	UniProt Accession code	MW [kDa]	Band	Unique peptides
Galectin-1	P09382	14,71	①, ②	2
Histone H2B type 2-E	Q16778	13,91	①, ②	2
Histone H2B type 1-O	P23527	13,90	①, ②	2
Histone H2B type 1-B	P33778	13,94	①, ②	2
78 kDa glucose-regulated protein	P11021	72,29	①, ②	1
Beta-actin-like protein 2	Q562R1	41,98	①, ②	1
Histone H2A,J	Q9BTM1	14,01	①, ②	1
POTE ankyrin domain family member E	Q6S8J3	121,29	①, ②	1
Keratin, type I cytoskeletal 25	Q7Z3Z0	49,29	①, ②	1
Polyubiquitin-C	P0CG48	76,99	①, ②	1
Histone H2AX	P16104	15,14	①, ②	1
Histone H2A type 1-D	P20671	14,10	①, ②	1
Probable G-protein coupled receptor 115	Q8IZF3	77,67	①, ②	1
Keratin, type I cytoskeletal 27	Q7Z3Y8	49,79	①, ②	1
Histone H2A type 1 SV=2	P0C0S8	14,08	①, ②	1
Keratin, type II cuticular Hb2	Q9NSB4	56,62	①, ②	1
E3 ubiquitin-protein ligase makorin-1	Q9UHC7	53,32	①, ②	1
Hemoglobin subunit gamma-2	P69892	16,12	①, ②	1
Heat shock protein 75 kDa, mitochondrial	Q12931	80,06	①, ②	1
Polyubiquitin-B	P0CG47	25,75	①, ②	1
Ubiquitin-40S ribosomal protein S27a	P62979	17,95	①, ②	1
Hemoglobin subunit gamma-1	P69891	16,13	①, ②	1
Ubiquitin-60S ribosomal protein L40	P62987	14,72	①, ②	1
Histone H2A type 1-C	Q93077	14,10	①, ②	1
Histone H2A,Z	P0C0S5	13,55	①, ②	1
Heat shock protein HSP 90-alpha	P07900	84,61	①, ②	1
60S ribosomal protein L14	P50914	23,42	①, ②	1
Histone H2A type 1-J	Q99878	13,93	①, ②	1
Histone H2A type 1-B/E	P04908	14,13	①, ②	1

Protein	UniProt Accession code	MW [kDa]	Band	Unique peptides
POTE ankyrin domain family member F	A5A3E0	121,37	①, ②	1
Hemoglobin subunit delta	P02042	16,05	①, ②	1
Histone H2A type 1-A	Q96QV6	14,23	①, ②	1
Probable E3 ubiquitin-protein ligase makorin-3	Q13064	55,61	①, ②	1
Hemoglobin subunit epsilon	P02100	16,19	①, ②	1
Histone H2A,V OS	Q71UI9	13,50	①, ②	1
Histone H2A type 3	Q7L7L0	14,11	①, ②	1
Histone H2A type 2-C	Q16777	13,98	①, ②	1
Histone H2A type 2-B	Q8IUE6	13,99	①, ②	1
Keratin, type I cytoskeletal 28	Q7Z3Y7	50,54	①, ②	1
Histone H2A type 2-A	Q6FI13	14,09	①, ②	1
Heat shock protein HSP 90-beta	P08238	83,21	①, ②	1
Putative beta-actin-like protein 3 OS	Q9BYX7	41,99	①, ②	1
Hemoglobin subunit beta	P68871	15,99	①, ②	1
Histo-blood group ABO system transferase	P16442	40,91	①, ②	1
Histone H2A type 1-H	Q96KK5	13,90	①, ②	1

Table 33: Proteins (human) from HeLa lysate identified by LC-MS.

Protein	UniProt Accession code	MW [kDa]	Band	Unique peptides
60 kDa heat shock protein, mitochondrial	P10809	61,02	③, ④	19
Actin, cytoplasmic 1	P60709	41,71	③, ④	5
Actin, cytoplasmic 2	P63261	41,77	③, ④	5
Alpha-enolase	P06733	47,14	③, ④	7
			⑤, ⑥	16
ATP-dependent RNA helicase DDX3X	O00571	73,20	③, ④	8
ATP-dependent RNA helicase DDX3Y	O15523	73,11	③, ④	5
Cleavage and polyadenylation specificity factor subunit 6	Q16630	59,17	④	5
Desmoplakin	P15924	331,57	④	9

APPENDICES

Protein	UniProt Accession code	MW [kDa]	Band	Unique peptides
DnaJ homolog subfamily A member 1	P31689	44,84	⑤, ⑥	4
Elongation factor 1-alpha 1	P68104	50,11	③, ④	6
			⑤, ⑥	12
Elongation factor 1-alpha 2	Q05639	50,44	③, ④	4
			⑤, ⑥	7
Far upstream element-binding protein 1	Q96AE4	67,52	③, ④	4
G patch domain and KOW motifs-containing protein	Q92917	52,20	③, ④	4
Glyceraldehyde-3-phosphate dehydrogenase	P04406	36,03	③, ④	5
Glyceraldehyde-3-phosphate dehydrogenase	P04406	36,03	⑤, ⑥	4
Heat shock 70 kDa protein 1A/1B	P08107	70,01	③, ④	19
Heat shock 70 kDa protein 1-like	P34931	70,33	③, ④	5
Heat shock 70 kDa protein 6	P17066	70,98	③, ④	6
Heat shock cognate 71 kDa protein	P11142	70,85	③, ④	20
Heat shock protein beta-1	P04792	22,77	③, ④	4
Heat shock-related 70 kDa protein 2	P54652	69,98	③, ④	6
Heterogeneous nuclear ribonucleoprotein F	P52597	45,64	⑤, ⑥	6
Heterogeneous nuclear ribonucleoprotein K	P61978	50,94	③, ④	17
Heterogeneous nuclear ribonucleoprotein L	P14866	64,09	③, ④	5
Heterogeneous nuclear ribonucleoprotein M	P52272	77,46	③, ④	4
Heterogeneous nuclear ribonucleoprotein Q	O60506	69,56	③, ④	5
Heterogeneous nuclear ribonucleoprotein R	O43390	70,90	④	4
Ig gamma-1 chain C region	P01857	36,08	③, ④	4
			⑤, ⑥	5
Ig kappa chain C region	P01834	11,60	③, ④	4
Junction plakoglobin	P14923	81,69	④	6
Keratin, type I cytoskeletal 10	P13645	58,79	③, ④	21
			⑤, ⑥	16
Keratin, type I cytoskeletal 14	P02533	51,53	④	5
Keratin, type I cytoskeletal 16	P08779	51,24	④	14

APPENDICES

Protein	UniProt Accession code	MW [kDa]	Band	Unique peptides
Keratin, type I cytoskeletal 18	P05783	48,03	⑤, ⑥	12
Keratin, type I cytoskeletal 9	P35527	62,03	③, ④	25
			⑤, ⑥	11
Keratin, type II cytoskeletal 1	P04264	66,00	③, ④	27
			⑤, ⑥	19
Keratin, type II cytoskeletal 2 epidermal	P35908	65,39	③, ④	16
			⑤, ⑥	8
Keratin, type II cytoskeletal 5	P13647	62,34	③, ④	9
Keratin, type II cytoskeletal 6A	P02538	60,01	④	4
Keratin, type II cytoskeletal 6C	P48668	59,99	④	4
Keratin, type II cytoskeletal 8	P05787	53,67	⑤, ⑥	8
Non-POU domain-containing octamer-binding protein	Q15233	54,20	③, ④	7
Nuclease-sensitive element-binding protein 1	P67809	35,90	③, ④	6
			⑤, ⑥	4
Nucleolin	P19338	76,57	③, ④	15
			⑤, ⑥	6
Nucleophosmin	P06748	32,56	③, ④	7
Perilipin-3	O60664	47,05	⑤, ⑥	10
Poly(U)-binding-splicing factor PUF60	Q9UHX1	59,84	③, ④	9
Prelamin-A/C	P02545	74,10	③, ④	20
Probable ATP-dependent RNA helicase DDX17	Q92841	80,22	③, ④	4
Probable ATP-dependent RNA helicase DDX5	P17844	69,11	③, ④	15
Putative elongation factor 1-alpha-like 3	Q5VTE0	50,15	③, ④	6
			⑤, ⑥	12
Ras GTPase-activating protein-binding protein 1	Q13283	52,13	③, ④	9
RNA-binding motif protein, X chromosome	P38159	42,31	⑤, ⑥	6
RNA-binding protein FUS	P35637	53,39	③, ④	11
RuvB-like 1	Q9Y265	50,20	⑤, ⑥	10

APPENDICES

Protein	UniProt Accession code	MW [kDa]	Band	Unique peptides
Serum albumin	P02768	69,32	③, ④	21
			⑤, ⑥	18
Splicing factor 3A subunit 3	Q12874	58,81	③, ④	4
Stress-70 protein, mitochondrial	P38646	73,64	③, ④	14
Trifunctional enzyme subunit beta	P55084	51,262	⑥	4
Tubulin alpha-1A chain	Q71U36	50,10	③, ④	8
Tubulin alpha-1B chain	P68363	50,12	③, ④	10
Tubulin alpha-1C chain	Q9BQE3	49,86	③, ④	9
Tubulin alpha-3C/D chain	Q13748	49,93	③, ④	6
Tubulin alpha-3E chain	Q6PEY2	49,83	③, ④	6
Tubulin alpha-4A chain	P68366	49,89	③, ④	6
			⑤, ⑥	4
Tubulin alpha-8 chain	Q9NY65	50,06	③, ④	4
Tubulin beta chain	P07437	49,64	⑤, ⑥	4
Vimentin	P08670	53,62	③, ④	14
			⑤, ⑥	14

10.6. Eidesstattliche Versicherung

Hiermit erkläre ich an Eides statt, die vorliegende Dissertation selbst verfasst und keine anderen als die angegebenen Hilfsmittel benutzt zu haben. Ich versichere, dass diese Dissertation nicht in einem früheren Promotionsverfahren eingereicht wurde.

Declaration on Oath

I hereby confirm that I wrote this dissertation on my own, without using any other than the acknowledged resources and aids.

The content of this dissertation has neither been submitted, nor accepted nor graded 'failed' in a previous doctoral procedure.

Hamburg, 07.03.2016

Kristina Dorothee Gorkotte-Szameit

